INTEGRATED OPTICAL COMPONENTS PRODUCED IN GaAs AND InP EPITAXIAL LAYERS USING THE PHOTO-ELASTIC EFFECT

By

Trevor Mark Benson

A thesis presented for the Degree of Doctor of Philosophy, University of Sheffield, Department of Electronic and Electrical Engineering, September 1982.

TEXT
CUT OFF IN THE
ORIGINAL

SUMMARY

Studies have been made of optical waveguides produced in GaAs and InP epitaxial layers. Of the possible waveguiding mechanisms present in these devices the contribution from the photo-elastic effect (strain-induced refractive index changes) dominates. Stresses in evaporated metal films and their control have been investigated.

Strain-induced waveguides have been used to produce a novel directional-coupler structure with a short coupling length ($\sim$2mm). In GaAs bias has been applied to control the amount of light at the output of each of the two waveguides forming these couplers and it has been possible to isolate the light in either the excited or the coupled waveguide.

A new theoretical model, based on finite difference techniques, has been developed and used to analyse strain-induced, slab and rib waveguide structures. Results obtained have been compared with those from other methods. Theoretical predictions of guiding properties in GaAs strain-induced waveguides give good agreement with experimental results in all cases. Optical waveguiding in InP layers using the same photo-elastic mechanisms, assessed experimentally, indicates that the refractive index changes are similar to those in GaAs but slightly larger. One of the first measurements of the non-zero electro-optic coefficient, r_{41}, of InP is described. Guiding properties vary little with time in both InP and GaAs.

The reflection of light guided in a single-mode photo-elastic waveguide into a second perpendicular guide using a

vertical etched facet running at 45° to the direction of propagation is proposed for providing bending with negligible loss and some experimental results are reported.

ACKNOWLEDGEMENTS

The author is indebted to Professor P.N. Robson and Dr. P.A. Houston for their invaluable help and enthusiastic supervision of this project.

It is a pleasure to thank Drs. D.H. Newman, S. Ritchie, M.W. Austin, L.D. Westbrook and A.J. Houghton at British Telecom Research Laboratories, Martlesham Heath for many stimulating discussions and helpful suggestions and for the provision of InP and GaAs epitaxial material. The kindness of Dr. D. Ashen of R.S.R.E., Dr. J. Roberts and Mr. J.H. Marsh in growing material is gratefully acknowledged.

Special thanks are due to Dr. T. Murotani of the Mitsubishi Electrical Corporation for advice and assistance with InP device fabrication and to Dr. J. Buus of the Technical University of Denmark for enlightening conversations on the effective refractive index method. Dr. T. Searle of the Department of Physics is also thanked for the loan of equipment.

Expert technical assistance received under the leadership of Mr. P.G. Ridsdale, Mr. R. Cousin, Mr. I. Moulson and Mr. H. Flower is very much appreciated. In addition the author thanks many members of the academic staff and fellow research students for help and advice.

The author's gratitude is extended to Mrs. B. Cowell for her patience and diligence in typing this thesis swiftly and accurately.

The work reported here was carried out under an SERC

CASE studentship in collaboration with British Telecom and the author extends his thanks for this financial support.

PUBLISHED WORK

The following papers have been published on the results of some of the work described in this thesis.

1. "Photoelastic Optical Directional Couplers in Epitaxial GaAs Layers".
   T.M. Benson, T. Murotani, P.A. Houston, P.N. Robson.
   Electronics Letters, 17, 237, 1981.

2. "Photoelestic Optical Waveguiding in InP Epitaxial Layers".
   T.M. Benson, T. Murotani, P.N. Robson, P.A. Houston,
   Presented at the 7th European Conference on Optical Communication, Copenhagen, Sept. 1981.
   Published in Conference Proceedings as Paper 9.4.

3. "Photoelastic Optical Directional Couplers in Epitaxial GaAs Layers at 1.15μm".
   T.M. Benson, T. Murotani, P.N. Robson, P.A. Houston.
   Presented at the 1st European Conference on Integrated Optics, London, Sept. 1981.

4. "A Novel Electro-optically Controlled Directional Coupler Switch in GaAs Epitaxial Layers at 1.15μm".
   T.M. Benson, T. Murotani, P.N. Robson, P.A. Houston.
   Accepted for publication in IEEE Transactions on Electron Devices for the Special Issue on Optoelectronic Devices, Sept. 1982.

CONTENTS Page No.

Page No.

CHAPTER 1

INTRODUCTION

Optical-fibre transmission has established itself as a reliable and cost-effective technology capable of meeting the rapidly increasing demand for high bit-rate communications. Light as a carrier wave, modulated to carry data, offers an enormous potential bandwidth for communications because of its high frequency although practical bandwidth is limited by the components of the fibre system.

The aim of integrated optics is to provide system components such as switches, mixers and modulators using light confined in thin dielectric films. The ultimate goal is 'monolithic' integrated optics where light sources [1] and detectors [2] are fabricated on the same substrate as the other circuit components.

The simplest integrated optical components are passive waveguides. These require the creation of a region with a higher refractive index that its surroundings and can be manufactured, for example, from glasses of different composition[3]. To provide external control of the light in the waveguide it is required to use materials in which local refractive index changes can be induced via the electro-optic, the acousto-optic or the magneto-optic effects. Of a host of materials used to make individual devices [4] lithium niobate ($LiNbO_3$) has the merits of a high electro-optic coefficient, good acousto-optic properties and a well-developed technology for waveguide formation based on titanium in-diffusion. It is unsuitable for monolithic integration, however, as no $LiNbO_3$ source is available.

Gallium arsenide (GaAs) and related compounds therefore hold a major advantage as sources in the right part of the infra-red spectrum can be fabricated. GaAs based lasers or light-emitting diodes (L.E.D's) are used as light sources for multimode fibre systems installed world-wide [5],[6],[7]. The emitted wavelengths of 0.8-0.9μm enable silicon avalanche photodiodes (A.P.D's) to be used as detectors.

By operating in a longer wavelength region (1.25-1.6μm) fibre attenuation and material dispersion can be minimised [8]. The InGaAsP/InP materials system has been exploited to produce highly efficient light sources in this wavelength range. Changing the composition alters the bandgap and hence the emitting wavelength. More recent attention has been focussed onto monomode fibre, where bandwidth is limited solely by material chromatic dispersion, for higher transmission speeds and longer distances [9],[10]. The chromatic dispersion of silica fibre goes through a zero near 1.3μm and at this wavelength there is no first-order limitation on bandwidth. The continued improvement and acceptance of single-mode fibres enhances the prospects for high data-rate systems employing integrated optical terminal devices since the great majority of integrated optical circuits and devices are single-mode structures.

Direct modulation of semiconductor laser drive current is the most convenient way of digital encoding. However, under rapid modulation wavelength instability is encountered [11]. Fast encoding by external guided-wave modulators could overcome this limitation, allowing stable continuous operation of the laser.

The electro-optic effect in GaAs allows for phase modulation of TE propagating modes whereas TM modes are unaffected. By exciting both TE and TM modes an external analyser can be employed to convert the phase shift to intensity modulation [12].

The directional-coupler switch provides for the modulation of light in a waveguide by the transfer of the guided light to a similar adjacent waveguide. The device length may be chosen to give complete power transfer between the two phase-synchronous guides. Field-induced refractive index changes may then be used to destroy the phase synchronism and thereby switch the light back to the initially excited guide. The switching performance depends critically on the phase matching between the waveguides and on device length.

Electro-optically controlled directional-coupler (E.C.D.) switches have been fabricated in $LiNbO_3$ using in-diffused waveguides [13] and in GaAs and GaAlAs using 'metal-gap' guides [14], rib waveguides of the Schottky Barrier [15] or M.O.S. [16] type and $p^+n^-n^+$ channel-stop strip guides [17].

In the stepped $\Delta\beta$ reversal directional-coupler switch [18] the sign of the refractive index step induced between the two guides forming the directional coupler is reversed halfway along the device. The advantage of multi-electrode pairs for a large-extinction ratio switch was first demonstrated in $LiNbO_3$ [19]. In GaAs Leonberger and Bozler [20] reported up to 99.7% cross-over (25dB) using a metal-gap structure with two electrode pairs.

Modulator structures based on band-to-band absorption effects at wavelengths near the bandgap [21] have also been fabricated in GaAs but active Y-junction switches [22] and the Mach-Zehnder interference modulator structure [23] have still to be demonstrated in this material. Westbrook showed clearly that passive single-mode optical waveguides can conveniently be produced in GaAs epitaxial layers by strain-induced refractive index changes [24]. In this thesis the nature of the stress in evaporated metal films has been studied and the findings of Westbrook confirmed. Ways in which the amount of stress introduced may be controlled and time-dependent annealing effects have been examined. Strain-induced wave-guides have been used to produce a novel directional coupler structure with a short coupling length ($\sim$2mm) and high synchronism without rigid fabrication tolerances. It is also shown that in GaAs waveguides formed by the epitaxy of low-doped GaAs on a heavily-doped GaAs substrate strain-induced refractive index changes must also be included to explain the behaviour of 'metal-gap' E.D.C. devices.

A new theoretical model based on finite difference techniques has been developed to analyse electromagnetic wave propagation in waveguide structures in general but in the inhomogeneous strain structures in particular. In addition to using the technique to study strain waveguides a theoretical analysis of some rib-waveguide structures has been made to allow comparison with other methods.

Optical waveguiding in InP layers using the same photo-elastic mechanisms has been examined to assess possible application to integrated optics in the long wavelength systems.

In GaAs guiding around bends has also been evaluated as these will be essential for increasing device packing density in envisaged integrated optical circuits. It is shown that the refractive index changes forming the observed waveguides are not large enough for fabricating curved waveguide sections with radii of curvature comparable with integrated optics and exhibiting tolerable loss. A method for forming bends in waveguides by reflection off an etched vertical wall is proposed therefore for providing waveguiding through a right angle with negligible loss. Experimental results for this structure are presented.

CHAPTER 2

GUIDED-WAVE OPTICS

2.1 Dielectric Slab Waveguide

The dielectric slab form of optical waveguide, illustrated in Fig.2.1, consists of a planar film of refractive index n_2 sandwiched between two regions with lower refractive indices n_1 and n_3 respectively. Light is confined by total internal reflection at each of the material interfaces.

A study of the slab waveguide is useful in gaining an understanding of the waveguiding properties of more complicated dielectric waveguides. Its simple geometry enables the finite number of guided modes and the infinite number of radiation modes to be described mathematically without difficulty and obtained as solutions of boundary-value problems.

A ray-optical picture of light propagation in slab waveguides is first outlined to gain a physical understanding. Although this approach can provide a number of useful results such as propagation constants and cut-off widths it is then shown that a much more complete description is provided by electromagnetic theory. The results obtained from the two treatments are in complete agreement.

In the devices described in this thesis GaAs optical slab waveguides are produced by growing epitaxial layers of n^- GaAs on an n^+ GaAs substrate as in Fig. 2.2. The depression of the refractive index Δn due to free carriers is given by [25]:

$$\Delta n = \frac{Ne^2 \lambda_0^2}{8\pi^2 \varepsilon_0 n_0 m^* c^2} \qquad (2.1)$$

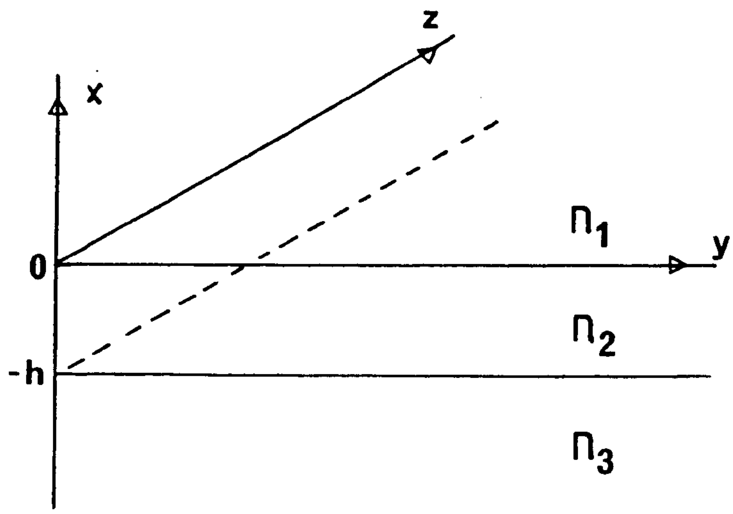

Fig.2.1 Generalised dielectric slab waveguide showing notation for axes and refractive indices.

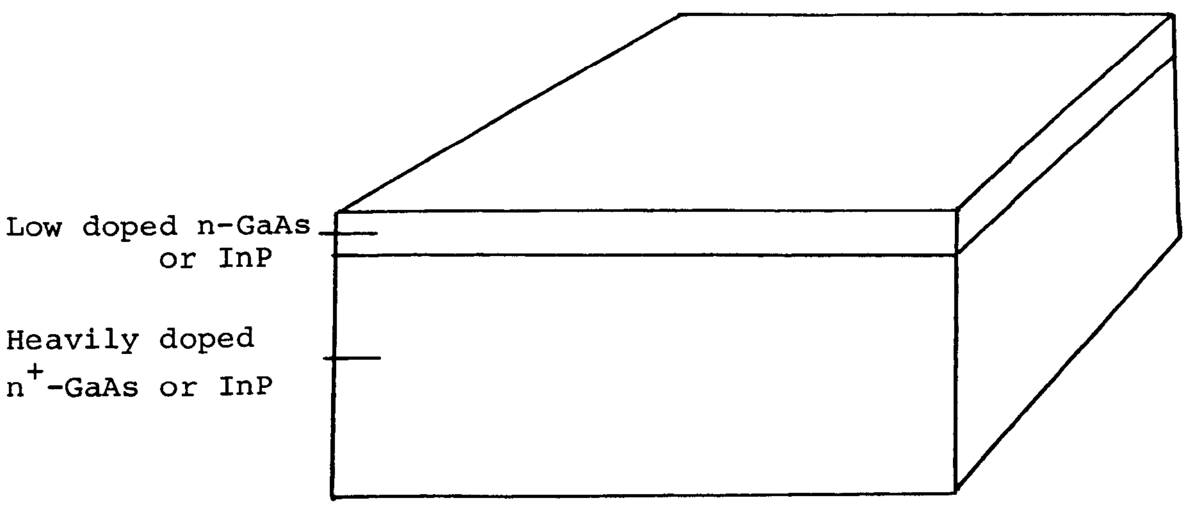

Fig.2.2 Slab waveguide due to free carriers as used in this work.

where N is the number of free carriers per cubic metre, m^* the carrier effective mass, e the electronic charge, ε_0 the permittivity of free space, c the velocity of light in free space, n_o the refractive index in the absence of free carriers and λ_0 the free-space wavelength. Because of the large difference between the doping levels the value of (n_2-n_3) is taken as Δn for the substrate, calculated using (2.1). Quality is good enough for material and interface perturbation losses to be neglected.

2.1.1 Ray-optical treatment of slab waveguides

Consider the ray picture of Fig.2.3. For the guided mode illustrated θ must exceed the critical angles at both interfaces to get total internal reflection. In the present case therefore θ must be greater than $\sin^{-1}(n_3/n_2)$, the critical angle at P, since the critical angle at the substrate interface is larger than the one at the air interface because of the smaller refractive index difference.

The light trapped in the region of refractive index n_2 may be considered to travel in a zig-zag path and, by satisfying the requirement that the total phase shift sums to $2q\pi$ where q is an integer, the propagation constant β of a guided mode may be found. β is related to the zig-zag angle θ by :-

$$\beta = k_o n_2 \sin\theta \qquad (2.2)$$

where $k_o = 2\pi/\lambda_0$.

The critical angle and equation (2.2) produce bounds for β such that :

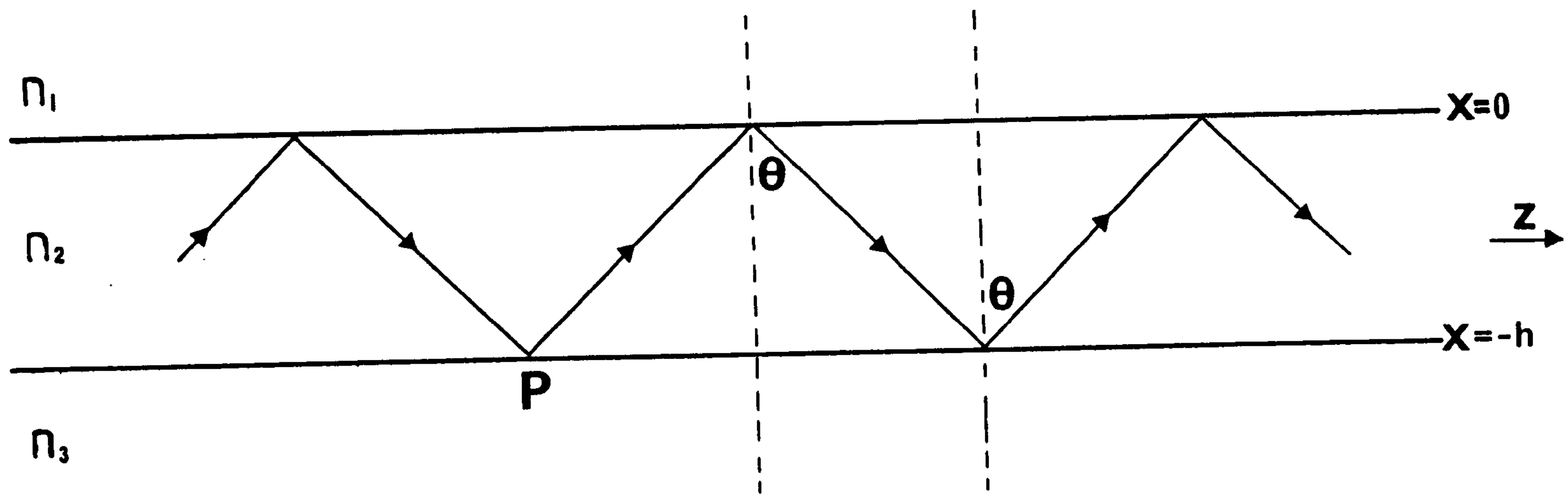

Fig.2.3 Side view of a slab waveguide showing wave normals of the zig-zag waves corresponding to a guided mode.

$$k_o n_3 < \beta < k_o n_2$$

The determination of β requires knowledge of the phase shifts $2\phi_s$ and $2\phi_c$ at the n_2-n_3 and n_2-n_1 interfaces respectively. In Appendix 9.1 expressions for the phase shifts on reflection of a plane wave at plane interfaces are derived for both TE and TM polarisations. It follows that in all cases the angle ϕ_s is given by :-

$$\tan\phi_s = \sqrt{n_2^2 \sin^2\theta - n_3^2}/n_2\cos\theta \tag{2.3}$$

for TE modes, and

$$\tan\phi_s = \frac{n_2^2}{n_3^3} \frac{\sqrt{n_2^2 \sin^2\theta - n_3^2}}{n_2\cos\theta} \tag{2.4}$$

for TM modes. With n_1 replacing n_3 the same relationships hold for tan ϕ_c for a dielectric/dielectric interface between n_2 and the cover n_1.

Only a discrete set of angles θ leads to a self-consistent picture and "guided modes". Consider a guide cross-section Z = constant and the phase shifts on moving from the x = -h boundary to the one at x = 0 and then back with the reflected wave. The total phase shift must equal a multiple of 2π for self-consistency. Thus

$$2k_o n_2 h\cos\theta - 2\phi_s - 2\phi_c = 2q\pi \tag{2.5}$$

where ϕ_s and ϕ_c are functions of θ as mentioned.

From equations (2.2), (2.3) and (2.4) :

$$2\phi_s = 2\tan^{-1}\{ \, Y_1 \left(\frac{\beta^2 - n_3^2 k_0^2}{n_2^2 k_0^2 - \beta^2}\right)^{\frac{1}{2}} \} \tag{2.6}$$

and

$$2\phi_c = 2\tan^{-1}\{ \, Y_3 \left(\frac{\beta^2 - n_1^2 k_0^2}{n_2^2 k_0^2 - \beta^2}\right)^{\frac{1}{2}} \} \tag{2.7}$$

where $$Y_i = \left(\frac{n_2}{n_i}\right)^2 \text{ for TM modes}$$
$$= 1 \text{ for TE modes}$$

Defining

$$\begin{aligned} p_1^2 &= \beta^2 - n_1^2 k_0^2 \\ q_2^2 &= n_2^2 k_0^2 - \beta^2 \\ p_3^2 &= \beta^2 - n_3^2 k_0^2 \end{aligned} \qquad (2.8)$$

(2.5) becomes

$$k_0 n_2 h\cos\theta - \tan^{-1}\left(\frac{Y_3 p_3}{q_2}\right) - \tan^{-1}\left(\frac{Y_1 p_1}{q_2}\right) = q\pi \qquad (2.9)$$

Now $k_0 n_2 h\cos\theta = hq_2$ so,

$$(hq_2 - q\pi) = \tan^{-1}\left(\frac{Y_3 p_3}{q_2}\right) + \tan^{-1}\left(\frac{Y_1 p_1}{q_2}\right),$$

i.e.

$$\tan(hq_2 - q\pi) = \frac{\left(\frac{Y_3 p_3}{q_2} + \frac{Y_1 p_1}{q_2}\right)}{\left(1 - \frac{p_1 p_3 Y_1 Y_3}{q_2^2}\right)}$$

$$= \frac{q_2(Y_1 p_1 + Y_3 p_3)}{(q_2^2 - Y_1 Y_3 p_1 p_3)} \qquad (2.10)$$

(2.10) is an eigenvalue equation for the transverse propagation constant q_2.

For the case of a metal cover equations (2.3) and (2.4) become (see Appendix 9.1) :

$$\tan\phi_c \sim \frac{(n_c'')}{n_2\cos\theta}\left(1 + \frac{n_2^2\sin^2\theta}{(n_c'')^2}\right)^{\frac{1}{2}} \qquad (2.11)$$

for TE modes, and

$$\tan\phi_c \sim \frac{n_2(n_c'')^2\cos\theta}{n_2^2\{(n_c'')^2 + n_2^2\sin^2\theta)\}^{\frac{1}{2}}} \qquad (2.12)$$

for TM modes where $n_1 = n_c^{1} - jn_c'' \sim -jn_c''$.

2.1.2 Fundamentals of the electromagnetic theory of dielectric waveguides

Maxwell's equations for time dependent fields in a source-free region are :-

$$\nabla x \underset{\sim}{H} = \frac{\partial \underset{\sim}{D}}{\partial t} \tag{2.13}$$

$$\nabla x \underset{\sim}{E} = -\frac{\partial \underset{\sim}{B}}{\partial t} \tag{2.14}$$

$$\nabla . \underset{\sim}{H} = 0 \tag{2.15}$$

$$\nabla . \underset{\sim}{E} = 0 \tag{2.16}$$

where $\underset{\sim}{E}$, $\underset{\sim}{H}$, $\underset{\sim}{D}$ and $\underset{\sim}{B}$ are time dependent vectors of electric and magnetic field, electric displacement and magnetic induction respectively.

Assume fields with a periodic time dependence of angular frequency ω and a lossless medium of dielectric constant ε and permeability μ_0. Now applying the curl operator to (2.14), using (2.13) to eliminate $\underset{\sim}{H}$ and noting that $\underset{\sim}{B} = \mu_0 \underset{\sim}{H}$ and $\underset{\sim}{D} = \varepsilon \underset{\sim}{E}$ gives :

$$\nabla x (\nabla x \underset{\sim}{E}) = -\mu_0 \varepsilon \frac{\partial^2 \underset{\sim}{E}}{\partial t^2} \tag{2.17}$$

For any vector $\underset{\sim}{A}$

$$\nabla x (\nabla x \underset{\sim}{A}) = \nabla (\nabla . \underset{\sim}{A}) - \nabla^2 \underset{\sim}{A}$$

and using this, (2.16) and (2.17) results in :

$$\nabla^2 \underset{\sim}{E} = \mu_0 \varepsilon \frac{\partial^2 \underset{\sim}{E}}{\partial t^2} \tag{2.18}$$

In the planar guide the modes are uniform in the y direction so all derivatives with respect to y are zero. Assuming that $\varepsilon = n_i^2 \varepsilon_0$ where i = 1,2,3 field solutions of the form

$$E(x,y,z) = E_v(x,y)\exp(-j\beta_v z)$$

can be found and may be interpreted as modes of the waveguide with propagation constants β_v. The reduced form of the wave-equation is :

$$\frac{\partial^2 E_y}{\partial x^2} + (k_0{}^2 n_i{}^2 - \beta^2)E_y = 0 \tag{2.19}$$

The remaining requirement is that tangential E and H fields be continuous at the dielectric discontinuities. For TE modes the non-zero field components are E_y, H_x and H_z. (2.13) and (2.14) yield:

$$H_x = -\frac{\beta E_y}{\omega\mu_0} \tag{2.20}$$

and

$$H_z = \frac{j}{\omega\mu_0}\frac{\partial E_y}{\partial x} \tag{2.21}$$

For guided modes in slab waveguides power is largely confined in the central layer of the guide which is satisfied for an oscillatory solution in region 2 and evanescent tails in the cladding regions. The field solutions obtained are :

$$\begin{aligned} E_y &= A\exp(-p_1 x) \qquad x \geqslant 0 \\ &= A\cos(q_2 x) + B.\sin(q_2 x) \qquad 0 > x \geqslant -h \\ &= [A\cos(q_2 h) - B\sin(q_2 h)]\exp\{p_3(x+h)\} \quad x < -h \end{aligned} \tag{2.22}$$

where $\frac{A}{B} = -\frac{q_2}{p_1}$

p_1, q_2, p_3, are as defined by (2.8) and q_2 obeys the eigenvalue equation (2.10).

Similar forms of the wave-equation for the magnetic field $\underset{\sim}{H}$ may be derived from Maxwell's equations for TM modes.

Exact solutions of the eigenvalue equation (2.10) were obtained by a computer program listed in Appendix 9.2. For the case where n_1, n_2 and n_3 are real (lossless) the solution is obtained by continuous bisection in the range $(q-1)\pi < q_2 h < q\pi$ where q is the solution number. In the case where n_1, n_2 or n_3 are lossy the refractive index becomes complex and the substitution of (n-jk) for n in (2.10) gives a complex form of the eigenvalue equation. Numerical solution for the complex propagation constants also yields the attenuation constants of the guided modes. The computer program of Appendix 9.2 uses Newton's method to solve the complex form of (2.10).

2.2 Three-Dimensional Waveguides

2.2.1 Analysis of rectangular waveguides

Propagation in the slab waveguide structures described in section 2.1 has an exact mathematical solution. In many applications, however, transverse waveguiding (that is in the y direction) is also important. Examples of some of the types of these three-dimensional waveguides have been discussed by Kogelnik [26]. An exact analytical solution for such a structure is not possible and for a rigorous solution to the boundary value problem of a rectangular dielectric waveguide recourse must be made to numerical analysis and the use of a computer [27]. It is possible, however, to approximate the problem by replacing it with two or more planar problems as discussed in this section.

Consider the step-index rectangular waveguide configuration of Fig.2.4. The guiding region is the one with refractive index n_{m_1}. The propagation constant (β) for the

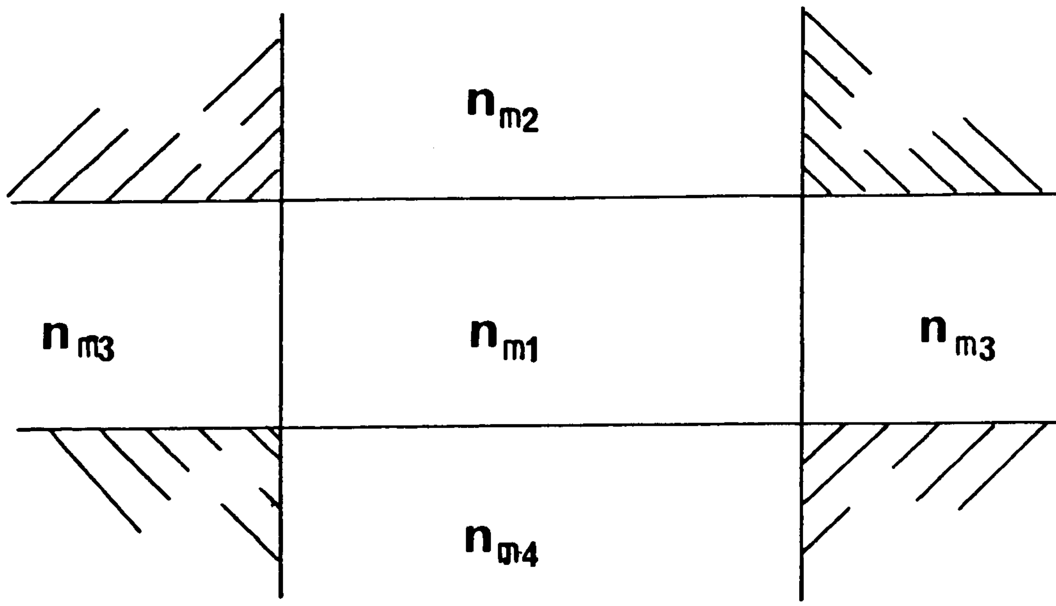

Fig.2.4 Waveguide cross-section subdivided for analysis by the method of Marcatili [28]. Region i is that with refractive index n_{mi}.

modes in this guide is given by :

$$\beta^2 = n_{m_1}^2 k_0^2 - q_x^2 - q_y^2 \tag{2.23}$$

where n_{m_1} is the refractive index of the waveguide core and q_x and q_y are the transverse propagation constants.

The approximate analysis of Marcatili [28] is based on the assumptions that field components in the two orthogonal directions are independent of each other and at the edges of the shaded regions of Fig.2.4 boundary conditions may be relaxed. The simplification arises from observing that for well guided modes the fields decay exponentially in regions 2-4. Therefore most of the power is contained in region 1, a small part in regions 2-4 and little in the four shaded regions. Clearly such an approximation holds only for modes well guided with most of the light energy travelling in the waveguide core.

Knox and Toulios [29] modified Marcatili's analysis for modes which are less well guided by using an effective refractive index to couple the two slab guides approximating the original rectangular structure. The method is illustrated in Fig.2.5 and was shown by the authors to give closer agreement than Marcatili's method to the computer analysis of Goell [27] near cut-off, a fact especially noticeable for low-order modes. In practice the technique involves firstly calculating the propagation constant of the slab guide formed if one lets the long guide dimension approach infinity (Fig.2.5 (b)). The propagation constant obtained (q_x) is used to define an effective refractive index, n_{eff_t}, through

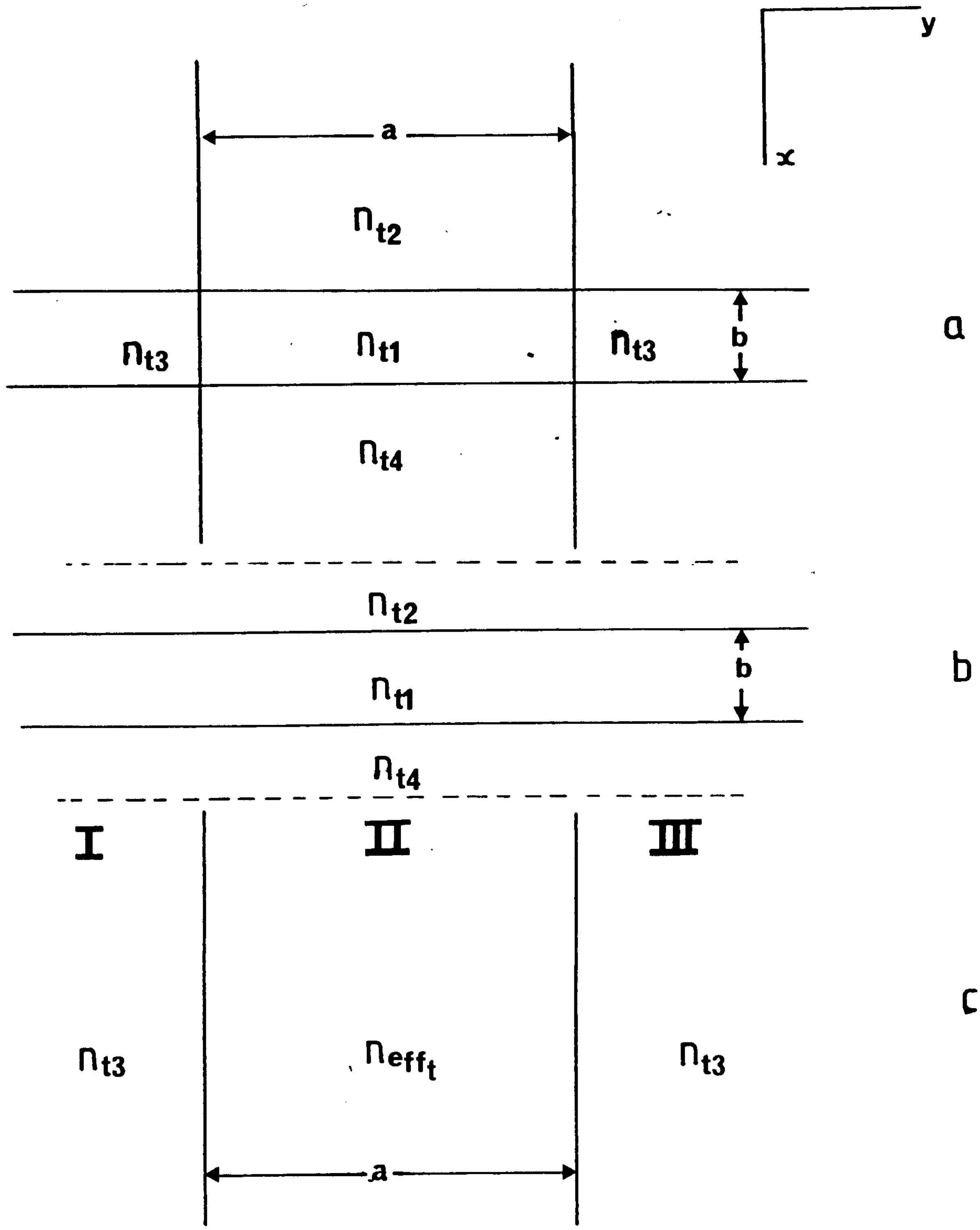

Fig.2.5 Analysis of a rectangular dielectric waveguide by the method of Knox and Toulios [29]

(a) Configuration of the waveguide
(b) Slab waveguide with equivalent confinement in the x direction
(c) Equivalent slab guide with confinement in the y direction. n_{eff_t} defined from (b).

$$n_{eff_t}^2 k_0^2 = n_{t_1}^2 k_0^2 - q_x^2 \qquad (2.24)$$

A second slab guide is now formed filled with a material of refractive index n_{eff_t} by allowing the short guide dimension to approach infinity (Fig.2.5(c)). The propagation constant of the slab guide so formed is taken as that representing the original waveguide.

A slightly different approach has been applied to strip-loaded guides by Furuta et al [30] and to metal-clad guides by Yamamoto et al [31] who both use an equivalent refractive index to reduce the structure to an equivalent rectangular waveguide suitable for analysis by Marcatili's method.

The effective index approach has been further developed by Itoh [32], McLevige et al [33] and Hamasaki and Nosu [34]. The assumption made by these authors is that if the aspect ratio of the waveguide is large there is much stronger confinement in the x direction shown in Fig.2.5 and in the waveguide core :

$$E_y(x,y) \sim E(y) \cos\{q_{xi}x + \phi_i\} \qquad (2.25)$$

where i = I, II, III corresponds to the regions illustrated in Fig.2.5(c).

The wave equation becomes :

$$\frac{d^2E_y}{dy^2} + (k_0^2 n_i^2 - q_{xi}^2 - \beta^2)\, E_y = 0 \qquad (2.26)$$

or using equation (2.24) :

$$\frac{d^2E_y}{dy^2} + (k_0^2 n_{eff_i}^2 - \beta^2) E_y = 0 \qquad (2.27)$$

Thus the problem is finally reduced to solving analytically the three dielectric slab regions (i = I, II, III), obtaining an effective index for each region which together form a lateral slab to be similarly solved. Intuitively a TM solution in this composite guide would appear to be the correct one but in practice there is very little difference between TE and TM solutions as generally one is working a long way from cut-off and the two modes are nearly degenerate.

The effective index analysis can be used in two ways depending on which lateral propagation constant is calculated first. A simple argument can be used to show that the method is particularly useful if there is a large field variation in one direction and a solution is first found for the larger transverse propagation constant in the direction of strongest guiding. The argument is based on the fact that the q_x and q_y terms in equation (2.23) may be regarded as perturbations on the $n_{m_1}^2 k_0^2$ term and in the effective index method the smaller of $q_{x,y}$ should be neglected to get a first-order approximation to β which is subsequently improved.

The effective index method will be used in later sections to analyse some waveguide properties. In particular the method is compared in section 6.1 with results from computer solutions for the case of rib waveguides of the configuration shown in Fig.2.6. This particular structure cannot be analysed directly by Marcatili's method because, although lateral waveguiding is observed, there is no physical refractive index change in the y direction.

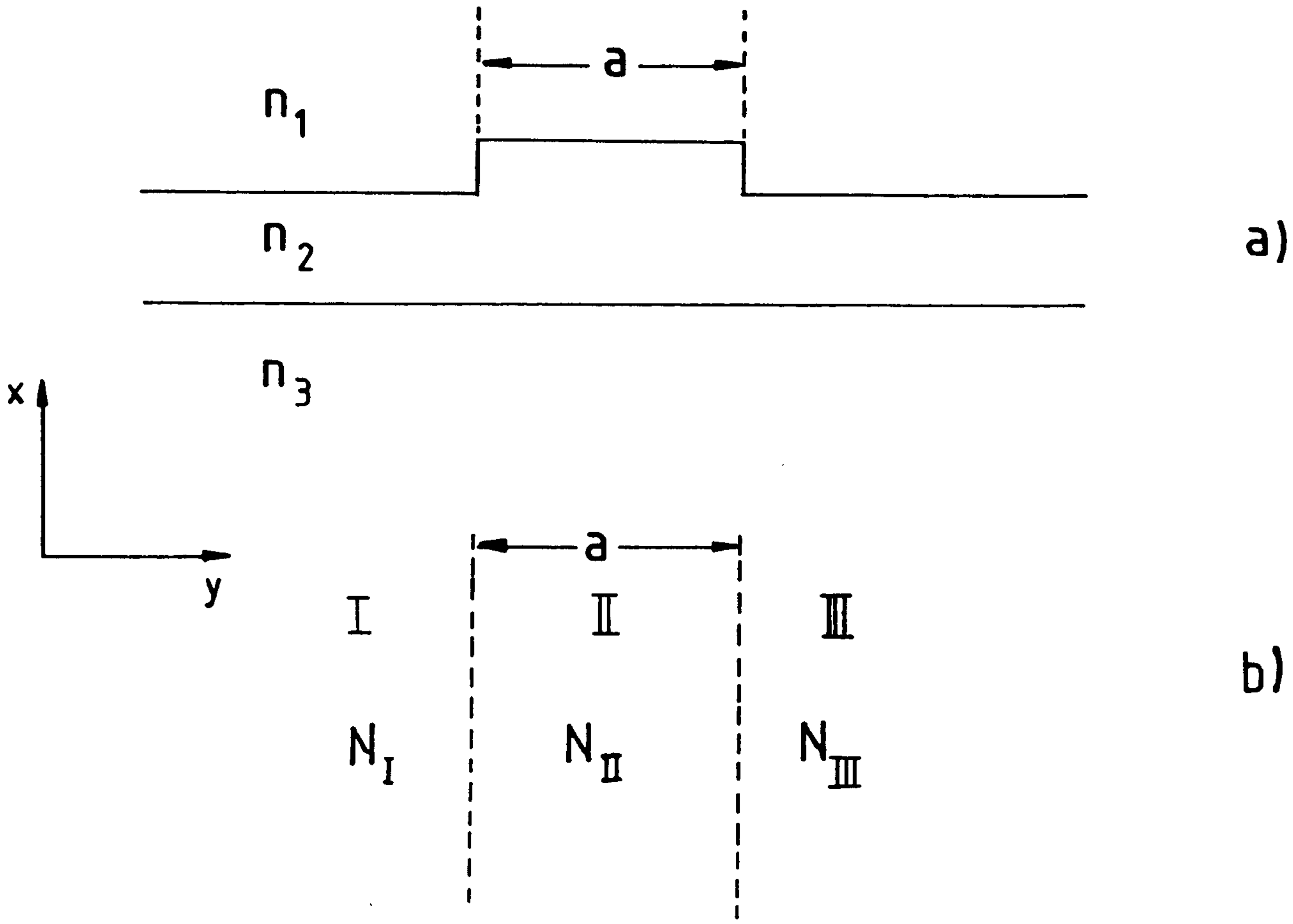

Fig.2.6 Analysis of a general rib waveguide by the effective index method.

Buus [35] has also demonstrated good agreement of the effective index method with a numerical method of calculation [36] for semiconductor lasers having a gradual lateral variation in complex permittivity.

2.2.2 Effective index analysis of directional couplers

An exact analytical solution for the coupling length of rib and strain-induced directional-coupler structures is not possible and again recourse must be made to a numerical method or an approximate model lending itself to analytical solution. A suitable approximation can be made using an extension of the effective index method.

The device is divided into regions I, II, and III shown in Fig.2.7 and, by assuming each region to be an infinite slab in the y direction, effective guide indices N_I, N_{II} and N_{III} can be obtained as β_i/k_o where β_i is the propagation constant of the fundamental TE mode for each slab guide.

The coupling length is calculated by modelling the five-layer structure of infinite extent in the x direction with indices N_i. The coupling length, L_c, is taken as $(\beta_S-\beta_A)/\pi$ where β_S and β_A are the propagation constants of the symmetric and asymmetric TM modes of the double-guide system (see Appendix 9.8). The characteristic equations for the symmetric and asymmetric modes are (see Appendix 9.3) :

$$\tan[2aq_2] = \frac{q_2\{\gamma_1 p_1+\gamma_3 p_3^{\star}\}}{\{q_2{}^2-\gamma_1\gamma_3 p_1 p_3^{\star}\}} \qquad (2.28)$$

where $p_3^{\star} = p_3\tanh\{p_3(c-a)\}$: symmetric mode

$= p_3/\tanh\{p_3(c-a)\}$: asymmetric mode

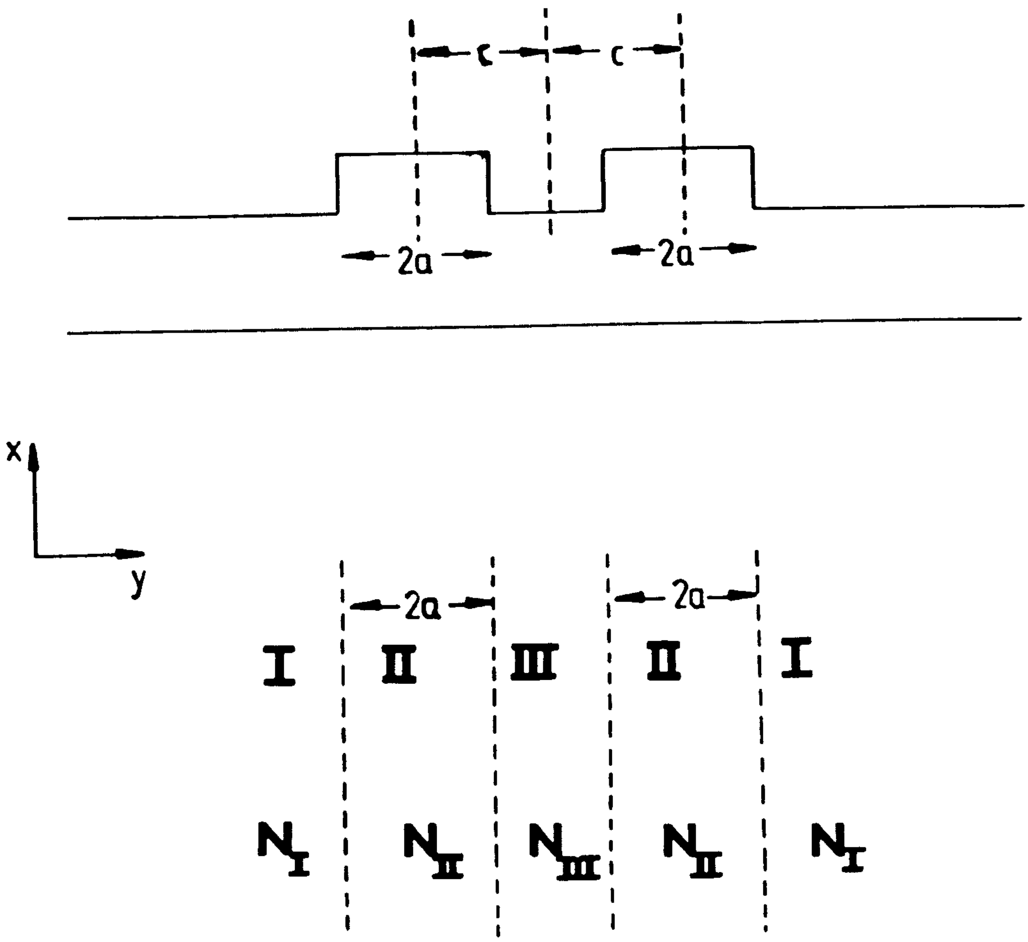

Fig.2.7 Analysis of a directional coupler by the effective index method.

$$\gamma_i = \left(\frac{N_{II}}{N_i}\right)^2 \qquad i = I, III$$

and

$$p_1^2 = \beta^2 - N_I^2 k_0^2$$

$$q_2^2 = N_{II}^2 k_0^2 - \beta^2$$

$$p_3^2 = \beta^2 - N_{III}^2 k_0^2$$

2.3 Finite Difference Calculations

A method is described in this section for analysing electromagnetic wave propagation in dielectric waveguides where refractive index may vary in both directions of the cross-section but is constant in the longitudinal direction (assumed infinitely long).

The basis of the procedure used is to replace the wave equation by finite difference relations in terms of the fields at discrete mesh points. Boundary conditions are enforced by enclosing the waveguide within an arbitrarily determined electric wall and full advantage taken of symmetry so that in most of the structures studied only half the waveguide cross-section is considered.

The finite difference techniques lead to a matrix eigenvalue problem and the construction of a computer program to calculate the field distribution and eigenvalue iteratively is described here in detail.

The importance of finite difference methods lies in the ease with which many operations and functions may be represented. Operations are then performed somewhat approximately in terms of values over a discrete set of points and as the distance between points is made sufficiently small it is hoped that the approximation made becomes increasingly accurate. As will become evident operations such as differentiation and integration reduce to simple arithmetic forms suitable for digital computation.

From equation (2.24) the wave equation for TE modes is :

$$\frac{\partial^2 E_y}{\partial x^2} + \frac{\partial^2 E_y}{\partial y^2} + k_0{}^2(n^2 - n_{eff}^2)E_y = 0 \qquad (2.29)$$

To apply the finite difference method the waveguide cross section is covered with a rectangular mesh of size X and Y in the x and y directions respectively. The different step lengths were incorporated to facilitate the study of devices with large aspect ratios. In place of the function $E_y(x,y)$ consider discrete values of E_y at mesh points only and replace the partial derivatives of (2.29) by the finite difference expressions of Appendix 9.4.

Rearrangement of these expressions gives :

$$E(I,J) = \frac{E(I+1,J)+E(I-1,J)+R^2\{E(I,J+1)+E(I,J-1)\}}{2[1+R^2]-k_0{}^2X^2-\{N^2(I,J)-N^2\}} \qquad (2.30)$$

where R = X/Y, N(I,J) is the refractive index at the point (IX,JY) and N is the effective refractive index of the guide.

Axes and dimensions were labelled as in Fig.2.8 giving a waveguide of dimensions AX and 2BY with a centre line of symmetry at J = 1. The following boundary conditions were imposed :

$$E(0,J) = E(A,J) = E(I,B+1) = 0 \qquad (2.31)$$

Symmetry about the centre line was modelled by requiring

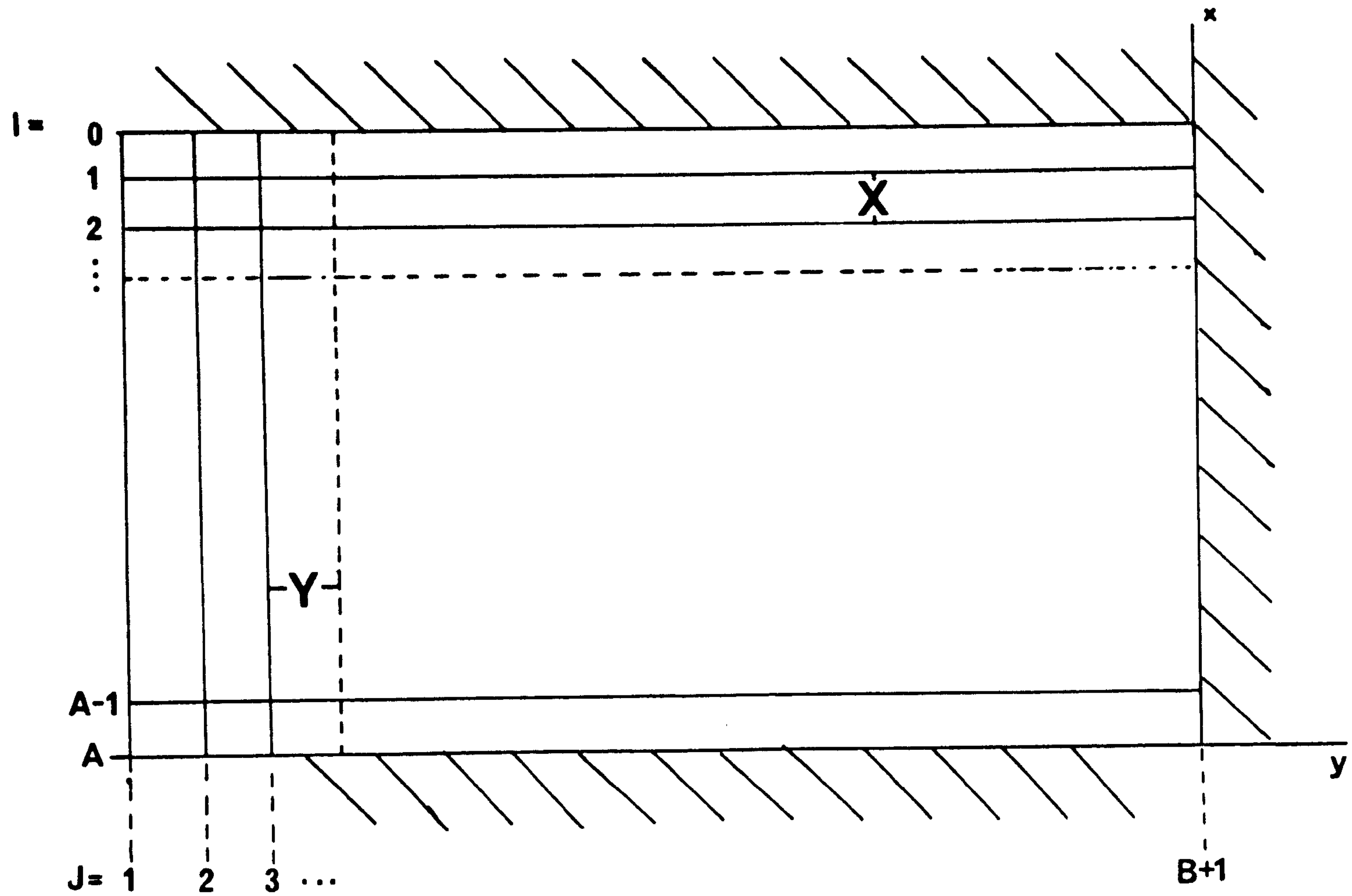

Fig.2.8 Definition of axes and mesh points for solution of the wave-equation by the finite difference method. The waveguide dimensions are AX and 2BY. J = 1 is the centre line of symmetry for the waveguide.

$$E(I,0) = E(I,2) \quad \text{for symmetric modes}$$
$$\text{and} \quad E(I,1) = 0 \quad \text{for asymmetric modes} \tag{2.32}$$

It is shown in Appendix 9.5 that a variational expression can be formed for the propagation constant $\beta(=N/k_o)$ of the waveguide that yields a lower bound for β^2 which improves as the trial function for E_y approaches the actual mode distribution. This variational expression is the Rayleigh Quotient and is :

$$k_o^2 N^2 \geq \frac{\iint_{\substack{\text{cross}\\\text{section}}} \left(\frac{\partial^2 E_y}{\partial x^2} + \frac{\partial^2 E_y}{\partial y^2} + k_0{}^2 n^2 E_y\right) E_y \, dxdy}{\iint_{\substack{\text{cross}\\\text{section}}} E_y{}^2 \, dxdy} \tag{2.33}$$

A finite difference form of the Rayleigh Quotient is also required. The integrand in the numerator is expressed as :

$$E(I,J)\left\{\frac{E(I+1,J) + E(I-1,J) - 2E(I,J)}{X^2}\right.$$
$$\left. + \frac{E(I,J+1) + E(I,J-1-2E(I,J)}{Y^2} + k_0{}^2 N(I,J)E(I,J)\right\}$$
$$= T(I,J) \text{ say} \tag{2.34}$$

The integration formula used to evaluate the numerator and the denominator was the "trapezoidal rule" [37] since the more accurate Simpson's 1/3 rule [37] was seen to give no improvement in the solution of one-dimensional waveguides. The trapezoidal rule gives :

$$\iint T(I,J)\,dxdy = \sum_{J=2}^{B}\sum_{I=1}^{A-1} T(I,J)XY + \sum_{I=1}^{A-1}\frac{T(I,1)}{2}XY$$

$$= C \text{ say} \qquad (2.35)$$

and

$$\iint E_Y^2\,dxdy = \sum_{J=2}^{B}\sum_{I=1}^{A-1}[E(I,J)]^2 XY + \sum_{I=1}^{A-1}\frac{E(I,1)^2}{2}XY$$

$$= G \text{ say} \qquad (2.36)$$

If the value of the numerator is C and that of the denominator G then from (2.33), (2.35) and (2.36) :

$$k_0^2 N^2 X^2 \geqslant \frac{CX^2}{G} \qquad (2.37)$$

from which a value of N can be substituted into (2.34).

In the practical solution of the wave equation the starting point was to draw up the mesh and assign a refractive index value to each mesh point. The eigenvalue was estimated (usually as N_3) and an approximate field value assigned to every point. In most cases E_Y was set initially to unity everywhere although better approximations speeded up convergence.

Equation (2.30) was then applied pagewise to each value in turn and field values overwritten. After each complete scan the latest field values were substituted into the Rayleigh Quotient from which a better approximation to the eigenvalue can be expected. The two processes were continued until a satisfactory convergence on field values or eigenvalue was attained.

2.3.1 <u>The method of successive over-relaxation</u>

The difference between any two successive E(I,J) values corresponds to a correction term to be applied in updating the current estimate. The rate of convergence may be speeded by overcorrecting at each stage by a factor S. The process is known as successive over-relaxation (S.O.R.) and may be shown to be convergent for any value of S in the range $0 \leqslant S \leqslant 2$ [38] with $S \geqslant 1$ over-relaxation results.

If over-relaxation is used the finite difference equation (2.34) is modified to [39]:

$$E(I,J) = S\left\{\frac{E(I+1,J)+E(I-1,J)+R^2\{E(I,J+1)+E(I,J-1)\}}{2[1+R^2]-k_0{}^2X^2\{N^2(I,J)-N^2\}}\right\}-(S-1)E(I,J) \tag{2.38}$$

The main difficulty in applying the idea of S.O.R. is the necessity for calculating the optimum accelerating factor (S_O) automatically within the computer program.

In Appendix 9.6 a brief outline is given of the theory behind the application of S.O.R. to the solution of (2.29) as given by Sinnott [40], Sinnott et al [41] and Carré [42]. A practical scheme is also presented there for efficiently calculating the optimum accelerating factor. S values found were in the range 1.6 - 1.9. The effectiveness of the method will become apparent in section 6.4.2 where a comparison is made of convergence with and without acceleration.

2.3.2 Higher-order modes

It is shown here that the modes of a dielectric waveguide are orthogonal which allows an arbitrary field distribution (ϕ) to be expressed as a superposition of the waveguide modes (ψ_r). This enables an approximation to higher-order mode solutions to be obtained.

2.3.2.1 Orthogonality of the waveguide modes

Orthogonality is easily proved by taking a pair of eigenfunctions ϕ_r and ϕ_s satisfying the wave equation. Then

$$\nabla^2\phi_r + (n^2-N_r^2)k_0^2\phi_r = 0 \tag{2.39}$$

$$\nabla^2\phi_s + (n^2-N_s^2)k_0^2\phi_s = 0 \tag{2.40}$$

Mulitplying (2.39) by ϕ_s and (2.40) by ϕ_r, subtracting and integrating over the waveguide cross-section

$$\begin{aligned}(N_s^2-N_r^2)k_0^2\iint\phi_r\phi_s dS \\ &= \iint(\phi_r\nabla^2\phi_s-\phi_s\nabla^2\phi_r)dS \\ &= \oint(\phi_r\frac{\partial\phi_s}{\partial n} - \phi_s\frac{\partial\phi_r}{\partial n})d\ell\end{aligned} \tag{2.41}$$

from Green's theorem.

The contour integral is zero if at least one of the modes is guided as guided mode field distributions are required to decay exponentially towards infinity and the line integral may extend over an infinitely large curve enclosing the waveguide. It follows that :

$$\iint\phi_r\phi_s dS = 0, \quad N_s \neq N_r \tag{2.42}$$

Orthogonality has been shown by Marcuse [43] to hold if both modes are radiation modes although the proof is somewhat more complicated and involves the oscillatory nature of the radiation modes.

For the case s = r solutions may be normalised in the usual way so that

$$\iint \phi_r \phi_s = \delta_{rs} \tag{2.43}$$

where δ_{rs} is the Kronecker delta, being unity for r = s and zero otherwise.

2.3.2.2 Higher-order modes

Consider a trial function $\phi(x,y)$ satisfying the boundary conditions of guided modes and having continuous derivatives up to second order. Expanding $\phi(x,y)$ in terms of the orthonormal solutions of the wave equation with the enforced symmetry as

$$\phi = \sum_{r=o}^{\infty} a_r \phi_r \tag{2.44}$$

and noting that

$$\nabla^2\phi + k_0{}^2 n^2 \phi = \sum_{r=o}^{\infty} a_r \phi_r \beta_r \tag{2.45}$$

a Rayleigh Quotient can be formed for the function $(\phi - a_o\phi_0)$ using (2.33) as

$$\beta^2 \geqslant \frac{\iint (\phi - a_0\phi_0)[\nabla^2\phi + k_0{}^2 n^2\phi - a_0(\nabla^2\phi_0 + k_0{}^2 n^2 \phi_0)]dS}{\iint (\phi - a_0\phi_0)^2 dS} \tag{2.46}$$

$$= \frac{\iint (a_1\phi_1 + a_2\phi_2 + \,..)(a_1\beta_1{}^2\phi_1 + a_2\beta_2{}^2\phi_2 + ...)dS}{\iint (a_1\phi_1 + a_2\phi_2 + ...)(a_1\phi_1 + a_2\phi_2 + \,....)dS}$$

Orthonormality of the ϕ_j leads to

$$\beta^2 \geq \frac{\sum_{r=1}^{\infty} a_r^2 \beta_r^2}{\sum_{r=1}^{\infty} a_r^2}$$

$$= \beta_1^2 + \frac{\sum_{r=2}^{\infty} a_r \ (\beta_r^2 - \beta_1^2)}{\sum_{r=1}^{\infty} a_r^2} \qquad (2.47)$$

Following the arguments of Appendix 9.5 a lower bound to the propagation constant of the next order mode with the required symmetry is found.

Thus, to determine the mode of propagation constant β_1 the function $(\phi - a_0\phi_0)$ is used in the Rayleigh Quotient. It is assumed that ϕ_0 is known to a sufficient accuracy from a previous finite difference solution.

The value of a_o may easily be determined. Since

$$\phi = a_o\phi_0 + a_1\phi_1 + \ldots.$$

it follows from orthonormality that :

$$a_o = \int \phi\phi_0 dV \qquad (2.48)$$

This technique is used in section 6.1 where a rib waveguide structure is analysed. If required, modes of higher order still can be found, provided all the lower-order modes of the relevant symmetry are known. This requires a large amount of computer storage, however.

2.3.3 Finite difference solution of the one-dimensional wave-equation

The wave equation for the TE modes is :

$$\frac{\partial^2 E_y}{\partial x^2} - (\beta^2 - n^2_{(x)} k_0{}^2) E_y = 0 \qquad (2.49)$$

In finite difference form with a step length h :

$$\frac{\partial^2 E_y}{\partial x^2} = \frac{E_{I+1} - 2E_I - E_{I-1}}{h^2} \qquad (2.50)$$

yielding

$$E_I = \frac{E_{I+1} - E_{I-1}}{(2-\lambda)} \qquad (2.51)$$

where $\lambda = k^2 h^2 (n^2(x) - n_e{}^2)$

and $n_e{}^2 = \beta^2 k_0{}^2$

For this problem, from (2.33) :

$$\beta^2 \geqslant \frac{\int_{-\infty}^{\infty} \left(\frac{\partial^2 E}{\partial x^2} + k^2 n^2(x)\right) E dx}{\int_{-\infty}^{\infty} E^2 dx} \qquad (2.52)$$

which is easily expressed in finite difference form using (2.50). The method is checked in section 6.4.1 against analytical solutions for slab waveguides and regions of constant refractive index. Integration was performed using the trapezoidal rule with E(o) = E(B+1) = 0 as boundary conditions. Integration using Simpson's rule gave little improvement to results.

CHAPTER 3

THIN FILM STRESSES AND THE PHOTO-ELASTIC EFFECT

3.1 Thin Film Stresses

3.1.1 Intrinsic and thermal stresses

Stress in epitaxial films consists of two major components [44]. One is "intrinsic" stress which reflects film structure in some way that is not well understood. Inconsistency between the experimental data of different workers indicates a dependence on film thickness, deposition temperature and condensation rate. The second component of stress dominates when the film thickness exceeds a few hundred angstroms [45] and arises from the different thermal expansion coefficients of the film and substrate and the difference between deposition temperature (T_D) and the temperature at which stress measurements are made (T_m).

If the expansion coefficient of the metal film is α_f and it were free to contract then its length $L_{x,y,z}$ along each axis (x,y,z) would change by an amount :

$$\Delta L_{x,y,z} = L_{x,y,z}\alpha_f(T_D-T_m) \qquad (3.1)$$

over the temperature range considered (in fact α_f varies slightly with temperature). Similarly the substrate would contract by :

$$\Delta L'_{x,y,z} = L_{x,y,z}\alpha_s(T_D-T_m) \qquad (3.2)$$

where α_s is the thermal expansion coefficient of the substrate.

Values of α_f for gold and aluminium are $1.4 \times 10^{-5} K^{-1}$ and $2.3 \times 10^{-5} K^{-1}$ respectively [46] and α_s for GaAs is $6 \times 10^{-6} K^{-1}$ [47].

The film is constrained from contracting and a strain is generated equal and opposite to the differential contraction. The strain components $e'_{xx,yy,zz}$ are given by :

$$\left.\begin{aligned} e'_{yy} &= e'_{zz} = -(\alpha_f-\alpha_s)(T_D-T_m) \\ e'_{xx} &= 0 \end{aligned}\right) \qquad (3.3)$$

The thin film stress (σ_f) is given approximately by :

$$\sigma_f = E_f \, e'_{zz} \qquad (3.4)$$

where E_f is Young's Modulus for the film. From the generalised Hooke's Law given in section 3.2 the stresses $\sigma_{xx,yy,zz}$ are :

$$\sigma_{xx,yy,zz} = \frac{\nu E' e}{(1+\nu)(1-2\nu)} + \frac{E' \, e'_{xx,yy,zz}}{1+\nu} \qquad (3.5)$$

where $e = e'_{xx} + e'_{yy} + e'_{zz} = \dfrac{1-2\nu}{E'}(\sigma_{xx}+\sigma_{yy}+\sigma_{zz})$,

E' and ν are respectively Young's Modulus and Poisson's ratio for the substrate. Letting $e'_{yy} = e'_{zz}$ and $e'_{xx} = 0$ gives

$$\sigma_{yy} = \sigma_{zz} = \frac{e'_{xx}E'}{(1+\nu)(1-2\nu)}$$

$$= \frac{-(\alpha_f-\alpha_s)(T_D-T_m)E'}{(1+\nu)(1-2\nu)} \qquad (3.6)$$

The distributed stresses σ_{yy} and σ_{zz} throughout the substrate balance the film stress σ_f i.e.

$$\sigma_f = \sigma_{zz} = \sigma_{yy}.$$

3.1.2 Experimental determination of thin film stresses

Stresses present in evaporated gold and aluminium films were measured by observing the curvature of long thin GaAs substrates, after film deposition, using a sodium interference microscope.

Flat GaAs samples for the interferometric measurements were prepared by thinning 400μm thick polished slices using a 1 : 8 : 1 water : hydrogen peroxide : sulphuric acid etch initially at room temperature. The samples were stuck polished side down to a glass slide using black wax and pre-etched in concentrated hydrochloric acid for about five minutes to remove surface oxide. After rinsing in de-ionised water and drying in a stream of nitrogen the samples were etched. The beaker containing the etchant was placed in an ultrasonic bath. With care to ensure that the wax protected the polished surface throughout the course of the etch the technique consistently produced samples with a uniform thickness in the range 75 - 125μm.

The flatness of the polished face of the substrates was checked before film evaporation and re-measured after etching off the film. The substrate was found to be unaltered in a control experiment in which it was heated by radiation from an evaporation source without any metal in it.

The measurement technique assumes that the evaporated film strains the substrate which bends until equilibrium is reached. For a film on the top side of a substrate a concave curvature is defined as tension in the film.

The product of film stress (σ_f) and its thickness (t) is given by [48]:

$$\sigma_f t = \frac{E'd^2}{6\rho(1-\nu)} \tag{3.7}$$

where ρ is the radius of curvature of the bent substrate and d its thickness. The radius of curvature is related to the deflection δ over length L by :

$$\rho = \frac{L^2}{2\delta} \tag{3.8}$$

Over the same length, δ is related to the lateral shift D in the sodium interference fringes as :

$$\delta = \frac{D\lambda}{2a} \tag{3.9}$$

where a is the fringe separation and λ the wavelength of sodium light. Fractional fringe shift could be measured from photographs taken over a 1mm section of the sample length.

For many samples the sodium interference microscope could be adjusted so that up to five Newton's Rings were observed over the field of view which could be photographed and in these cases the radius of curvature was also calculated from the radius of successive rings.

Brenner and Senderoff [49] review (3.7) in detail and point out several approximations made. These include different elastic moduli in film and substrate and stress relief in the film as curvature changes. Experimentally stresses measured in films evaporated onto substrates constrained from bending during evaporation (by sticking their reverse side to a glass slide with photoresist) were the same as those measured on similar unconstrained substrates. Brenner and Senderoff also develop corrections to (3.7) for cases where film thickness is an appreciable fraction of substrate thickness. The worst error due to this in samples studied is 3%.

The discussion above assumes that stress is uniform throughout the film thickness. However it was observed that films peeled off some substrates and devices curled away from the substrate indicating that film stress is not uniform. Stress values found must therefore be regarded as some average value.

Any thermal gradients across the substrate thickness would induce a bending of the film-substrate combination which may be interpreted as a stress. However, the temperature difference between the two sample faces was estimated as being less than $1^{\circ}C$.

Evaporation rate was kept constant by using the same source current although gold tended to run into the corners of the source boat which it is thought are cooler than the central part.

3.1.3 Experimental results and discussion

Fig.3.1 shows the experimental plot of $\sigma_f t$ against film thickness t for an evaporated gold film. Approximating the plot with a straight line gives a value of $\sigma_f = 3.5 \times 10^8$ Nm^{-2}. Using equation (3.6) this corresponds to a temperature difference $(T_D - T_m) \approx 230^{\circ}C$. For evaporated aluminium films the film stress increased with increasing film thickness up to a maximum value of $\sim 1 \times 10^8 Nm^{-2}$ for a $2\mu m$ thickness. The

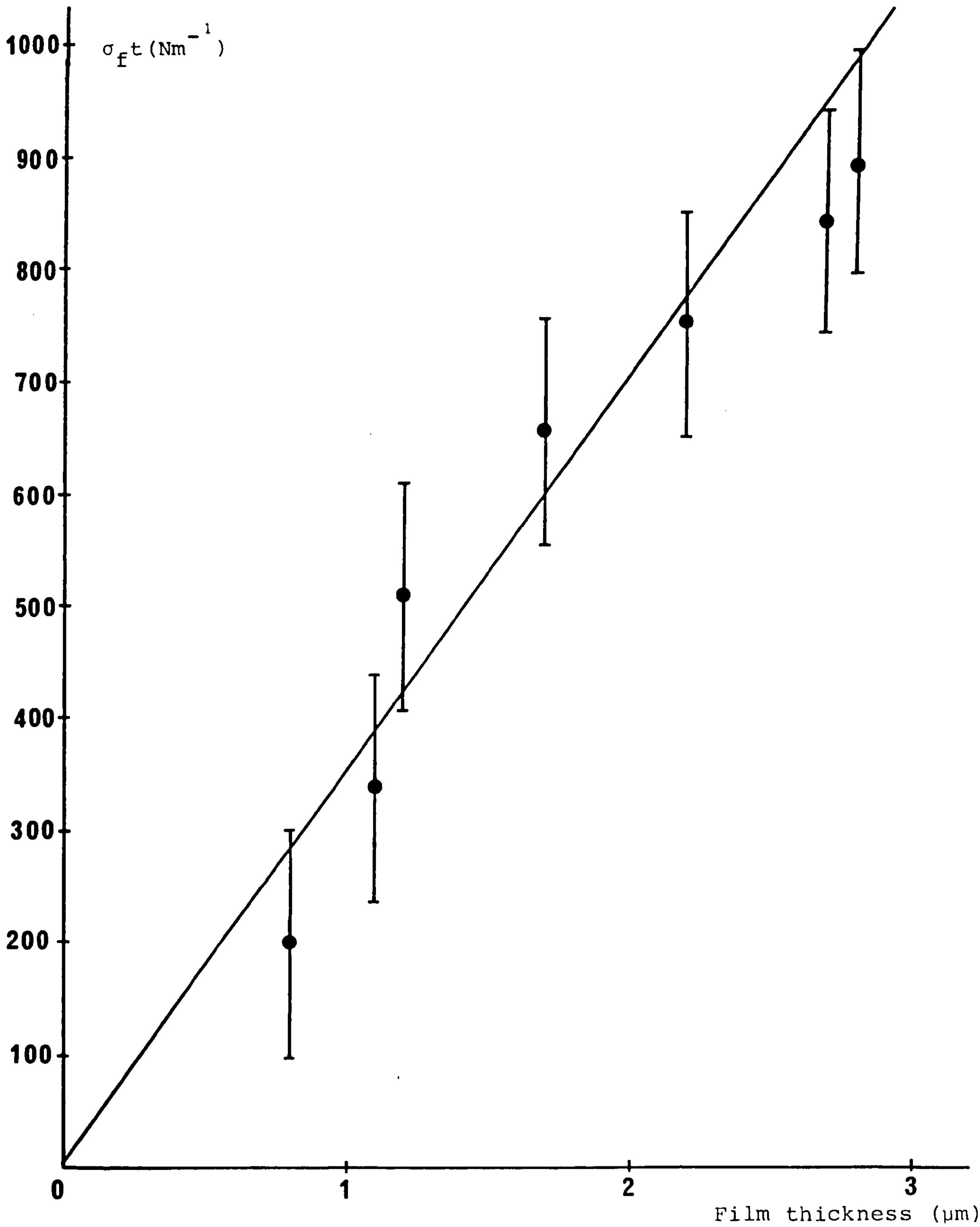

Fig. 3.1 Plot of film stress-film thickness product against film thickness for gold films evaporated on to GaAs substrates

corresponding $(T_D - T_m)$ from (3.6) is $\approx 30^{o}C$. The temperature T_D at which the film forms is determined by thermal radiation from the evaporation source and latent heat given up by the condensing atoms. Maximum temperatures measured during evaporations of 1μm of gold and 2μm of aluminium were $195^{o}C$ and $50^{o}C$ respectively, in favourable agreement with calculated values. Temperature measurements were made using a Johnson Matthey "Thermafilm" platinum resistance thermometer.

The difference $(T_D - T_m)$ was increased by evaporating onto samples heated by placing them on a small metal block attached to a soldering iron heating element. The block temperature was determined using a copper-constantan thermocouple and could be varied by altering the heating-element voltage. A Peltier cooling element was used to cool samples during evaporation. Cooling of $30^{o}C$ was achieved and maintained during evaporation of aluminium films. Films with no measurable stress could be formed. Two samples showed small compressive stresses.

Fig.3.2 shows a plot of film stress against temperature prior to evaporation for 1μm thick aluminium films. An increase of film stress with temperature is observed at least up to about $110^{o}C$. Although it is tempting to assume that a constant stress value of $2.9 \times 10^{8} Nm^{-2}$ is reached for higher temperatures (which would be in agreement with the results of Fig.3.1) as shown by the solid curve of Fig.3.2, it is evident that in view of measurement errors a curve such as the dotted one in this Figure could be drawn, indicating

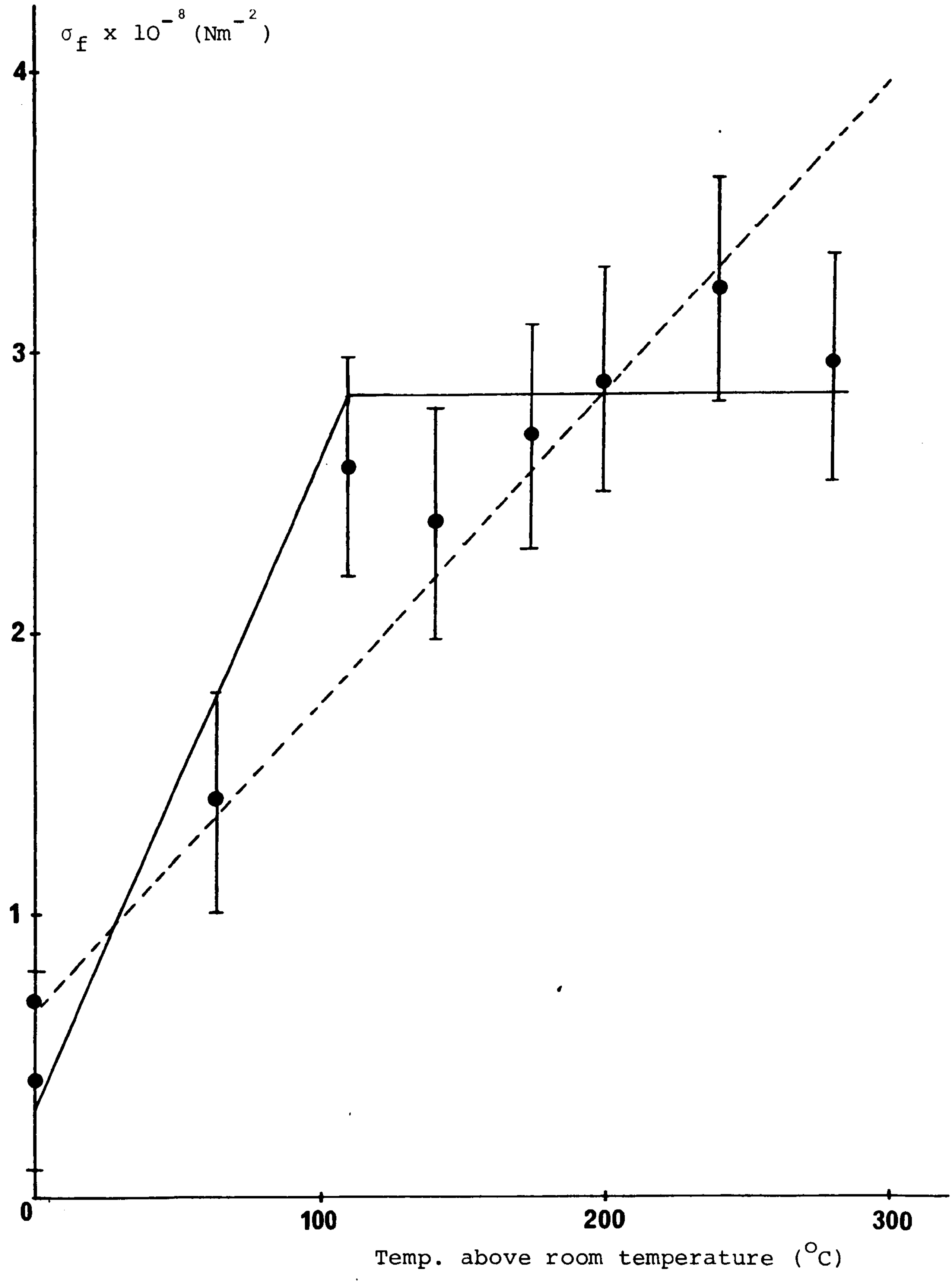

Fig. 3.2 Measured stress as a function of substrate temperature above room temperature for aluminium films 1μm thick evaporated on to GaAs substrates

stress increases with temperature up to 300°C.

The experimental results of Fig.3.1 and those of Fig. 3.2 using the solid curve agree closely with the interpretation of Murbach and Wilman [50] who state that appreciable atomic migration persists in the film until the temperature falls below the recrystallisation temperature. On further cooling the mechanical properties of the film return and cause the observed tensile stress. The amount of stress developed depends therefore on the difference between the recrystallisation temperature, or the highest temperature reached if less than this, and the final temperature (T_m). The recrystallisation temperatures of Al and Au are 150°C and 200°C [50] and the corresponding stresses compare favourably with those observed experimentally.

It should be remembered, however, that no direct observation of film structure has been made so there is no direct evidence that recrystallisation does in fact occur. As the film stress is larger than the yield stress of bulk material its value might be determined by the yield strength at the deposition temperature and subsequent hardening on cooling. Haworth [51] says these are, however, conditions under which recrystallisation may occur. Neugebauer [52] does report orientation approaching that of a single crystal for gold films deposited at $\sim$300°C on a rock-salt substrate but completely random structure for deposition at temperatures less than 150°C. He also shows that a stress-strain curve for the evaporated films has a gradient slightly smaller than Young's Modulus for low stress but which remains steep even for high stresses. He concludes that this is due to a high concentration of dislocations and other defects impeding but not preventing dislocation motion even at high stresses. This also explains an ultimate tensile strength larger than in bulk material. Although plastic deformation was observable at stresses very much less than the tensile stress, Neugebauer reports that there is no sharp yield point.

It is evident that this part of the study needs further careful experimental work to satisfactorily explain the results. In particular a study of film structure is necessary.

In a further experiment an already evaporated sample having a gold film was heated using the heating block whilst observing fringes formed with the sodium interference microscope. The sample temperature is assumed to be that of the heating block. A linear plot of $\sigma_f t$/temperature was found up to the maximum temperature used of 90^oC. Extrapolation predicted $\sigma_f t = 0$ at a temperature of $\sim 240^oC$ which can be interpreted as the temperature at which tensile stress was first developed.

Annealing of samples with evaporated gold films at temperatures of 80^oC, 140^oC and 200^oC produced on the whole no change in film stress. The temperatures used were chosen as representative of those to which the device is subjected during fabrication whilst avoiding the appreciable atomic diffusion of a gold/GaAs system above 250^oC [53] which may cause stress relief. Samples removed from the evaporator before cooling to room temperature showed stress some 20% larger than expected but this extra component was rapidly removed on annealing.

Attempts made to evaporate metal films onto samples initially cooled to near 77K by placing them on a stainless steel reservoir containing liquid nitrogen were unsuccessful. Both aluminium and gold condensed into long, fine "whiskers" between source and samples.

3.2 Strain Due to Discontinuities in the Metal Films and the Photo-elastic Effect

In this section the effect of the metal stress on substrate refractive index near discontinuities in the metal film is examined.

Consider the discontinuity in a thin film under tension as illustrated in Fig.3.3. To maintain equilibrium a force F per unit length in the z direction is transmitted into the crystal at the discontinuity. This force is strictly distributed in a small region near the film edge but is considered here to be concentrated directly at the edge. The force is given by :

$$F = \sigma_f t \tag{3.10}$$

If the semiconductor is assumed elastically isotropic and semi-infinite in the x direction the required stress components in the GaAs are given by [54] :

$$\sigma_{xx} = -\frac{2F}{\pi}\frac{x^2 y}{(x^2+y^2)^2} \tag{3.11}$$

$$\sigma_{yy} = -\frac{2F}{\pi}\frac{y^3}{(x^2+y^2)^2} \tag{3.12}$$

$$\sigma_{xy} = \sigma_{yx} = -\frac{2F}{\pi}\frac{xy^2}{(x^2+y^2)^2} \tag{3.13}$$

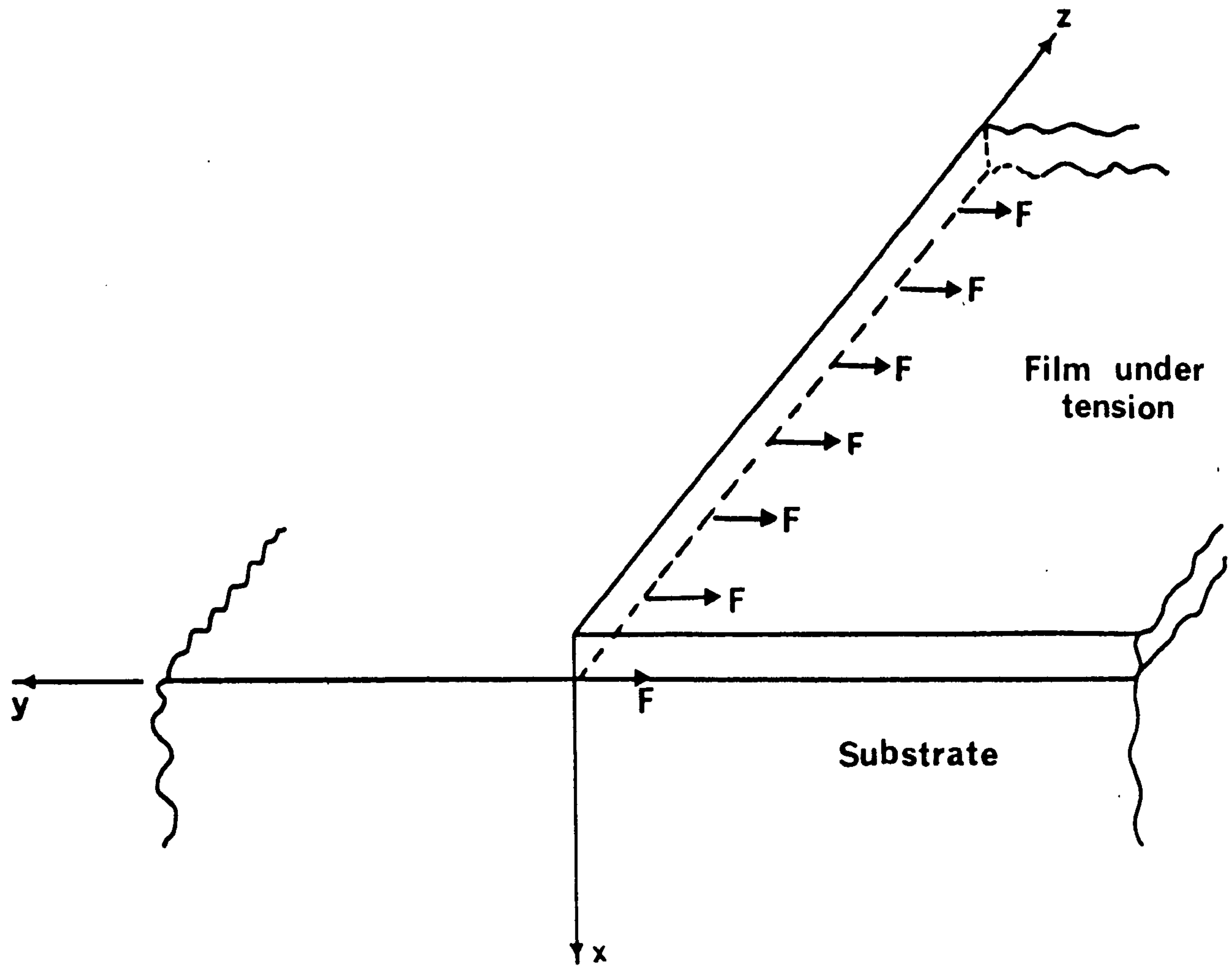

Fig.3.3 The edge forces resulting from a discontinuity in a thin film under tension.

To find the related strain components a generalised Hooke's Law is used giving [55] :

$$e_{xx} = \frac{1}{E'} \{\sigma_{xx} - \nu(\sigma_{yy} + \sigma_{zz})\} \tag{3.14}$$

$$e_{yy} = \frac{1}{E'} \{\sigma_{yy} - \nu(\sigma_{xx} + \sigma_{zz})\} \tag{3.15}$$

$$e_{zz} = \frac{1}{E'} \{\sigma_{zz} - \nu(\sigma_{xx} + \sigma_{yy})\} \tag{3.16}$$

In practice cubic crystals such as GaAs and InP are elastically anisotropic. Isotropic average values for E' and ν are taken in the treatment used.

If the thin film discontinuity is assumed infinite in the z direction, implying no displacement in that direction (i.e. $e_{zz} = e_{xz} = e_{yz} = 0$), then from (3.16) :

$$\sigma_{zz} = \nu(\sigma_{xx} + \sigma_{yy}) \tag{3.17}$$

and substitution into (3.14) and (3.15) gives :

$$e_{xx} = \frac{(1+\nu)}{E'} \{(1-\nu)\sigma_{xx} - \nu\sigma_{yy}\} \tag{3.18}$$

$$e_{yy} = \frac{(1+\nu)}{E'} \{(1-\nu)\sigma_{yy} - \nu\sigma_{xx}\} \tag{3.19}$$

If there are two or more discontinuities in the metal film the strain components at a general point (x,y) may be found by superimposing strain components found for each discontinuity considered in turn.

The photo-elastic effect describes the dependency of the dielectric constant (and refractive index) on strain. The effect of the strain is to alter the relative dielectric impermeability tensor B_{ij} defined as [56] :

$$B_{ij} = \varepsilon_0 \frac{\partial E_i}{\partial D_j} \tag{3.20}$$

by an amount [57] :

$$\Delta B_{ij} = p_{ijrs} . e_{rs} \tag{3.21}$$

where the p_{ijrs} are coefficients of the fourth rank photo-elastic tensor.

For TM waves (polarisation in the x direction) the refractive index n_{xx} is given by :

$$\frac{1}{n_{xx}^2} = (\frac{1}{n_0^2} + p_{xxrs} . e_{rs}) \tag{3.22}$$

As ΔB is small compared to B this equation may be expanded to first order giving :

$$n_{xx} \sim n_0 - \frac{1}{2} p_{xxrs} . e_{rs} n_0^3 = n_0 + \Delta n \tag{3.23}$$

The perturbation in relative dielectric constant is :

$$\Delta\varepsilon_r = 2n_0 \Delta n = -n_0^4 p_{xxrs} . e_{rs} \tag{3.24}$$

Similarly for TE waves (polarisation is the y direction) :

$$\Delta\varepsilon_r = -n_0^4 (p_{yyrs} . e_{rs}) \tag{3.25}$$

For the $\bar{4}3m$ crystals (such as GaAs and InP) there are three independent photo-elastic constants p_{11}, p_{12} and p_{44} (using reduced matrix notation [56]). These constants are given in the literature for GaAs but are referred to the primary crystallographic axes (x',y',z'). Therefore to determine the coefficients referred to the axes of the device a tensor transformation must be applied [24]. The relationship between the two sets of axes is shown in Fig.3.4. The x axis is coincident with the x' but the y and z axes are rotated through 45° with respect to the y' and z' axes. The photo-elastic contribution to relative dielectric constant is then, for TM modes :

$$\Delta\varepsilon_r = -n_0^4 (p'_{11} e_{xx} + p'_{12} e_{yy}) \qquad (3.26)$$

and for TE modes :

$$\Delta\varepsilon_r = -n_0^4 \{p'_{12} e_{xx} + (p'_{44} + \frac{p'_{11} + p'_{12}}{2}) e_{yy}\} \qquad (3.27)$$

The non-zero photo-elastic coefficients of GaAs are [58] $p'_{11} = -0.165$, $p'_{12} = -0.140$ and $p'_{44} = -0.072$. No photo-elastic coefficients have been reported for InP although some information on them can be found from published data on the piezobirefringence of the material [59]. The photo-elastic coefficients are related to the piezo-optic coefficients π'_{ij} by :

$$p'_{ik} = \sum \pi'_{ij} \, c'_{jk} \qquad (3.28)$$

where the c'_{jk} are the elastic stiffness constants. From the data of Canal et al [59] (3.28) gives $p'_{11} - p'_{12} = -0.007$ and $p'_{44} = -0.051$ for InP at a wavelength of 1.15μm using values for the c'_{jk} quoted by Neuberger [60]. Values of $p'_{11} - p'_{12} = -0.036$ and $p'_{44} = -0.065$ from similar piezobirefringence measurements for GaAs [61] are in reasonable agreement with the p'_{ij} of Dixon [58]. At the wavelength used the p'_{ij} values for InP and GaAs are thought similar, therefore. The sign of π'_{44} and $(\pi'_{11} - \pi'_{12})$ reverses for both GaAs and InP near the respective absorption edges, however.

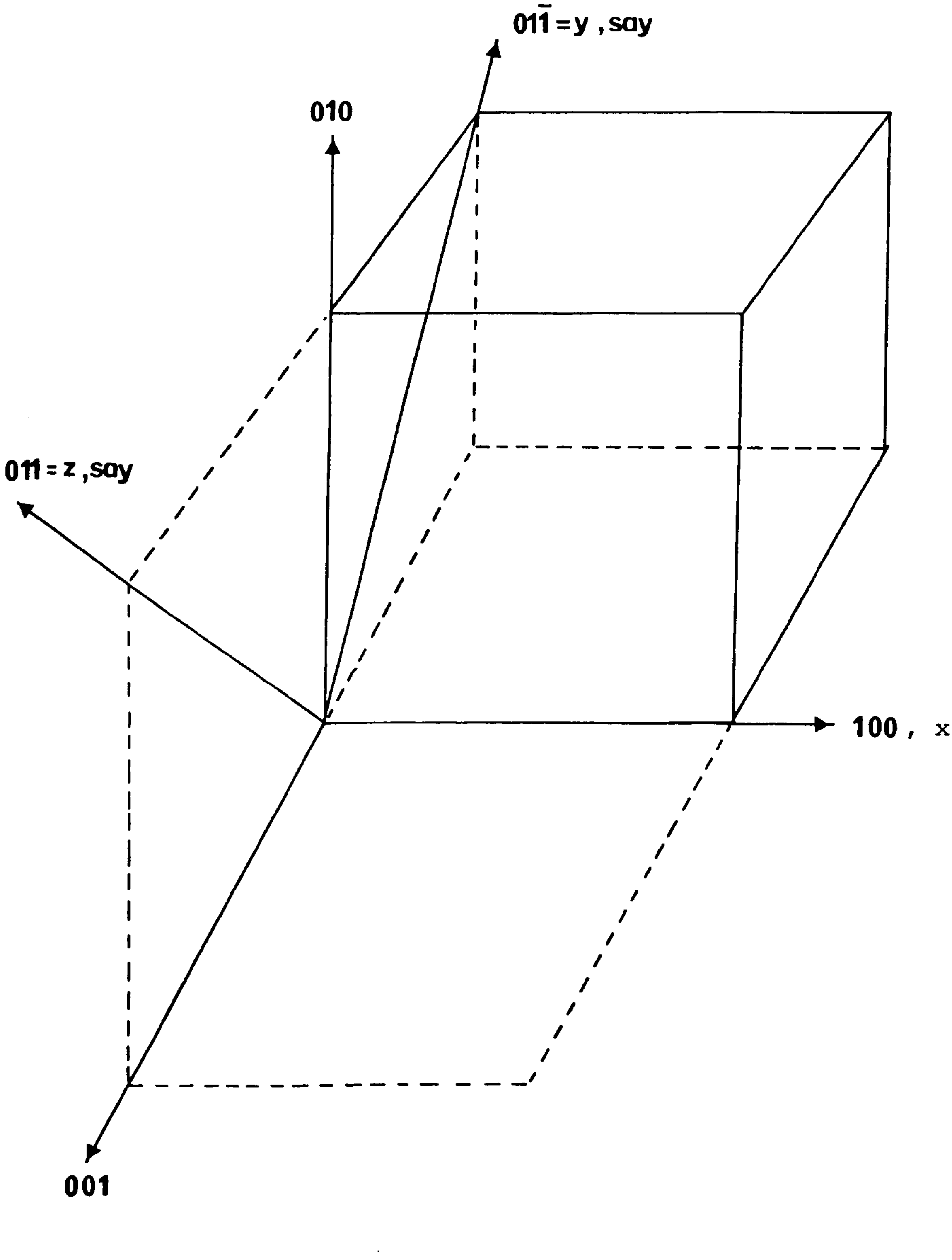

Fig.3.4 The relationship between x, y, z axes used and the primary crystallographic axes.

The effect of the strain on the dielectric constant is illustrated by Fig.3.5 which shows the variation of ε_r with y for a TE mode at depths of 1, 2 and 4μm below a 14μm wide channel with $F = 1200\ Nm^{-1}$ and a GaAs substrate*. It is clear that the dielectric constant perturbation decreases rapidly with increasing depth but it should be remembered that the optical fields are contained within the first few microns of the device by the free-carrier contribution to refractive index in the n^+ substrate.

Analysis of the waveguiding characteristics of strain-induced refractive index profiles produced using several metal film geometries is given in Chapter 6.

---

*Average values of E' and ν for GaAs are [24] $1.2 \times 10^{11} Nm^{-2}$ and 0.23 respectively.

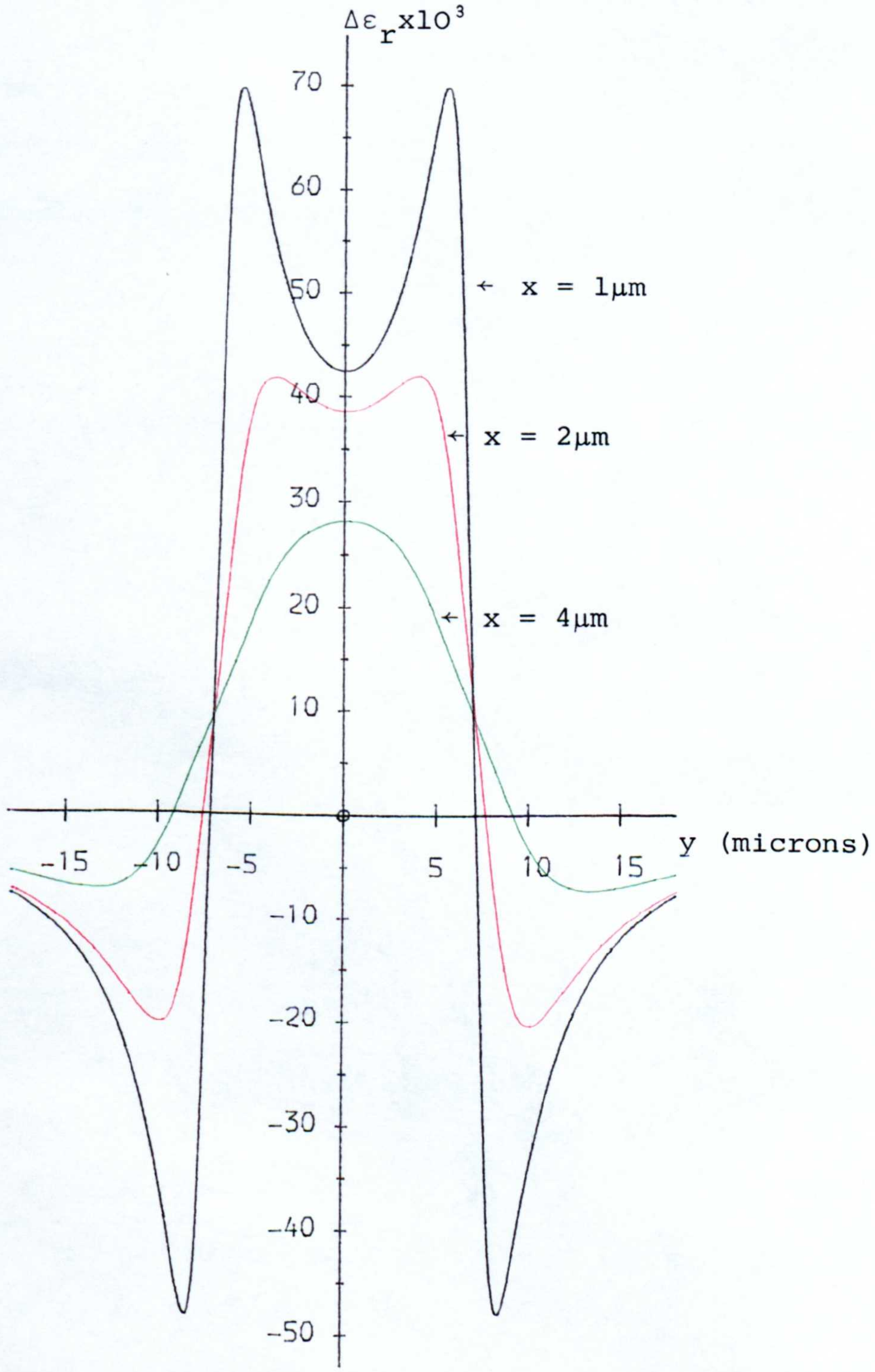

Fig.3.5 The variation of ε_r with y for TE polarised waves at depths of 1, 2 and 4μm produced beneath a 14μm slot (F = 1200Nm^{-1}).

CHAPTER 4

DEVICES AND THEIR FABRICATION

4.1 GaAs Devices

The material used in the fabrication of GaAs devices had a lightly-doped GaAs epitaxial layer grown on a heavily-doped n^+ GaAs substrate ($N_d \sim 10^{18} cm^{-3}$). Several slices were used with slightly different doping in the epitaxial layer.

The following initial stages of processing were identical for all GaAs devices :

(a) The wafers were stuck to a lapping block with dental wax and lapped on a glass plate to a total thickness of 120μm using an aqueous suspension of 3μm alumina grit. A finer (1μm) grit mixed with glycerol was then used to get a finish with a dull shine. The 120μm thickness was chosen as the best compromise to provide a sample both easy to cleave and handle.

(b) The epitaxial layer surface was cleaned by rubbing gently with strands of cotton pulled from a cotton bud and soaked in trichloroethylene. The whole wafer was then cleaned by boiling in a succession of solvents, usually three times each in trichloroethylene, acetone and iso-propyl alcohol. Each solvent in turn was allowed to boil for a few minutes before introducing the sample which was then left for 2-3 minutes.

(c) Some slices required the epitaxial layer thickness to be reduced to a final value of about 2.7μm. This was done using a 1 : 8 : 1 (H_2SO_4 : H_2O_2 : H_2O) etch cooled to room temperature before use and agitated by placing the beaker containing the etch into an ultrasonic bath. When preceded by a 5 minute etch in HCl to remove surface oxide [62] an etched surface indistinguishable from the original epitaxial surface resulted. The etch rate at 17^{o}C was 7.4μm/minute.

(d) In devices requiring subsequent electrical contact to the Schottky electrodes a gold-germanium ohmic contact with 6% nickel by weight as a wetting agent was evaporated onto the n^+ substrate. The total weight of the evaporation sources was usually about 0.4g but all was not evaporated as the evaporants alloyed with the molybednum boat used. The contacts were subsequently alloyed for 2 minutes in a furnace set to a temperature of 450^{o}C through which pure hydrogen gas was passed. The sample was held on a quartz boat incorporating a thermocouple. Alloying was timed from when monitored temperature exceeded 400^{o}C.

(e) Wafers were then cleaved into individual samples as required. The natural $\{110\}$ cleavage planes were exploited. Cleaving was performed by trapping the remote edge of the sample with the point of a fine pair of tweezers. The body of the tweezers was pointed along the direction to be cleaved but making an angle of about 45^{o} with the plane of the slice. Light pressure on the point of the tweezers then caused the sample to lift slightly and cleave in the required place.

The following sections describe briefly the subsequent fabrication of the various devices studied.

4.1.1 Stripe waveguides

A device studied by Westbrook [24] and called the electro-optic waveguide modulator by him has been further investigated and will be referred to as a stripe waveguide.

The ideal structure is shown in Fig.4.1(a). The stripe width is typically 20-30μm and consequently inhibits direct bonding of a contact wire. Therefore in devices requiring an electrical contact a wider stripe, isolated from the semiconductor surface by a layer of negative photoresist, was provided for bonding purposes giving the structure of Fig.4.1(b).

Further processing for this structure was :-

(i) A stripe window of the required width was opened up parallel to the cleaved sample edges in Waycoat H.R. negative photoresist spun on the sample at 8000 r.p.m. for 30s. The high spin speed was used to avoid build-up of the resist near sample edges. Placing the sample off-centre on the spinner was also helpful in this respect. To give the samples extra strength they were stuck onto 2.5 cm square microscope cover slips with a thin layer of positive photoresist spun for a few seconds at 6000 r.p.m. Adhesion to the slide was improved by baking at 60°C under an infra-red (I.R.) lamp.

The negative photoresist was baked at 90°C for 30 minutes before exposure to U.V. light through a suitably aligned mask using a KSM mask aligner system. An exposure time of 3s was followed by development under a flow of xylene from a wash bottle. The sample was next removed from the glass slide

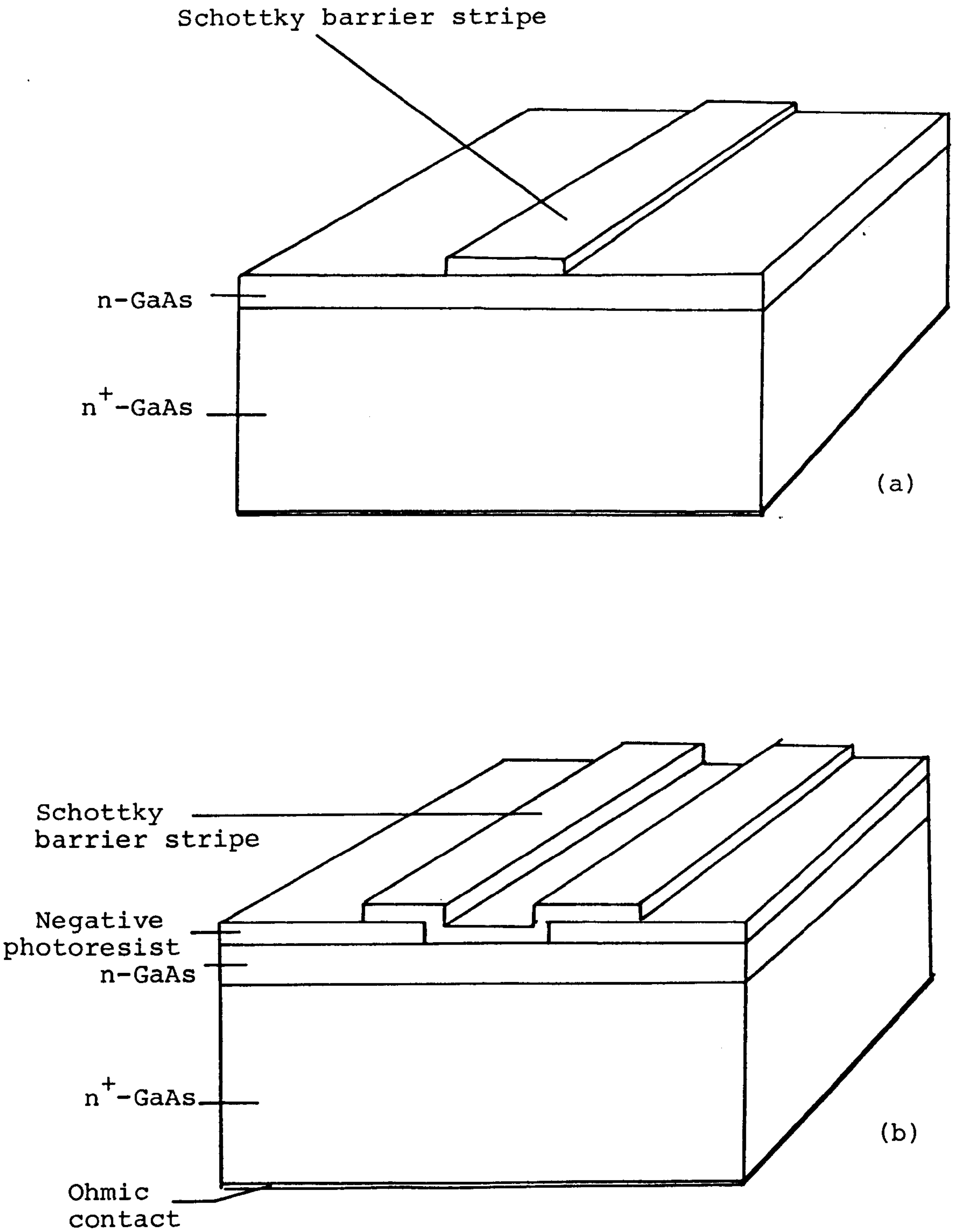

Fig.4.1 Schematic diagram of the stripe waveguide

(a) shows the ideal device while (b) illustrates the electrically active structure with a contacting strip for application of bias.

by soaking for a few seconds in ethyl acetate and sprayed with n-buthyl acetate to ensure complete removal of the negative photoresist from the window. The photoresist was subsequently baked for 20 minutes at 135°C.

(ii) A gold Schottky barrier film was evaporated onto the epitaxial layer after a 5 minute etch in HCl to remove surface oxide. The evaporation was performed at a residual pressure of <2.7 x 10^{-4} Pa (2 x 10^{-6} torr). A fired molybdenum boat containing melted gold wire provided the source. The thickness t of the evaporated film was estimated from :

$$t = \frac{m}{2\pi r^2 \rho} \tag{4.1}$$

where m is the mass of evaporant, r the source-substrate distance and ρ the density of the metal. Subsequent measurement of film thickness using a "Talystep" showed actual thickness to be 1.5 times larger than that predicted when all source material was evaporated.

(iii) The sample was stuck to another glass slide with positive photoresist and AZ1350H positive photoresist spun onto the surface at 8000 r.p.m. for 30s. A 100μm mask was delineated over the stripe window. A 5 minute pre-bake under an I.R. lamp and a 15s exposure were used. The sample was developed in a beaker containing AZ developer until the stripe became visible (after 5-10s). The sample was then rinsed well in de-ionised water and blown dry in a stream of nitrogen.

(iv) Exposed gold was removed using a solution of potassium iodide/iodine (KI/I_2). The positive resist was next removed by soaking in ethyl acetate and this also removed the device from the cover slip.

(v) The device was cleaved and mounted as described in section 4.3.

It was shown in section 3.2 that the photo-elastic effect produces guiding at a remote metal edge. Edge waveguides were fabricated by evaporating gold directly onto the epitaxial layer as in (ii) and then delineating and etching 100-200μm stripes as in (iii) and (iv). Direct bonding to the stripe is possible.

4.1.2 Channel waveguides - novel directional-coupler structures

Channel structures were fabricated by evaporating gold onto the semiconductor surface and etching through windows in negative photoresist spun over the metal. The resist was then removed using "Microstrip" a proprietory resist stripper. With the thicker films severe undercutting of the photoresist was noticed. For example, a 15μm channel would be formed when etching a nominal 2μm film through a mask 7μm wide. By carefully controlling the etching time in the KI/I_2 solution line widths were found to be reproducible although photolithography did not always succeed in giving the narrow window required for an etched channel width of 7μm.

As demonstrated in Chapter 6 channels of intermediate width show directional-coupler action. In these devices the total metallised area was reduced by covering the channel and surrounding gold with a positive resist stripe 100-200μm wide and further etching. Extra electrodes for applying bias in the $\Delta\beta$ configuration were formed by another photolithographic and etching stage. This device is illustrated in Fig. 4.2 .

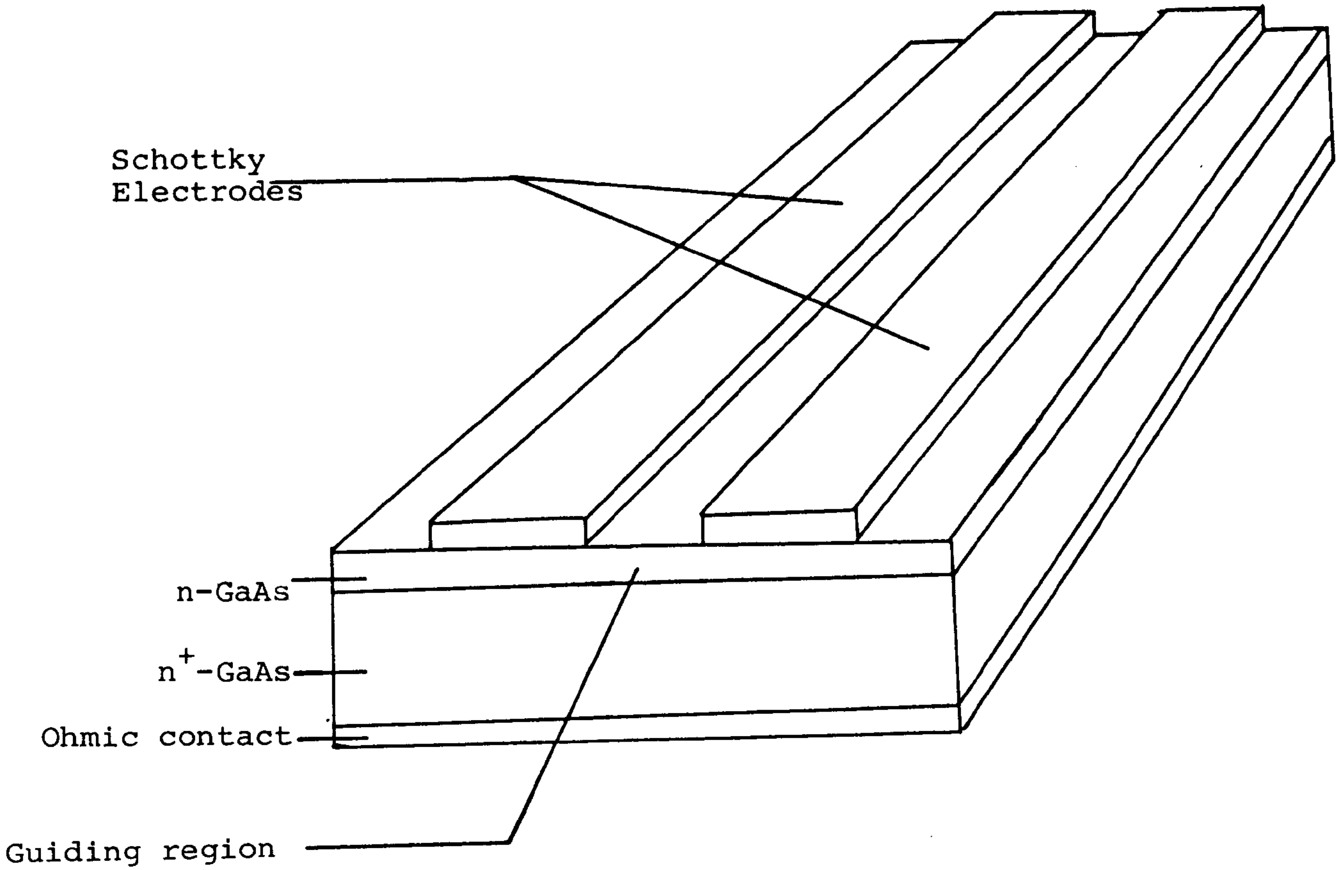

Fig.4.2 Schematic diagram of the photo-elastic optical channel waveguide.

Directional-coupler structures formed by the above multiple photolithography and etching process nearly always had one or more electrodes with poor Schottky barrier properties, in particular a soft breakdown on reverse biasing.

A photolithographic mask was therefore designed to enable the production of $\Delta\beta$ devices using a one-step photolithography and etching process. 75μm square bonding pads were provided enabling the total Schottky area to be substantially reduced.

4.1.3 Conventional channel-waveguide directional-coupler structures

These devices are fabricated by forming two single-mode waveguides in close proximity as in Fig.4.3(a) (typically edge separation is 3μm). Due to undercutting of the resist by the etchant a mask-and-etch technique is not suitable for device fabrication. Two other approaches were tried therefore :-

(i) The directional-coupler pattern was formed in photoresist on the semiconductor surface and gold, or aluminium, then evaporated over this to form the devices (Fig.4.3(b)).

In the earlier structures fabricated it was obvious that the resist thickness of about 1μm was limiting the effective thickness of the evaporated metal introducing strain into the GaAs. By spinning up to four successive layers of AZ 1350H photoresist thickness was increased whilst avoiding build-up at sample edges. After spinning, the device was left for 1 hour completed by an oven bake at 60^{o}C before processing. No significant degradation of line quality was observed.

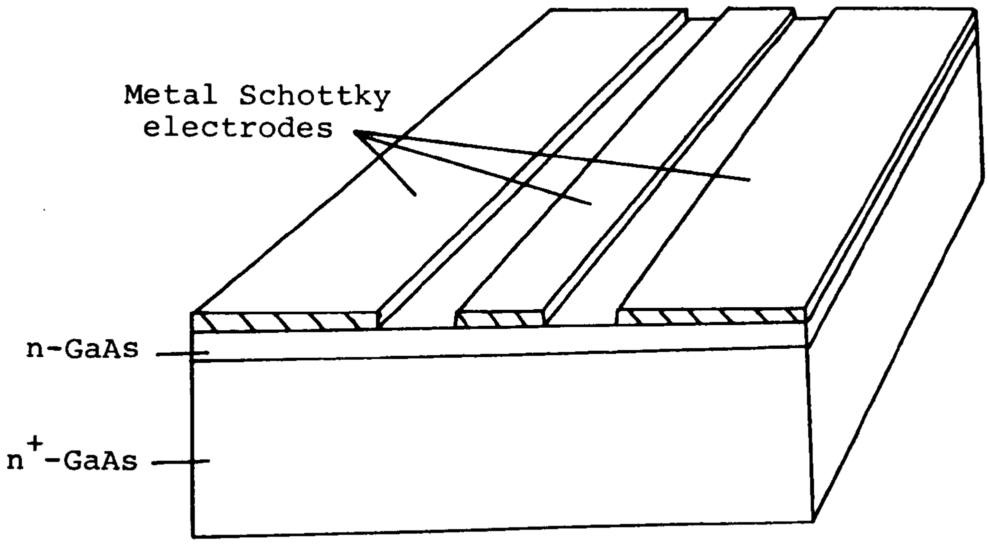

(a)

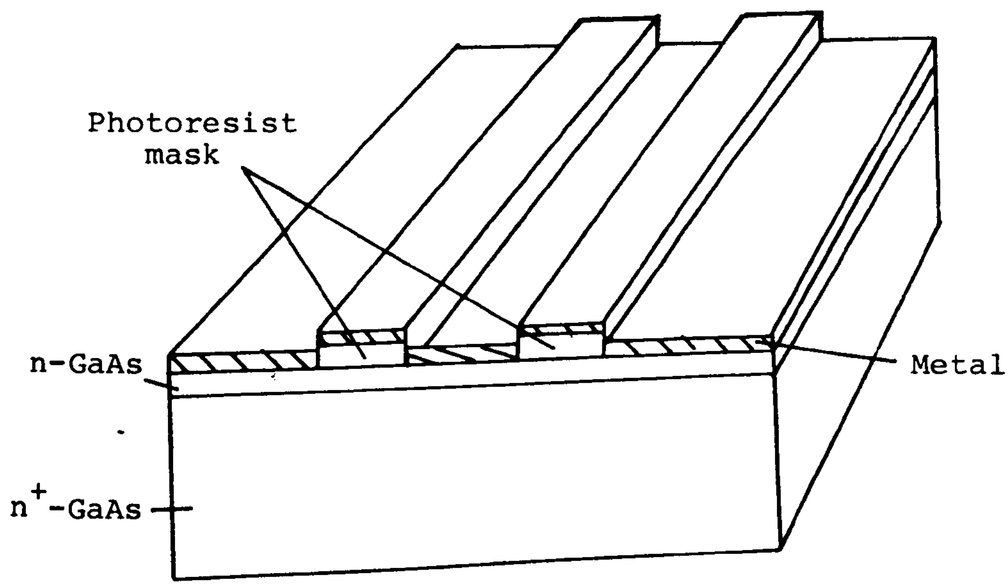

(b)

Fig.4.3 Directional-coupler structure formed by two single-mode channel waveguides in close proximity. (a) ideal structure and (b) practical structure.

The method is similar to that used by Campbell et al [14] who used an SiO_2 mask instead of the photoresist one.

(ii) After delineating the directional-coupler pattern as in (i) the photoresist was exposed to U.V. light for 1 minute and then loaded directly into the evaporator. Following evaporation the device was boiled in acetone to hopefully "lift-off" the photoresist and the fraction of the metal on top of it. It is required that the thickness of the resist is greater than that of the contact metal to ensure a discontinuity in the metal film at the edge of the resist thus allowing the solvent to reach the photoresist. Although this criterion was fulfilled, limited success was encountered. Some aluminium films could be "lifted-off" but not reproducibly. After heating the samples to $80^{o}C$ in the evaporator to introduce more strain (see section 3.1) the photoresist remained firmly attached to the sample even when subjected to ultrasonic agitation. It is thought that the large aspect ratio of the guides is at least partly to blame for the lack of success.

4.1.4 Bends through 90^{o}

Bent waveguides will be necessary to increase device packing density in integrated optics circuits. Photo-elastic waveguides have an advantage of identical guide cross-sections in the (011) and $(01\bar{1})$ crystallographic directions. Curved waveguide sections, however, prove inherently lossy.

Marcatili [63] derived a transcendental relation for the attenuation per radian ($\alpha_c R$) using an approach similar to that of his described in section 2.2.1. Numerical results based on the effective index method of Furuta [30] and curves presented by Marcatili show that the difference Δn in effective refractive index between the waveguide core and its surrounding regions has to be at least 0.01 for losses of less than 1dB/ radian at a radius of curvature compatible with integrated optics. Index changes due to doping differences in GaAs and strain effects are clearly not sufficiently large for curved waveguide sections exhibiting tolerable loss.

The reflection of light guided in a single-mode photo-elastic waveguide into a second perpendicular guide using a vertical etched facet running at 45° to the direction of propagation is proposed for providing bending with negligible loss. This device is illustrated in Fig.4.4.

4.1.4.1 Etching of the (100) surface in GaAs

Two different etchants were tried. The first was a citric acid : hydrogen peroxide : water system developed by Otsubo et al [64] for preferential etching of GaAs through photoresist masks. The composition of the etching solution was varied by changing the ratio k of 50 weight-per-cent citric acid to 30 weight-per-cent H_2O_2. A solution k = 10 was found to give good clean etching profiles. However, the etching rate of 25Å s^{-1} made it unsuitable for etching walls of depth 10μm necessary to ensure complete reflection of the guided light.

Iida and Ito [65]report selective etching of GaAs using the H_2SO_4 : H_2O_2 : H_2O system.For reaction-limited etching of the (100) face with a mask in the [010] or [001] direction

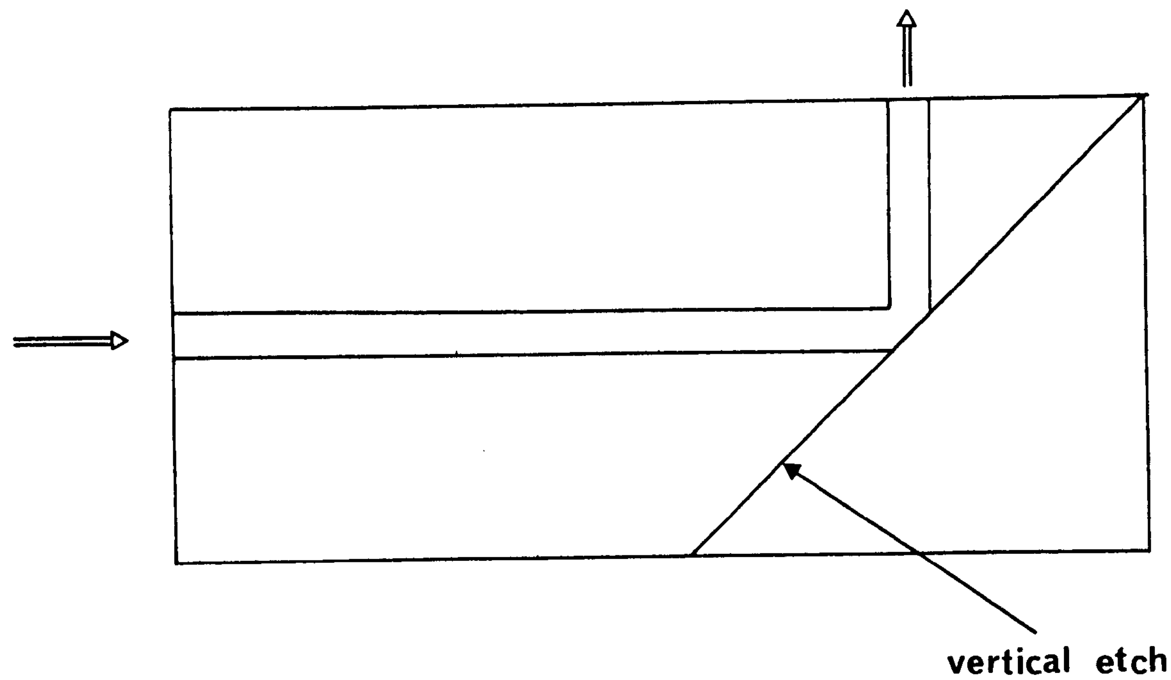

Fig.4.4 Proposed structure for providing bending through 90^{o} with negligible loss

they found the etched wall to be nearly perpendicular to the (100) surface. The walls exposed are the {100} planes.

When used at room temperature the etching solution attacked the photoresist mask in places producing a jagged edge. On cooling the etchant to 0-2^{o}C the AZ 1350H photoresist was resistant to attack by the etchant and clean etching profiles were obtained. Fig.4.5 shows the cross-sections obtained for edges orientated along various crystal directions using the 1 : 8 : 1 cooled etch. Etch depth measured for different samples under a microscope and using a "Talystep" displayed a linear increase with time showing the process to be reaction rate limited. The etch rate is about 3μm min^{-1}. No dependency on dopant density in the GaAs was noted.

The H_2SO_4 : H_2O_2 : H_2O etchant was freshly made up for each sample. Cooled etchant was produced by mixing 2.5ml H_2O and 2.5ml H_2SO_4 in a beaker surrounded by crushed ice which was placed in a refrigerator for about 1 hour. 20ml H_2O_2 were then added and the whole etch cooled in the refrigerator for a further 5 minutes. Samples were pre-etched in concentrated HCl for 5 minutes.

In studying etching profiles (and later in producing devices) particular attention was paid to cleaning prior to processing in order to give good photoresist adhesion and reproducibility of results. After cleaning in solvents (as section 4.1(b)) the slices were washed in de-ionised water, boiled in methanol and blown dry with a nitrogen gun. The samples were then stuck to cover slips, etched in concentrated

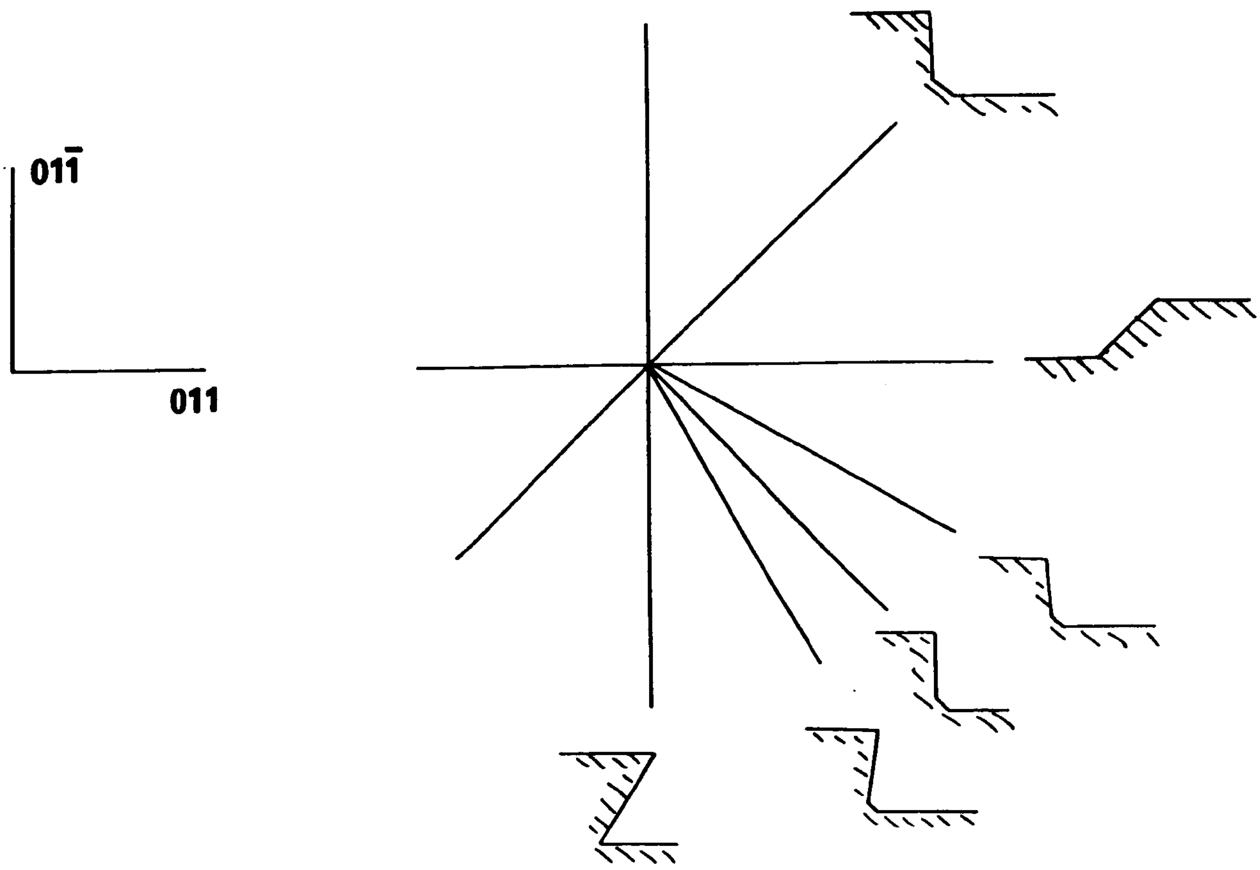

Fig.4.5 Sketches of etch profiles along various crystal directions on (100) GaAs substrate etched with 1 : 8 : 1 reaction-limited etch.

HCl for 5 minutes, rinsed in de-ionised water, boiled in iso-propyl alcohol and again blown dry with nitrogen. After drying under an I.R. lamp for 15 minutes and blowing cool with nitrogen AZ 1350H photoresist was spun onto the sample at 6500 r.p.m. The samples were processed as in section 4.1.1(iii), and following development of the photoresist, post-baked under the I.R. lamp for 15 minutes and then in an oven at 80-90^{o}C for another 15 minutes. This post-bake did not cause rounding in the vicinity of the delineated edge and the corresponding degradation of line quality found when post-baked in the oven for 20 minutes at 130^{o}C. The resulting edges were straight to better than 0.5μm.

4.1.4.2 Fabrication of waveguides

Photo-elastic waveguides were fabricated by evaporating 1-2μm of gold over 8μm wide stripes of AZ 1350H photoresist. The technique is as described in section 4.1.3(i).

4.2 InP Waveguides

The fabrication of devices using epitaxial InP layers is almost identical to that for corresponding devices in GaAs. The material used in fabricating the devices examined during the present studies had a lightly-doped InP epitaxial layer about 3μm thick grown on heavily-doped n^{+} InP substrates ($N_D \sim 10^{18}cm^{-3}$). During evaluation experiments L.P.E. layers were used. In the main two epitaxial slices were used, one grown by the halide process, the other by M.O.C.V.D. These layers had carrier concentrations of $|N_D-N_A| = 1 \times 10^{15}cm^{-3}$ and $|N_D-N_A| = 1 \times 10^{16}cm^{-3}$ respectively.

A slightly different cleaning process was adopted from that used for GaAs. After boiling in solvents the wafers were etched in $5H_2SO_4$: $1H_2O_2$: $1H_2O$ for 10 minutes at $50^{\circ}C$. This slow etch is often used to clean substrate surfaces before L.P.E. growth.

One important difference between InP and GaAs is that low leakage Schottky barriers to n-type InP are difficult to make because of a low metal-semiconductor barrier height. Incorporation of an interfacial oxide layer in the Schottky barrier structure and subsequent annealing of the oxidised surface can increase the barrier height by 0.3 - 0.4eV whilst still attaining a nearly ideal n-factor [66], [67]. Thus prior to evaporation the InP surface was oxidised in nitric acid for 10s at $70^{\circ}C$ under illumination from a 12W tungsten lamp. The thin oxide layer grown was subsequently alloyed in to the InP for 30 minutes under nitrogen at $250^{\circ}C$. Schottky barrier properties with and without the oxide layer present are discussed further in section 6.6.1.

The presence of the oxide layer was beneficial in also preventing a reaction between the gold film and the InP observed after etching of un-oxidised samples. The oxide layer is thought to make negligible difference to strain fields.

For InP a slightly larger total thickness of 130μm was found to be the best compromise for a sample both easy to cleave and handle.

4.3 Cleaving and Mounting Devices

4.3.1 Cleaving

The coupling of light into and out of the waveguide requires the device cross-section to be exposed. After fabrication therefore sample ends were cleaved using the technique described in section 4.1(e). With device thicknesses quoted, lengths greater than 300μm could reproducibly be cleaved off a sample 5mm long. The resulting cleaves were very clean and generally free from cracks except at the point where the tweezers contacted the semiconductor. In several channel structures with large gold thicknesses localised cracks developed under the channel itself on cleaving, possibly because of the large strains there. Where such cracks were observed devices were re-cleaved until a crack-free cleave was attained.

In devices where a totally gold-covered sample was to be cleaved gold films tended to peel off the sample on cleaving. If a further layer of negative photoresist was spun over the surface and baked for 1½ hours at 135^{o}C the photoresist became brittle and would subsequently break cleanly along a cleave. This caused the gold sandwiched between it and the sample to likewise break cleanly. The technique was found particularly helpful for cleaving of two perpendicular faces in the study of waveguiding through 90^{o}.

4.3.2 Mounting on headers

All devices were mounted on headers, about 1.5cm long and of width slightly smaller than the sample length, cut from printed-circuit board coated on one face with copper.

Passive structures were mounted using wax which was melted onto the end of the header and wiped to a thin layer using a filter paper. The sample was then placed on the surface with the waveguide direction perpendicular to the longest dimension of the header.

By cutting through the copper coating on the printed-circuit board, using a fine saw, headers for electrically active structures were provided with several electrically isolated regions. The devices were fixed at their substrates to a central metal pad with a conducting gold epoxy (trade name "Ablebond" which was then cured for 1 hour at $140^{o}C$.

Electrical connection to the Schottky barrier was effected by connecting a gold wire of 50μm diameter between the electrode and an isolated region of the header. To do this the header was placed on a heating stage and a pool of epoxy was put onto it. The gold wire was bent into a horizontal "S" shape and its free end dipped into the epoxy with the aid of a micropositioner. Sufficient epoxy was picked up to subsequently form a connection to the sample electrode. With careful positioning the body of the wire simultaneously dropped into the original pool of epoxy. The epoxy was then cured as above and the bonding process repeated until all connections were made. Fig.4.6 shows photographs of a bonded wide-slot $\Delta\beta$ directional-coupler.

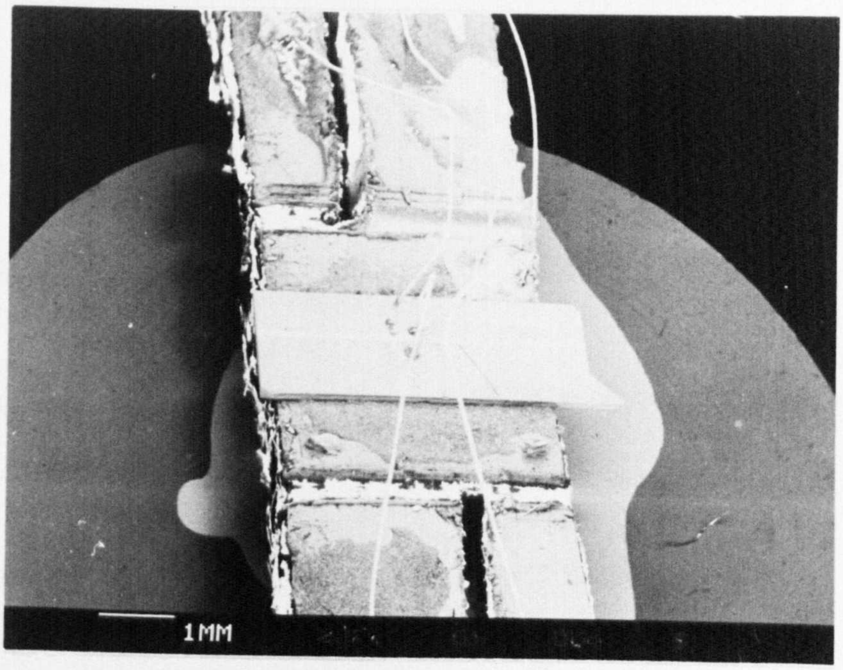

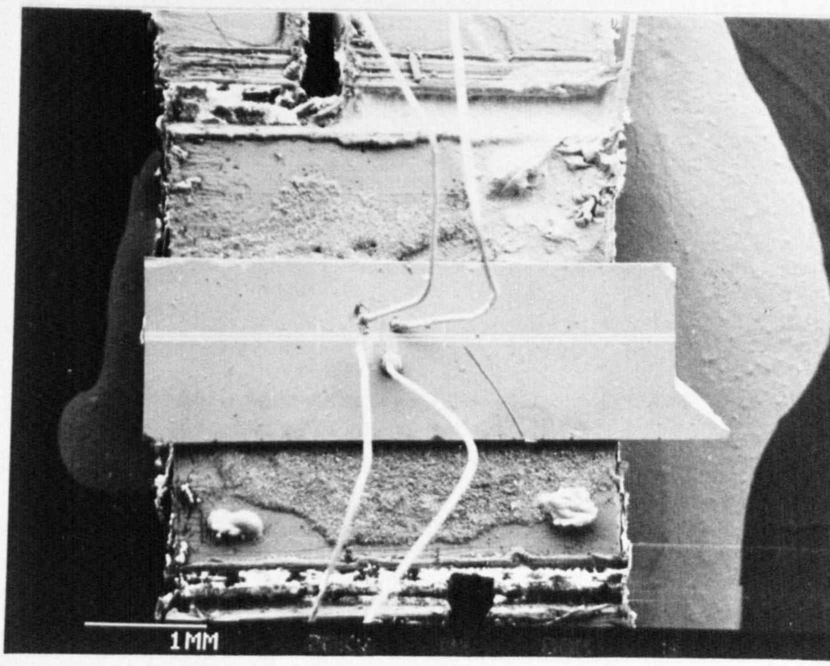

Fig.4.6 Photographs showing bonding of gold wire leads to wide-slot $\Delta\beta$ directional coupler and header configurations.

CHAPTER 5

THE OPTICAL EQUIPMENT

Most of the purpose-built optical system used in this work has been described in detail by Westbrook [24]. The important features and some of the modifications made will be outlined here.

5.1 The Optical Bench

The construction of the optical bench is illustrated in the block diagram of Fig.5.1.

The light source used was a linearly polarised 1mW He-Ne laser operating at a wavelength of 1.15μm and mounted at 45^{o} to the horizontal. An I.R. polariser at the laser output enabled TE or TM polarised modes or both to be excited in the devices. The sample headers were attached to a length of semi-rigid coaxial cable using "electrodag" (a highly conductive paint). Where required electrical connections were made to the cable also using "electrodag". A second length of coaxial cable was provided for applying a second independent bias to the electrodes of Δβ directional couplers. Microscope objective lenses were mounted in two three-dimensional micromanipulators positioned on either side of the device. The position of the input objective could be monitored to 1μm using a "Baty" gauge. The output face of the sample could be imaged in white light for alignment and to check the quality of the cleaved edge.

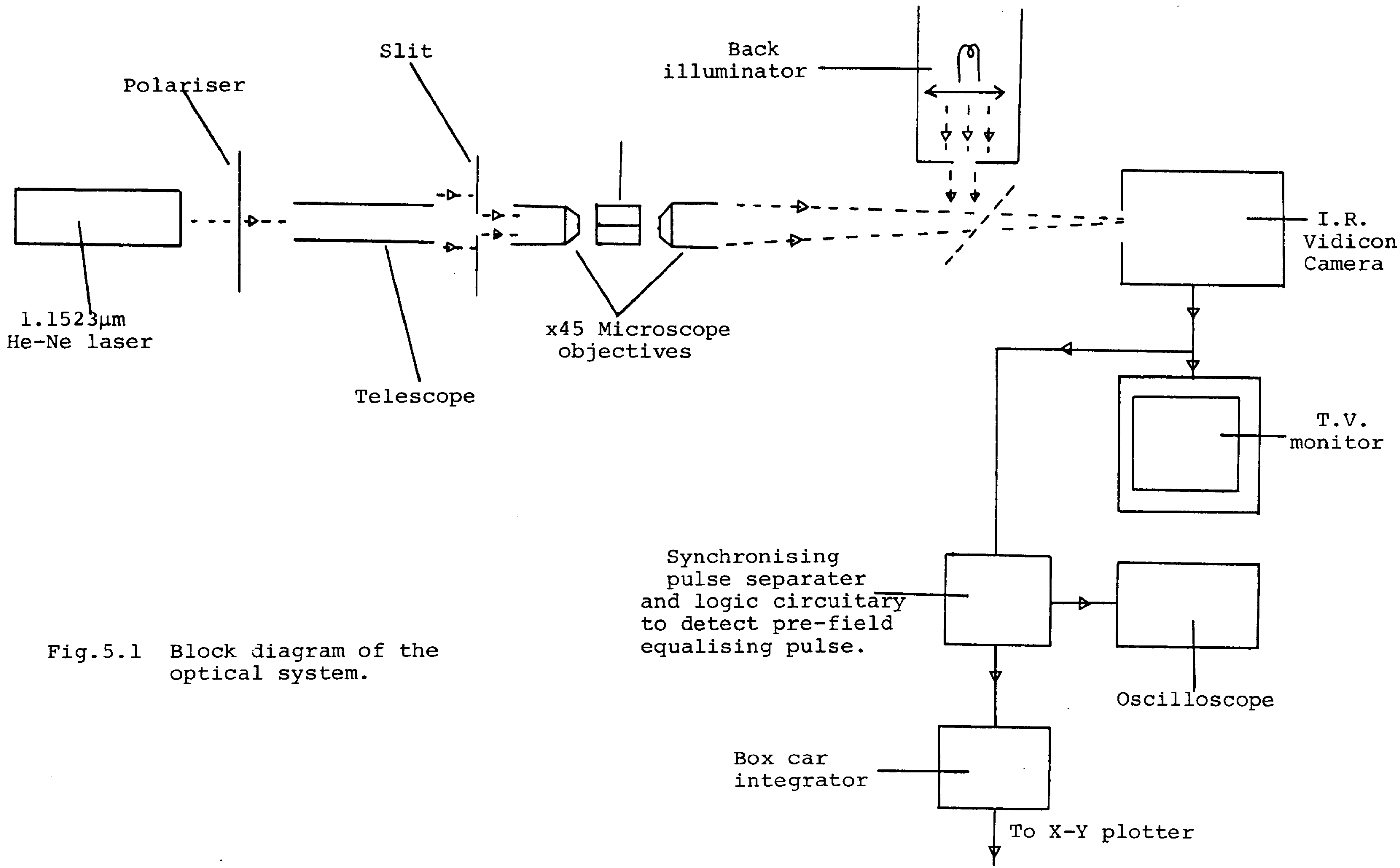

Fig.5.1 Block diagram of the optical system.

5.2 Waveguide Coupling

Light is coupled into and out of the waveguide by 'end-fire' coupling. To avoid exciting radiation modes the incident beam should match the profile of the guided mode to be excited and be carefully aligned with the sample. Westbrook shows that a 2.5μm diameter spot can be achieved by focussing a laser beam with a x45 microscope objective provided that a beam expander is positioned between this lens and the laser. With this arrangement all the light emerges from the epitaxial region. For many of the waveguides studied this spot was sufficient to excite only guided modes. In some "weak" guides, however, it was found helpful to tailor the beam to further match the elliptical shape of the guided modes. This was done by using a narrow adjustable slit to diffract the expanded beam. Unwanted slab modes could then be eliminated with careful alignment.

5.3 The Detection System

In the main a detection system based on a Siemens XQ1112 I.R. Vidicon tube installed in a LINK 109A camera was used. The camera was positioned at the focal point of the output lens and the Video-signal output displayed on a T.V. monitor.

Logic circuitry described by Westbrook [24] enabled the information contained in a selected T.V. line to be displayed on an oscilloscope. The circuitry counts line synchronising pulses down from a pre-set line number and on reaching zero applies a trigger pulse to the oscilloscope time base. If the video signal is connected to the Y input of the oscilloscope the intensity information of the selected T.V. line can be displayed. Sampling the T.V. line with a box-car integrator allows a record of the oscilloscope display to be made on an X-Y recorder.

The magnification of the output lens was $\sim$61 and the usable Vidicon target width 12.8mm. Each T.V. line scan lasts 52μs, consequently each microsecond of video signal corresponds to $(12.8 \times 10^{-3}/61 \times 52)$ m i.e. $\sim$4μm at the output waveguide cleave.

The light transfer characteristic or gamma of the Vidicon tube was determined using a set of neutral density filters. The transmittances of these at 1.15μm were found using a spectrophotometer. The camera saturated when the laser was focussed directly onto it with no sample present. The neutral density filters were used in series, and in conjunction with several single-mode waveguides, to gauge the gamma of the camera at lower light intensities. The electrical output signal was proportional to the input light intensity for camera voltage settings up to the maximum used in making measurements.

A Roffin Ge photodiode (model 7462) was also used for light intensity measurements. Using the neutral density filters output current was shown to vary linearly with optical intensity. Laser output intensity measured using the photodiode remained constant with time after an initial warm-up period of about 30 minutes.

CHAPTER 6

RESULTS AND DISCUSSION

6.1 The Finite-Difference Method and Its Comparison With Some Other Techniques

This section presents and discusses the results of a theoretical analysis of the rib waveguide structure shown in Fig.6.1(a). Comparison is made between solutions obtained using the effective index method, those given by the finite-difference method and the results of Austin [68] who used a variational method of solving the wave-equation developed at the University of Glasgow and summarised by Macfadyen [69].

Values of effective refractive index (N_{eff}), for the four TE modes supported by this structure as given by Austin are :

$$N_o = 3.406179$$
$$N_1 = 3.392070$$
$$N_2 = 3.369115$$
$$N_3 = 3.350042$$

The equivalent slab guide when solving using the effective index method is given in Fig.6.1(b) where $N_I = 3.357639$ and $N_{II} = 3.411645$. From the TM solutions for this structure the effective refractive indices for the rib guide are :

$$N_o = 3.407891$$
$$N_1 = 3.396829$$
$$N_2 = 3.379297$$
$$N_3 = 3.359158$$

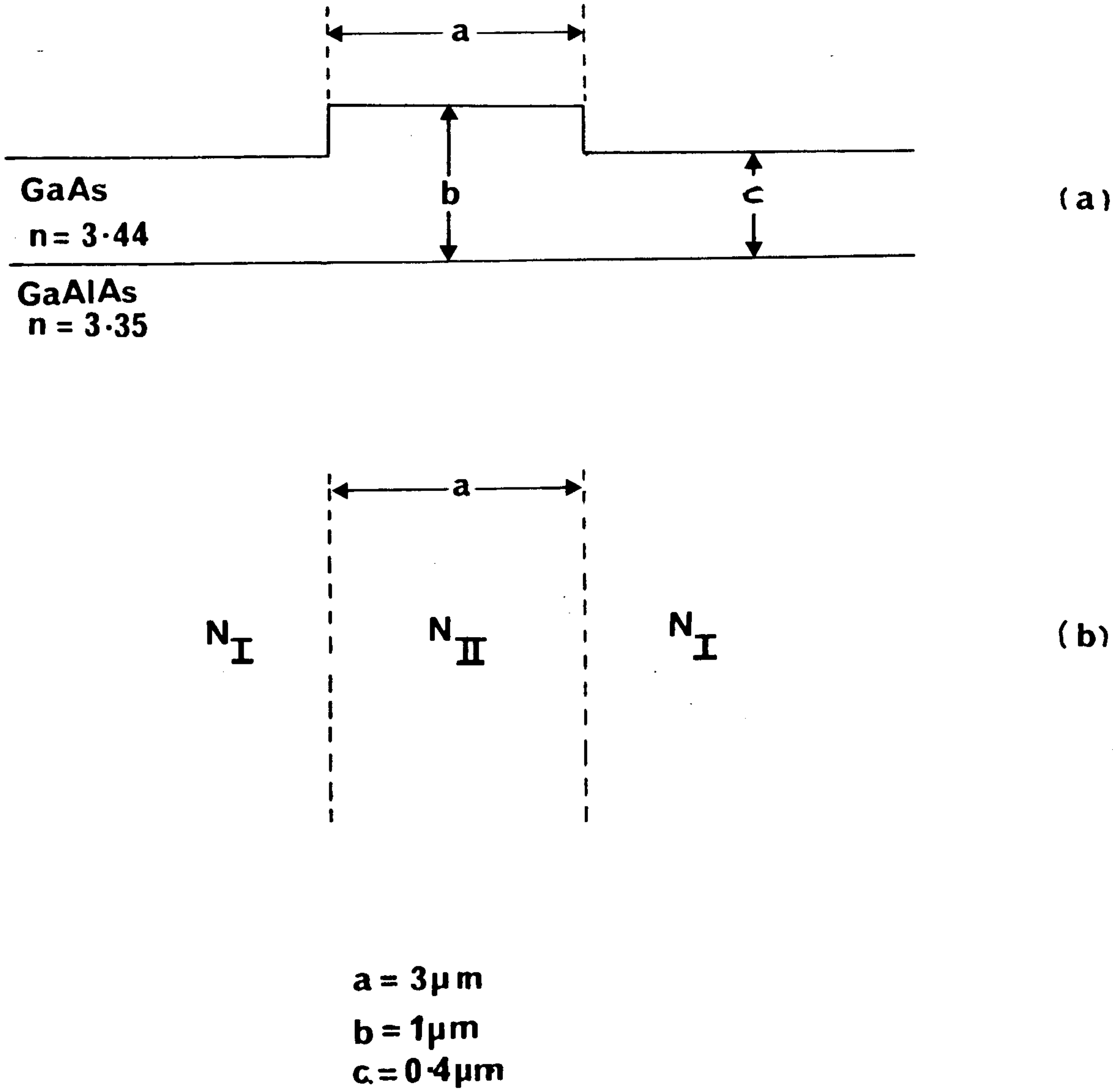

Fig.6.1 Rib waveguide structure examined theoretically.

For solution using the finite difference method the waveguide was considered to be contained in a "box" of half-width 3μm and depth 4μm. Increasing these dimensions did not alter the calculated values of effective refractive index. If refractive index values at mesh points falling on the boundary between two regions are taken as the numerical average of the values on either side of the boundary the following effective refractive indices are found :

$$\left.\begin{array}{l} N_o = 3.405947 \\ N_1 = 3.392044 \\ N_2 = 3.370022 \\ N_3 = 3.348966 \end{array}\right) \quad X = Y = 0.1\mu m$$

and

$$\left.\begin{array}{l} N_o = 3.406588 \\ N_1 = 3.392964 \\ N_2 = 3.371259 \\ N_3 = 3.350126 \end{array}\right) \quad X = Y = 0.05\mu m$$

Closer agreement with analytical results was found for slab waveguides using boundary refractive index values determined from a consideration of stored energy and the continuity of normal $\underset{\sim}{D}$ and tangential $\underset{\sim}{E}$ components at a dielectric boundary. This leads to boundary refractive indices of :

$$n = \sqrt{(n_1{}^2+n_2{}^2)/2} \qquad (6.1)$$

for a boundary in the y direction, and

$$n = \sqrt{2n_1{}^2n_2{}^2/(n_1{}^2+n_2{}^2)} \qquad (6.2)$$

for one in the x direction. The improvement in effective refractive index for a n/n^+ slab waveguide can be seen in section 6.2. Using boundary refractive indices from (6.1) and (6.2) the finite difference method gives :

$$\left.\begin{aligned} N_o &= 3.406202 \\ N_1 &= 3.392171 \\ N_2 &= 3.369999 \\ N_3 &= 3.349397 \end{aligned}\right) \quad X = Y = 0.1\mu m$$

and

$$\left.\begin{aligned} N_o &= 3.406777 \\ N_1 &= 3.393039 \\ N_2 &= 3.371299 \end{aligned}\right) \quad X = Y = 0.05\mu m$$

for the structure of Fig.6.1(a).

Thus the numerical calculations all agree to within 0.001 (<0.03%) for all modes. Effective refractive indices obtained using the effective index method are in all cases larger than those found using the finite-difference technique. For the rectangular waveguide of Fig.2.4 a simple argument can be used to show this is the case. The effective index method overestimates the guiding by including the "corner regions" twice giving transverse propagation constants which are too small and a value of N_{eff} which is too large. This reasoning also explains why the results get worse for higher-order modes and incidently close to cut-off [27].

If the product of field profiles in the x and y directions from the effective index method is taken as an initial guess to fields for use in the finite difference method the correct solution is quickly iterated. The value of N_{eff}

obtained from the Rayleigh Quotient after one iteration is too small because the guessed field profile is not the correct one, being discontinuous at the rib walls ($y = \pm 1.5\mu m$). However, because this value for N_{eff} is too small and the effective index method gives a value which is too large an immediate error interval is specified for the correct result.

6.2 Attenuation in Dielectric Waveguides

Fig.6.2 presents published data on the attenuation coefficient at a wavelength of 1.15μm as a function of n-type doping for InP [70] and GaAs [71], [72] and shows InP to give lower loss than similarly doped GaAs.

Fig.6.3 shows the calculated attenuation coefficient (α) for the fundamental TE mode in an epitaxial layer with $N_d = 10^{15} cm^{-3}$ on a more highly-doped substrate as a function of guide thickness for both InP and GaAs. The calculation of α from equation (2.10) was outlined in section 2.1.2. The loss decreases slightly as substrate carrier concentration is increased because the greater loss of the evanescent field in the substrate is off-set by the better light confinement due to a larger refractive index step. Attenuation increases rapidly as the waveguide thickness is reduced to the cut-off value as a result of optical fields extending further into the substrate where loss is greater. Calculations using metal claddings of gold and aluminium have also been considered. Complex refractive indices of (0.34 - j6.4) for gold and (1.5 - j12) for aluminium were extrapolated from published data [74] as values at 1.15μm have not been reported.

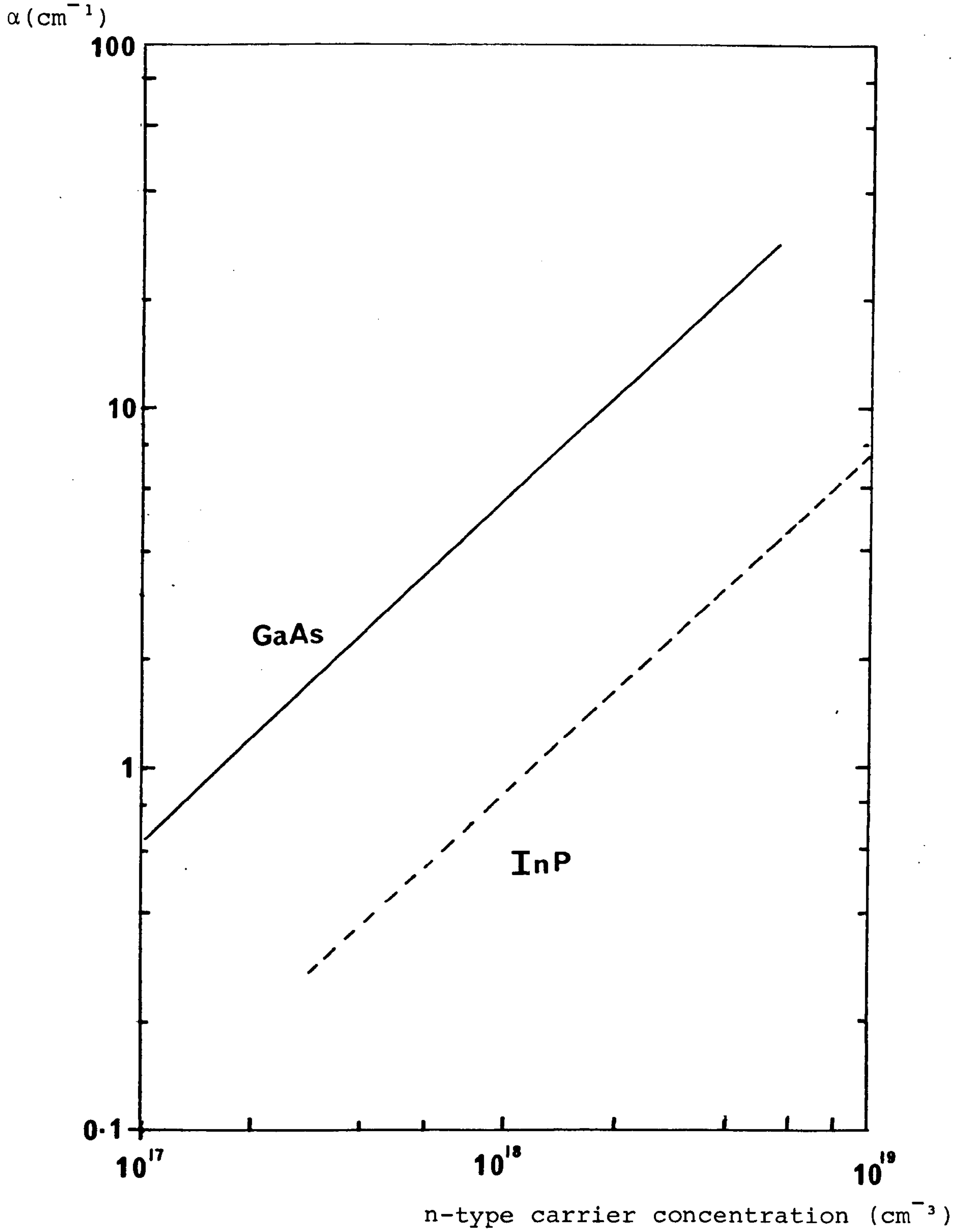

Fig.6.2 Attenuation coefficient at a wavelength of 1.15μm as a function of n-type doping.

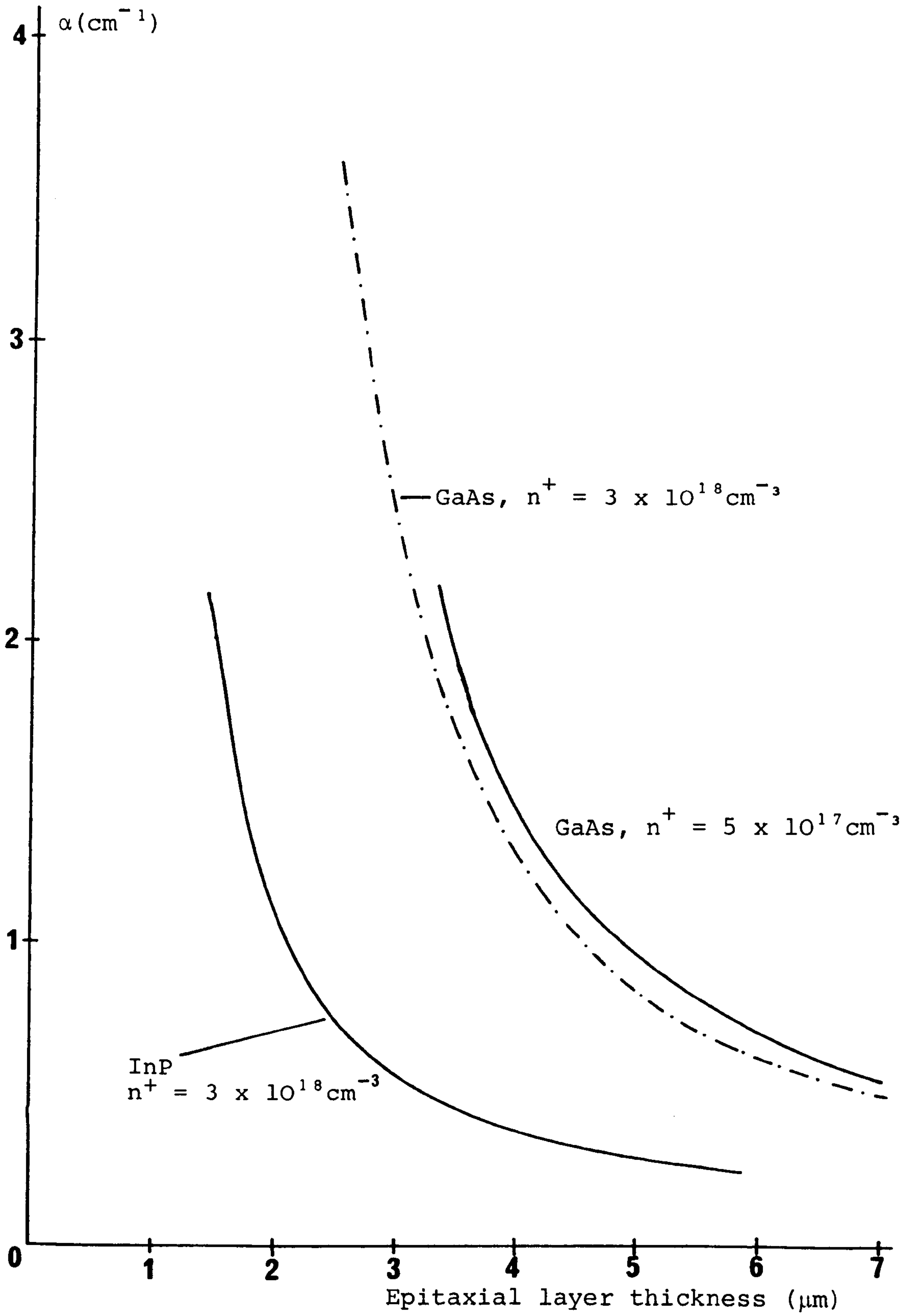

Fig.6.3 Variation of absorption coefficient with waveguide thickness for the fundamental TE modes in InP and GaAs n/n^+ slab waveguides. The full curve for the GaAs guide with $n^+ = 3 \times 10^{18} cm^{-3}$ is given in Fig.6.4.

The large imaginary part of the refractive index of metals reflects their high reflectivity. Fig.6.4 shows that for TE modes attenuation for a metal-clad n/n^+ waveguide is only slightly higher than that for the equivalent unclad case, a result of a small field in the vicinity of the metal.

For comparison purposes the variation of attenuation coefficient with waveguide width was found for the $GaAs/Ga_{0.77}Al_{0.23}As$ waveguide discussed in section 6.2. The losses for this waveguide, presented in Fig.6.5 are due entirely to the metal cladding with gold affording a reduction in loss when compared to aluminium. The different behaviour of the two slab waveguides is again governed by the refractive index step at the guiding layer/substrate interface.

It is also possible to estimate loss in waveguides from the field profiles calculated using the finite difference method. As outlined in Appendix 9.7 the power attenuation coefficient for the guide is given by :

$$\alpha = \frac{2k_o \iint nkE^2\,dA}{\iint nE^2\,dA} \tag{6.3}$$

The integrals can easily be evaluated in finite difference form using the trapezoidal rule outlined in section 2.3. Fig.6.6 shows a plot of α against epitaxial layer thickness for an 8µm wide slot waveguide fabricated on n/n^+ GaAs ($n = 10^{15}$ and $10^{16}\,cm^{-3}$, $n^+ \sim 1.2 \times 10^{18}\,cm^{-3}$). Values are slightly smaller than those for comparable slab waveguides (Fig.6.3). This is thought to be because the strain-induced

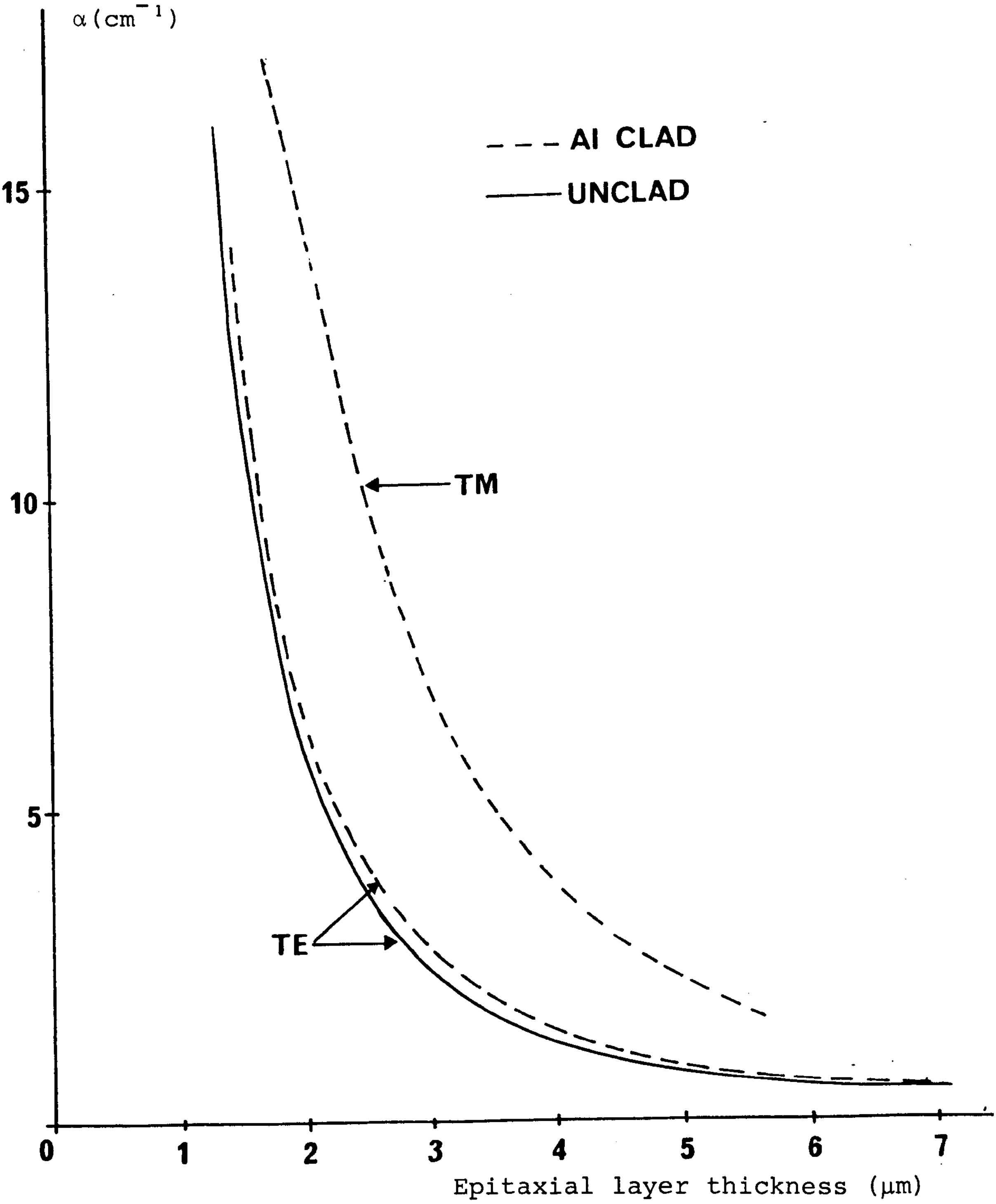

Fig.6.4 Variation of attenuation coefficient with waveguide thickness for TE and TM modes in unclad and aluminium-clad GaAs n/n^+ waveguides. In unclad guides α for TM modes is slightly higher than for equivalent TE modes, the curve is omitted for clarity.

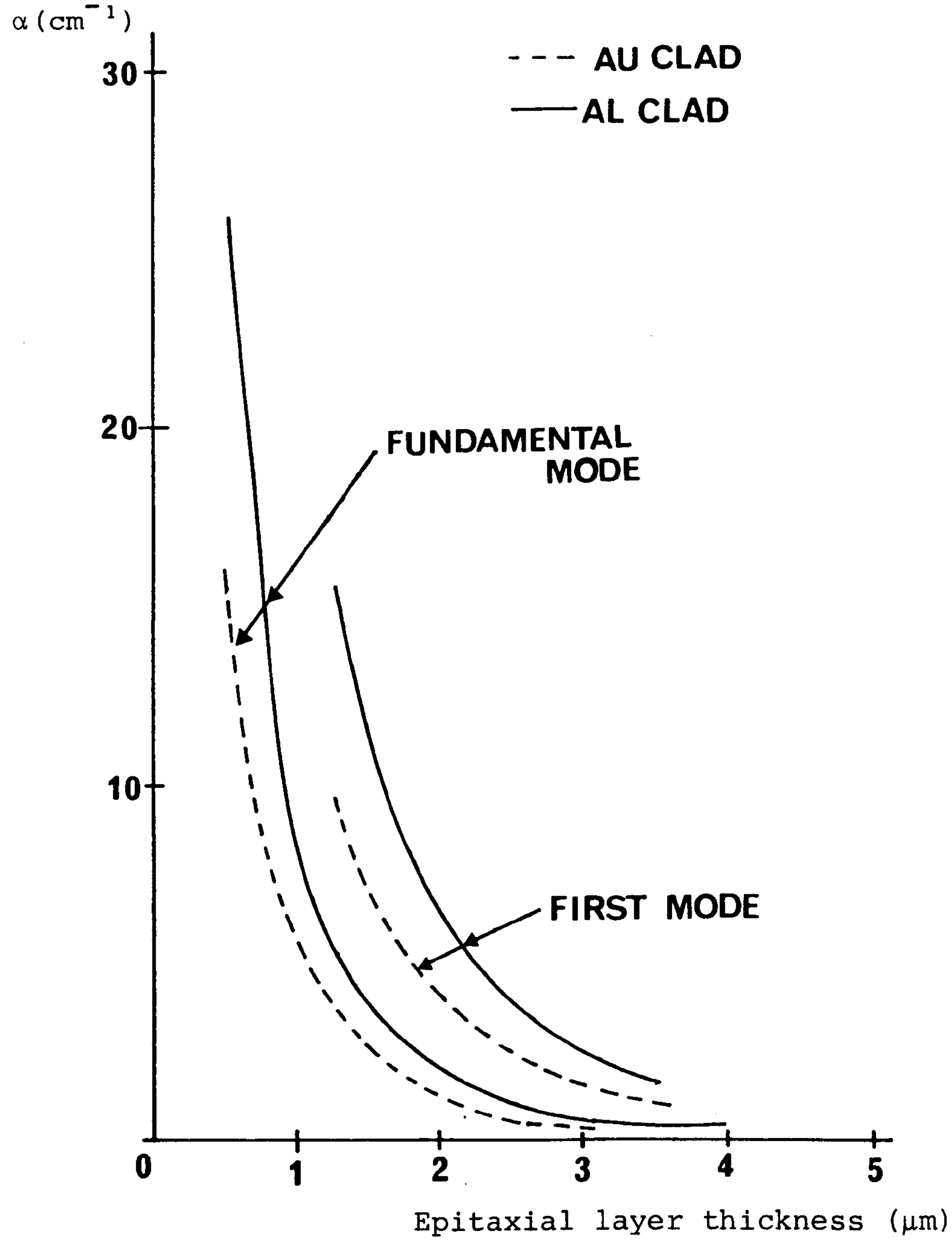

Fig.6.5(a) Absorption coefficient variation with waveguide thickness for TE modes in a GaAs/GaAlAs waveguide with gold and aluminium cover layers.

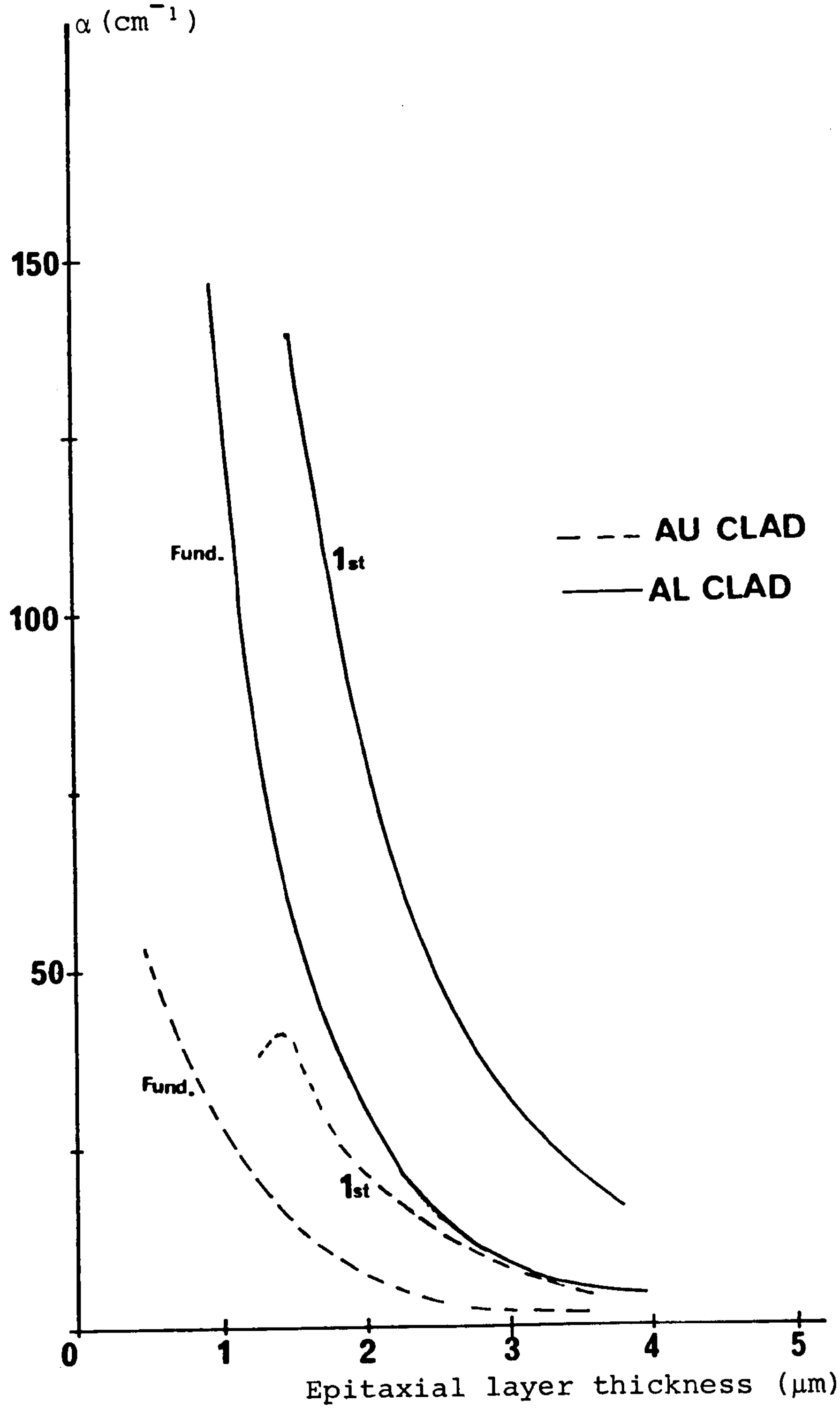

Fig.6.5(b) Absorption coefficient variation with waveguide thickness for TM modes in a GaAs/GaAlAs waveguide with gold and aluminium cover layers.

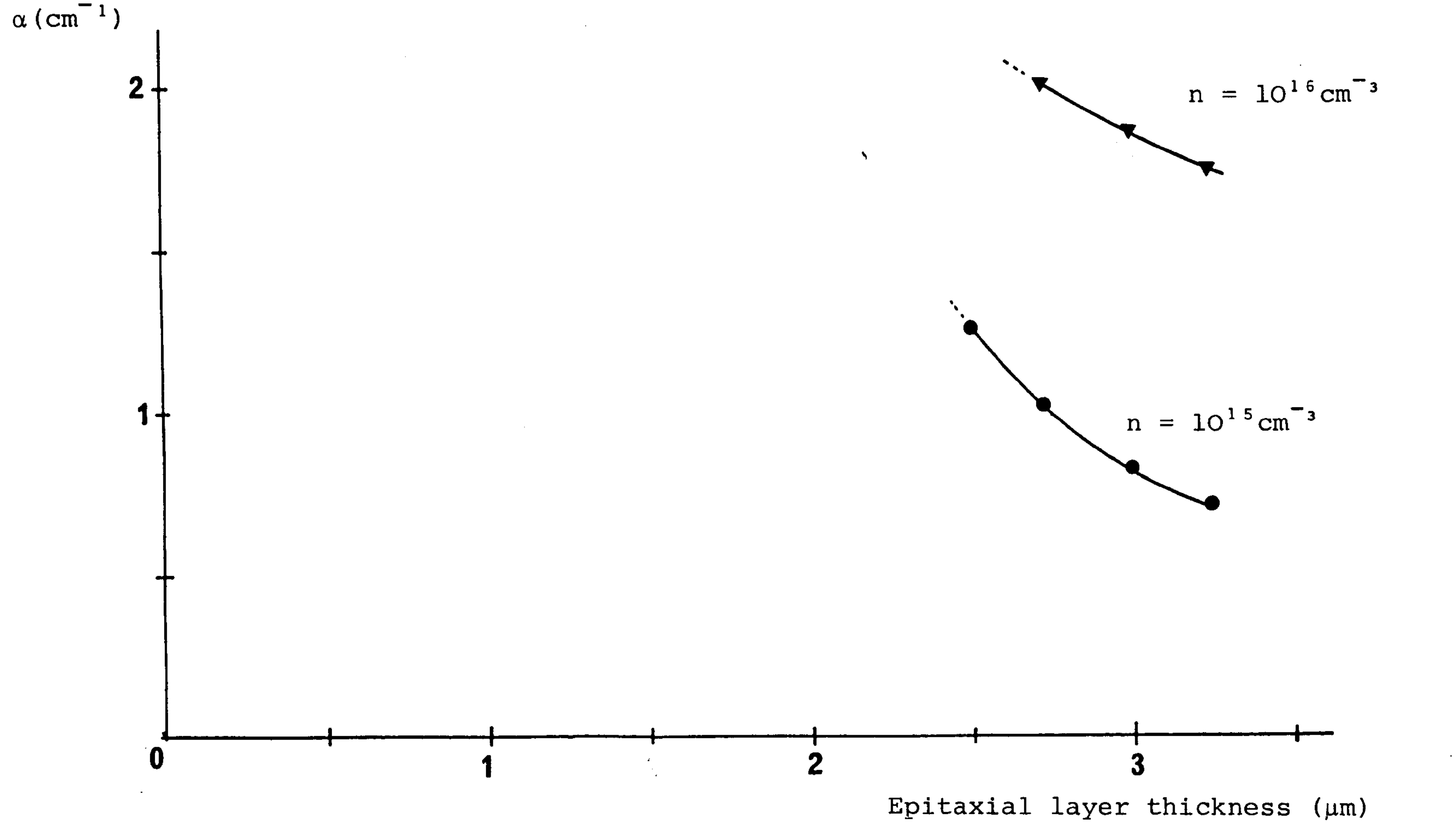

Fig.6.6 Attenuation coefficient as a function of epitaxial layer thickness for an 8μm wide slot-waveguide, $n^{+} \sim 1.2 \times 10^{18} cm^{-3}$.

refractive index changes decrease into the crystal so causing the fields to be guided more within the layer itself where losses are lower. If this were so it would be expected that losses due to the metal cover would become more significant, as for GaAs/$Ga_{1-x}Al_xAs$ guides, and that by ignoring these the finite-difference method underestimates attenuation. It is thought a reasonable approximation to ignore losses due to the metal as most of the guided wave is confined under the channel itself.

6.3 Guiding Mechanisms In Metal Clad Waveguides

Westbrook [24] pointed out that lateral waveguiding he observed in epitaxial GaAs layers grown on n^+ GaAs substrates was not due to electro-optic effects [73] which, as will become evident in section 6.5.1, would give different guiding properties in the (011) and $(01\bar{1})$ crystallographic directions and no guiding for TM polarised waves. Using effective index methods Westbrook also showed that interdiffusion at the metal-semiconductor interface [53] and small variations in epitaxial thickness (caused for example by overetching with the KI/I_2 gold etch) would lead to negligible waveguiding.

The proposed slot waveguide structures show similarities in design to the "metal-gap" waveguides of other workers [14], [20] who proposed that lateral confinement is solely due to a lower effective refractive index away from the slot arising from the presence of the metal cladding alone. For a 2.5μm thick GaAs epitaxial layer (n_2 = 3.44) on an n^+ GaAs substrate

(n_3 = 3.4375) effective indices calculated using (2.10), (2.24) and the computer program of Appendix 9.2 are 3.437616 for an air covering and 3.437600 for a gold covering. The effective index difference (1.6×10^{-5}) is not large enough to cause the relatively strong lateral waveguiding observed.

Hamasaki and Nosu [34] reported an effective refractive index difference of 4×10^{-4} for a "metal-gap" glass waveguide with a 2μm thick guiding region of refractive index $n_2 = 1.57$ and a substrate of refractive index $n_3 = 1.47$. The larger effective index step in this case is due to the greater refractive index step at the n_2/n_3 interface which provides greater confinement of the light within the guide and hence in the vicinity of the metal. This was further studied by calculating effective refractive indices for a GaAs waveguide with a $Ga_{0.77}Al_{0.23}As$ confining layer which has a refractive index of 3.35 [60]. This guide supports one TE slab mode for GaAs thicknesses in the range 0.32 - 1.05μm. For a layer thickness of 0.5μm the effective index difference between unclad and aluminium or gold clad regions is 5.7×10^{-3} and for a thickness of 1μm 1.8×10^{-3}. The effect on optical loss of the refractive index step between guiding layer and substrate is discussed in section 6.1.2.

Thus, when discussing waveguides formed using different impurity concentrations the effect of the metal on effective refractive index may be ignored. However, when larger refractive indices caused by material differences are used this is no longer the case. When using the finite-difference method of section 2.3 to model the experimental structures, therefore, only strain-induced refractive index changes and those forming the original slab waveguide need be considered.

6.4 The Finite-Difference Method for Strain Waveguides

6.4.1 Slab waveguides

In the development of the finite-difference method in section 2.3 fields at the air/GaAs interface were equated to zero (equation (2.31)). The approximation can be made because the dielectric slab waveguide is strongly asymmetric i.e.

$$n_2{}^2-n_1{}^2 >> n_2{}^2-n_3{}^2$$

and the normalised electric field strength at the n_1/n_2 interface is practically zero. The assumption is tested here by considering slab waveguides with the short-circuit condition modelled analytically by allowing $n_1 \to 0$.

Table 6.1 shows optical loss and N_{eff} values calculated from (2.24) and using finite difference methods for an n/n^+ GaAs slab waveguide ($n^+ \sim 1.2 \times 10^{18}$). The boundary condition of (6.1) gives a value of N_{eff} closer to the analytical one than using the arithmetic mean of the refractive indices to either side.

6.4.2 Convergence of the finite-difference method

The number of iterations required for the finite-difference calculations to converge to the required solution depends on the number of mesh points and the accuracy of the initial guess to the eigenvector. More iterations are required for convergence when using a larger number of mesh points as well as each individual iteration requiring more computer time. Table 6.2 presents values for the effective indices N_S and N_A of the symmetric and asymmetric modes calculated using the finite-difference technique for a 14μm wide strain-induced waveguide with $F = 1200\text{Nm}^{-1}$ and different mesh sizes. The refractive index variation with y at various depths was given for this structure in Fig. 3.5 . The approximate number of iterations required for convergence to six decimal places without the use of S.O.R. is also given in Table 6.2. Although both N_S and N_A vary by $\sim 2 \times 10^{-4}$ on halving the X mesh size the coupling length L_c calculated using (9.55) changes only by ∿0.1mm between X = 0.25μm and X = 0.125μm.

In practice the use of S.O.R. reduces the number of iterations required for convergence by a factor of about three. This is illustrated in Fig.6.7 which shows calculated effective index against number of iterations for the 14μm slot structure described above for the case X = Y = 0.25μm. It can be seen from Fig.6.7 and Table 6.2 that the value of the effective index increases as the field approximation improves, either by having more mesh points or by continued iteration. This is as predicted in Appendix 9.5.

6.5 GaAs Waveguides

6.5.1 Guiding at a remote metal edge

Fig.6.8 shows the positional change ε_r calculated from equation (3.26) for TE waves 1.5μm below a remote discontinuity such as that illustrated in Fig.3.3. 1.5μm is the approximate depth at which field strength of modes

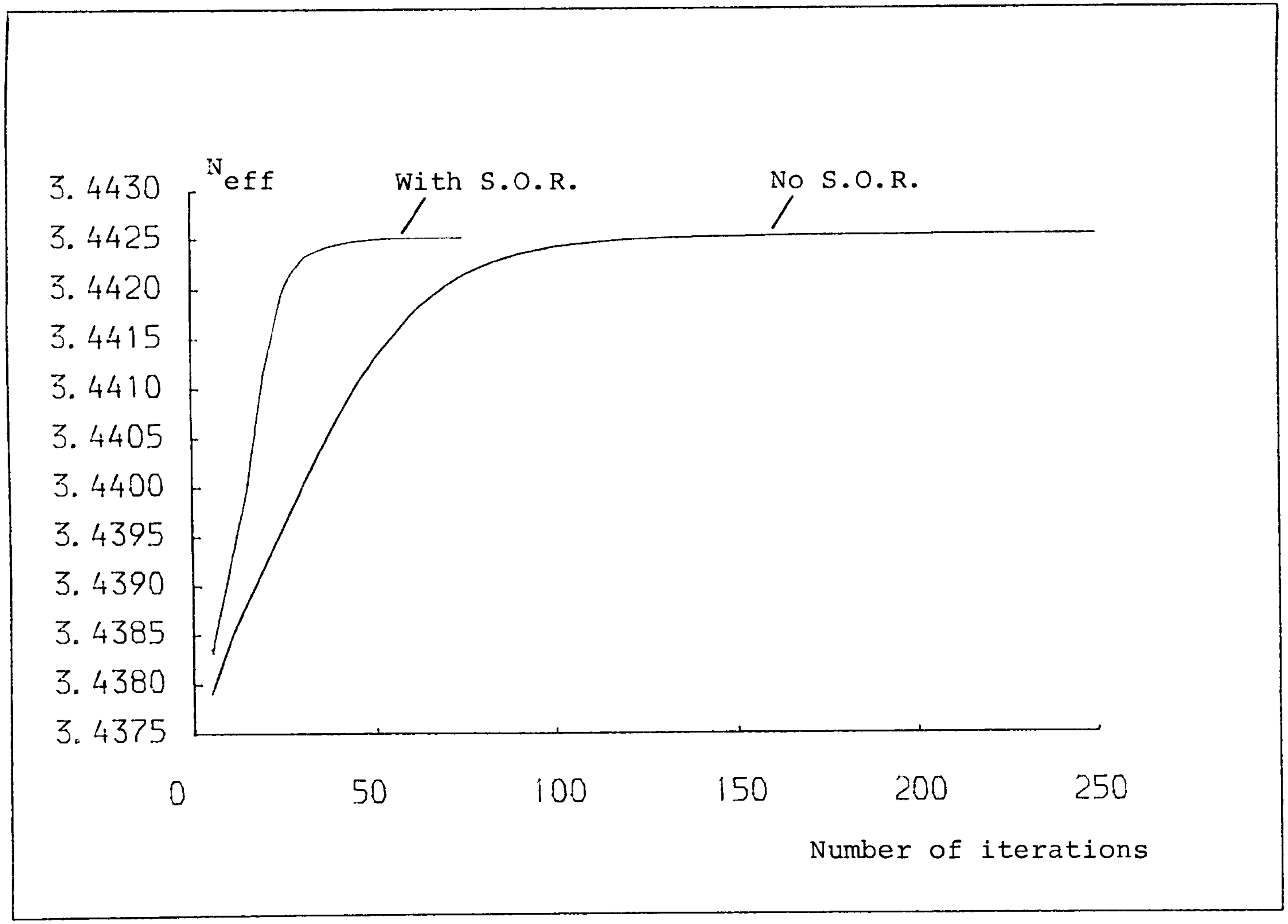

Fig.6.7 Effective refractive index as a function of iteration number for the finite difference solution of the waveguiding properties of a 14μm slot.

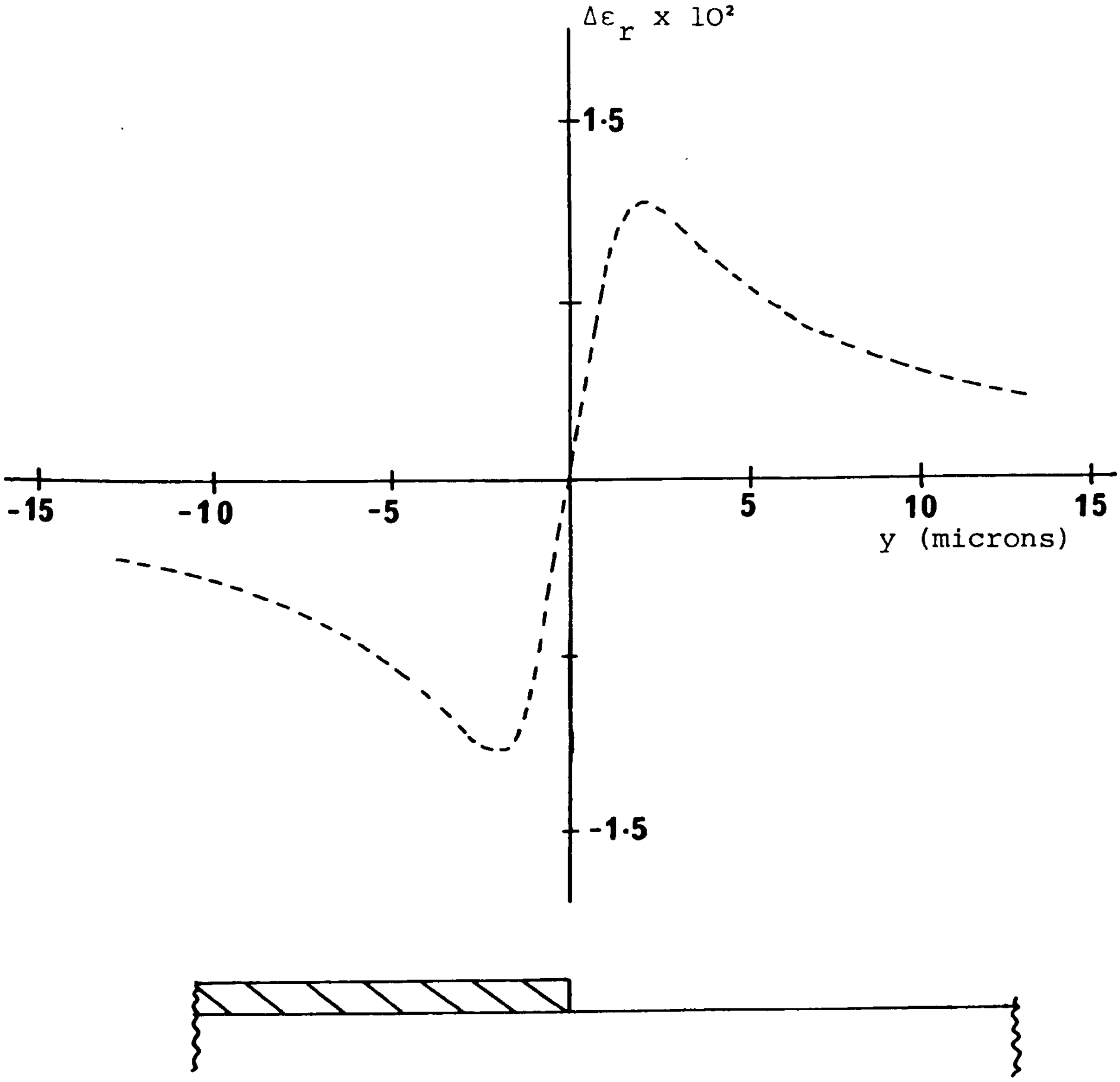

Fig.6.8 Positional change in ε_r for TE polarised waves at a depth of 1.5μm produced by a remote discontinuity ($F = 360Nm^{-1}$)

confined in the epitaxial layer is a maximum. In this example $F = 360Nm^{-1}$.

The waveguiding properties of the refractive index changes produced by such a remote discontinuity were examined using a 100μm wide, 0.6μm thick+, gold stripe. Single-mode waveguiding was observed at each discontinuity for both TE and TM polarisations. Fig.6.9 shows the TE polarised mode observed experimentally together with the intensity profile predicted by the finite-difference method.

The application of a reverse electrical bias to the deposited metal Schottky electrode depletes the epitaxial layer which quickly becomes punched-through. A large electric field then fills the region under the Schottky diode and fringing fields extend to the light-guiding region. The electric field $\underset{\sim}{E}_b$ is a solution of Poisson's equation :

$$\nabla . \underset{\sim}{E}_b = \frac{\rho_d}{\varepsilon} \qquad (6.4)$$

where ρ_d is the charge density.

For reverse bias voltages V_b greater than the punch-through voltage the electric field is given to a good approximation by :

$$E_b(x) = \left|\frac{V_b}{h}\right| \quad , \quad 0 > x > -h \qquad (6.5)$$

+All gold thicknesses quoted subsequently in this thesis are nominal values calculated from (4.1) to be consistent with Westbrook [24] and papers published on the present work. As mentioned in section 4 film thicknesses estimated from (4.1) are ∿1.5 times smaller than measured values. Measured film thicknesses are used to calculate quoted figures for F.

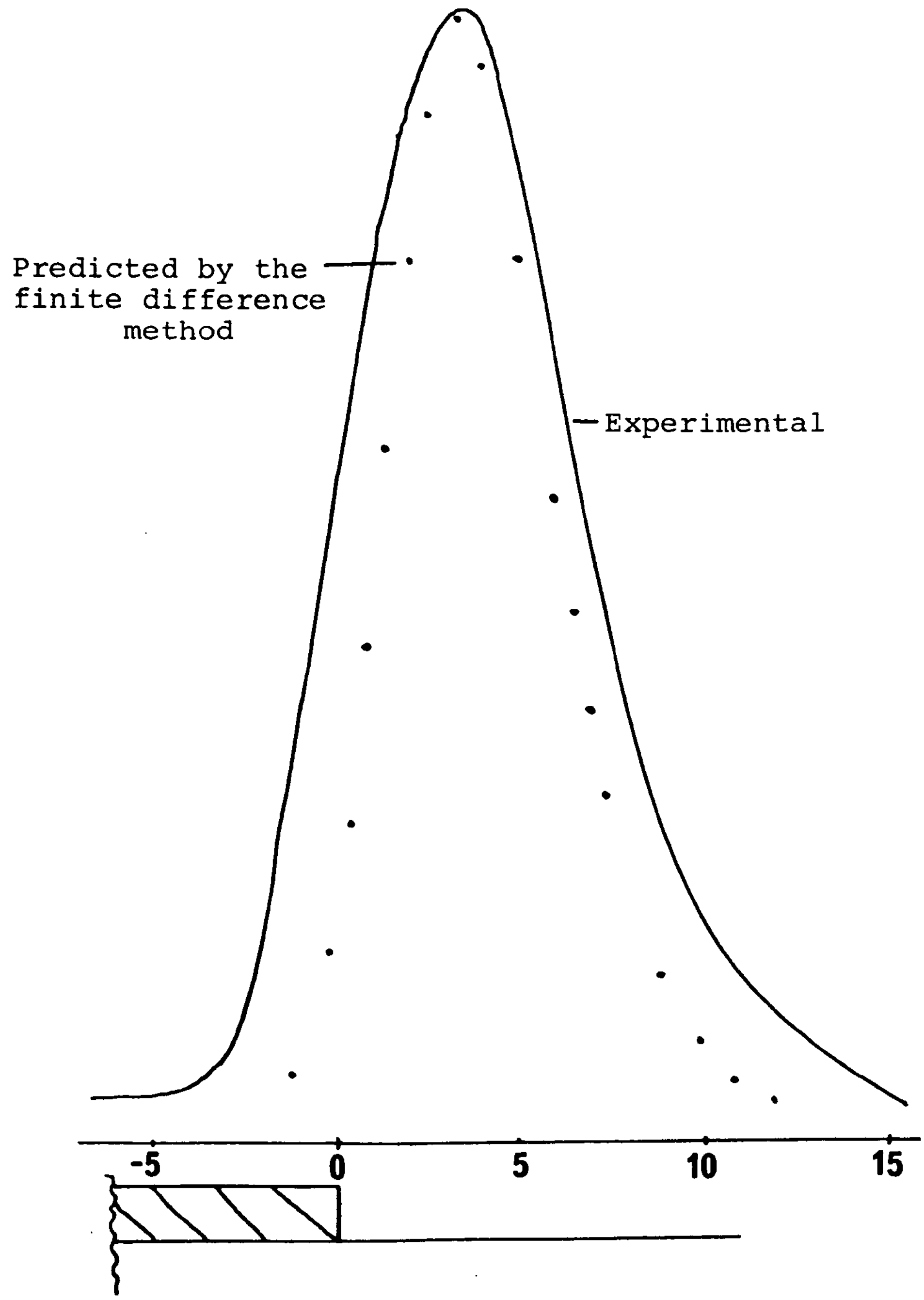

Fig.6.9 TE polarised mode profile found at the remote discontinuity of Fig.6.8 and profile predicted by the finite-difference method.

For TE waves the refractive index change produced through the electro-optic effect by an electric field in the (100) direction is [24] :

$$\left.\begin{array}{ll} \dfrac{+n_0{}^3 r_{41} E}{2} & \text{for } 01\bar{1} \text{ propagation} \\ \text{and} & \\ \dfrac{-n_0{}^3 r_{41} E}{2} & \text{for } 011 \text{ propagation} \end{array}\right) \qquad (6.6)$$

where r_{41} is the non-zero electro-optic coefficient in the reduced notation of Nye [56]. For GaAs $r_{41} = 1.4 \times 10^{-12} mV^{-1}$ [25]. These is no electro-optic interaction with TM-like modes [24].

As both TE and TM modes are guided by the strain-induced refractive index changes the electro-optic interaction with the TE waves may be measured. Equal amplitudes of each mode were excited and the output focussed onto the Vidicon camera. A crossed analyser was positioned between the sample and camera and reverse bias applied to the Schottky barrier. Fig.6.10 gives the resulting plot of intensity (normalised to its maximum value) as a function of reverse bias for an edge guide in a sample 4mm long. Total intensity was measured by summing values taken from the oscilloscope for each T.V. line on which the guided light showed. Relative intensity measurements taken in this way gave agreement within ±5% with those taken using the Ge photodiode.

If the field distributions of the TE and TM guided modes are assumed the same the intensity varies as :

$$I = I_o \sin^2 \left(\frac{\Delta\beta L}{2}\right) \qquad (6.7)$$

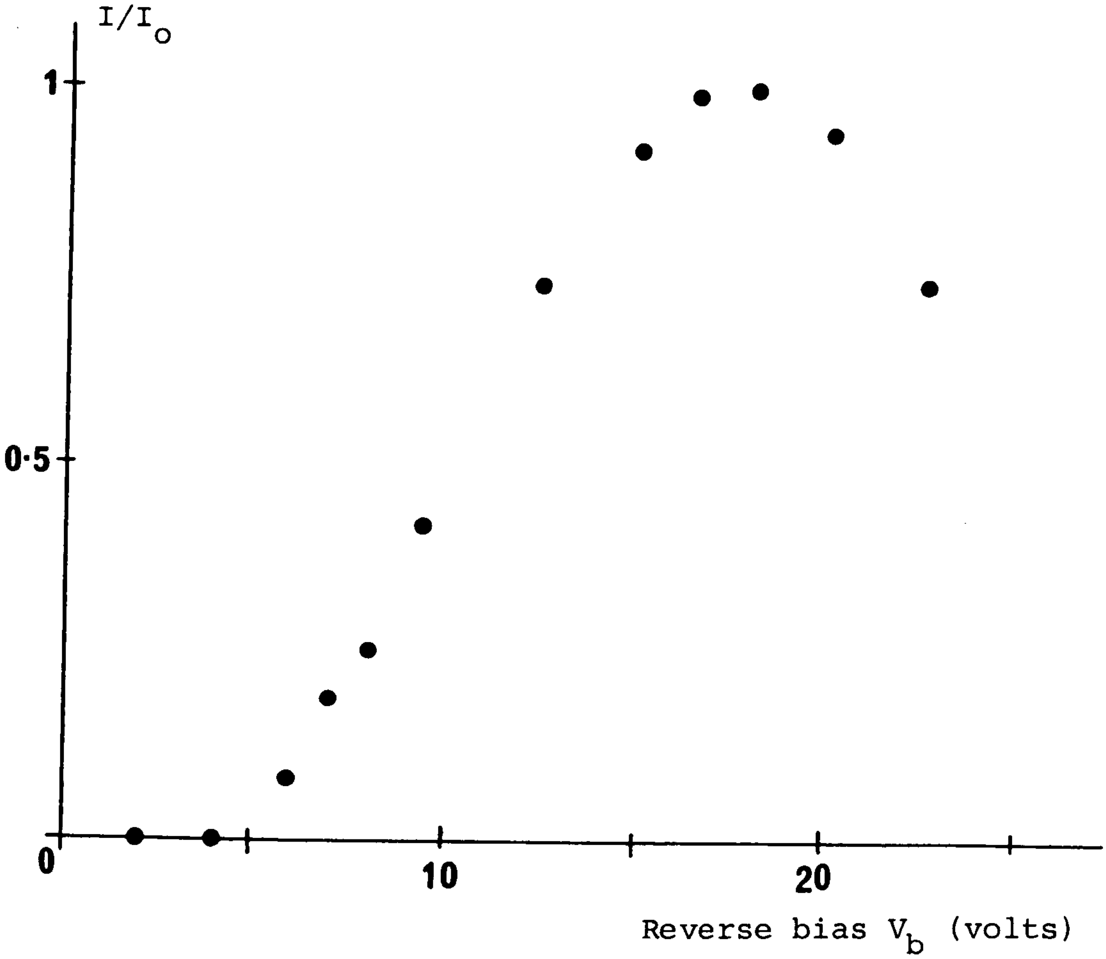

Fig.6.10 The variation in the total near field intensity (TE and TM), caused by the interference of two edge modes, as a function of bias voltage.

where

$$\Delta\beta = |(\beta_{TE}-\beta_{TM})| = \frac{\pi n_0{}^3 r_{41} E}{\lambda_0} \qquad (6.8)$$

and L is the sample length.

Using (6.7) to model the intensity distribution of Fig.6.10 gives $\Delta\beta L$ as a function of V_b as presented in Fig.6.11. The graph obtained is linear above $\approx$7V. The intercept voltage V_b = 3.4V agrees with a calculated punch-through voltage of 3.9V for a 2.7μm epitaxial layer with a carrier concentration $N_d \sim 7 \times 10^{14} cm^{-3}$. The stripe direction was determined to be in the $(01\bar{1})$ crystallographic direction from etch characteristics (see section 4.1.4.1). Corresponding results were found for edge guides running in the (011) direction.

6.5.2 Stripe waveguides

The device structure is illustrated in Fig.4.1 and was studied in detail by Westbrook [24] who used stripe widths between 17 and 29μm and gold thicknesses in the range 0.6 to 1.8μm.

All devices exhibited transverse waveguiding for both TE and TM polarisations, most with stripe widths between about 17 and 30μm in three separate regions of the cross-section, others at the stripe edges only. Measurements were made on two devices of Westbrook's (A6XA and A18YA) over a period of 30 months. Fig.6.12 compares the guiding properties of A18YA measured in November 1981 and by Westbrook in 1978. It is clear that they have changed little. A summary of the measurements made on this and other devices is given in Table 6.3.

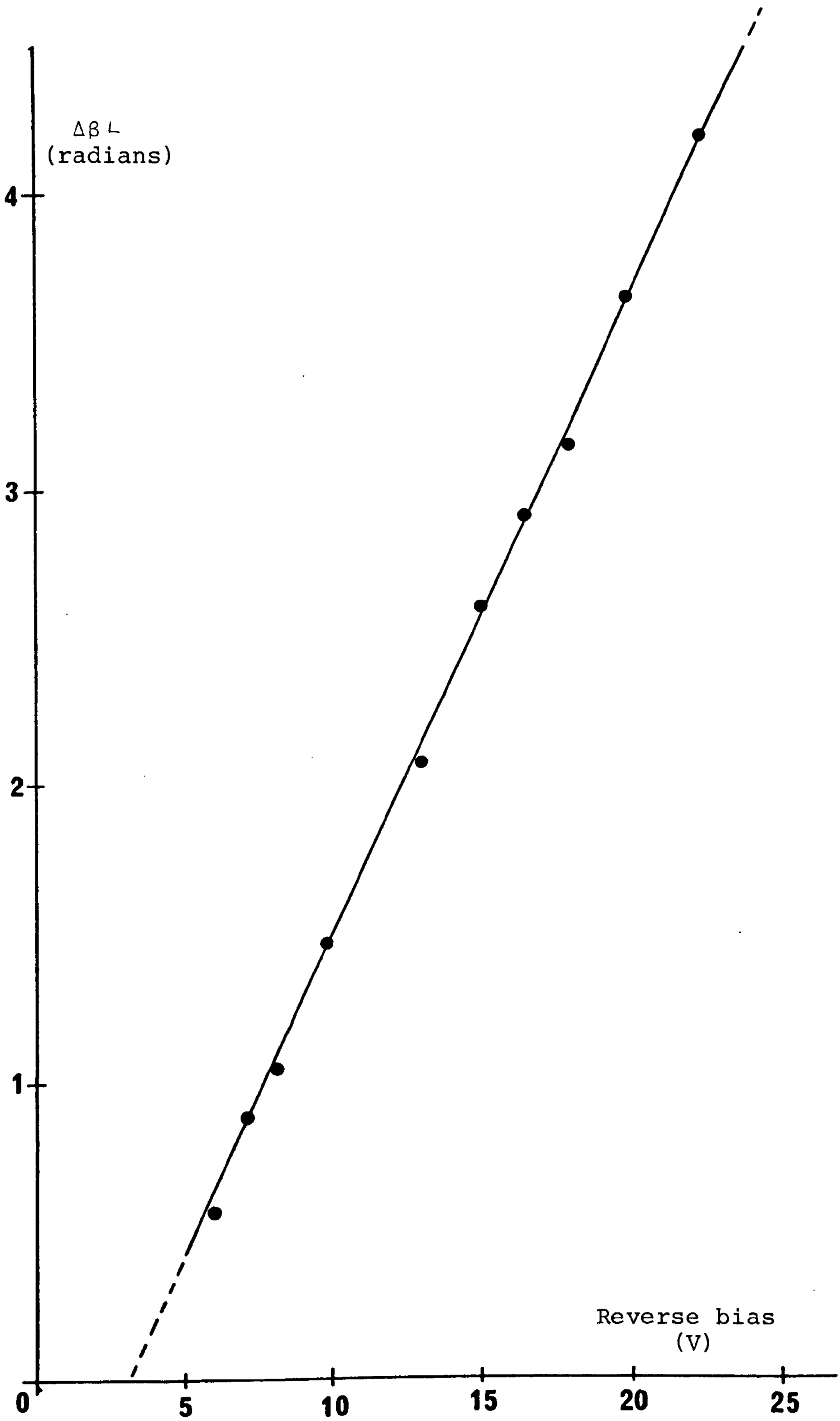

Fig.6.11 Phase modulation characteristic obtained from Fig.6.10 using equation (6.7).

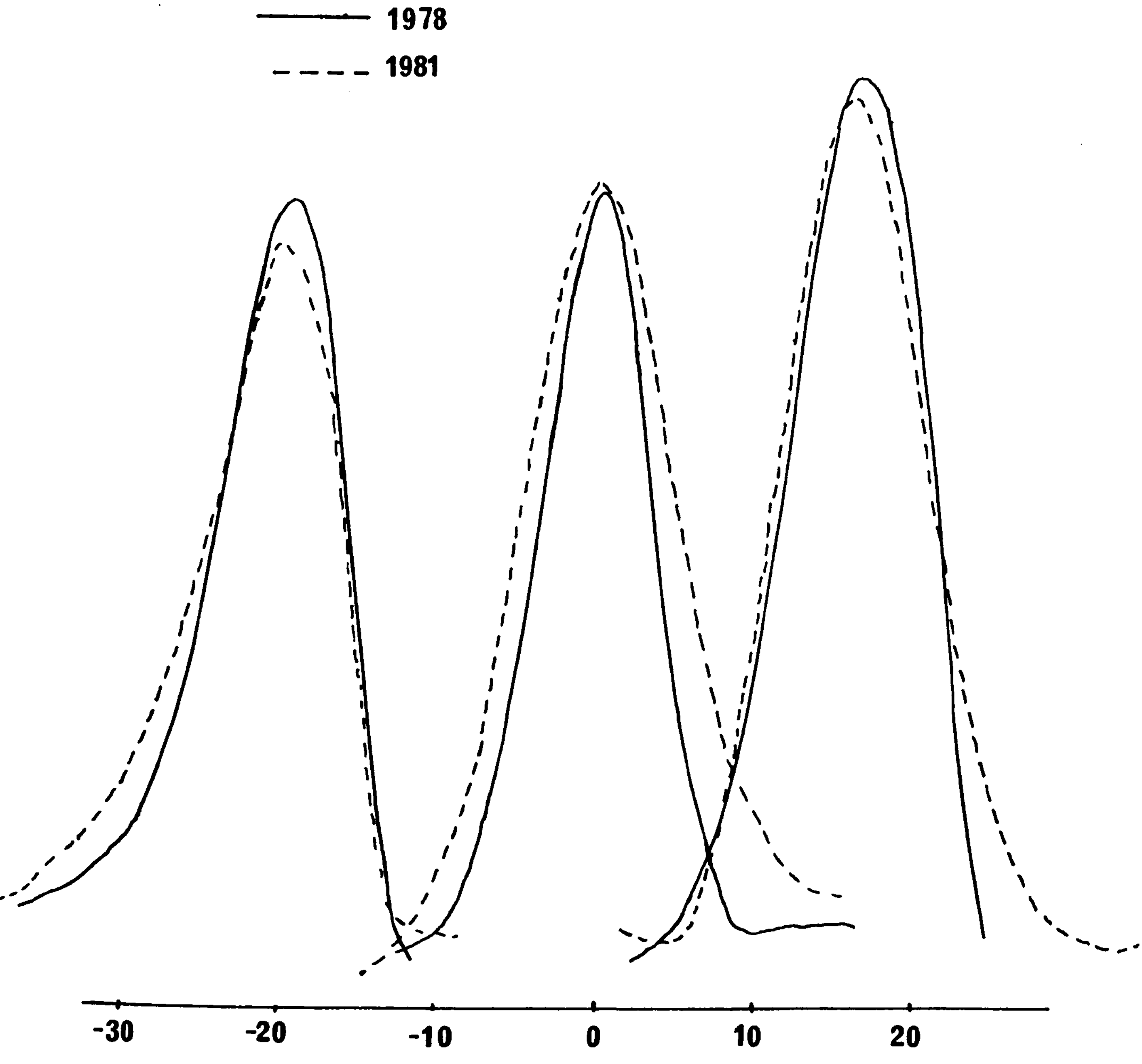

Fig.6.12 The three TM mode profiles of device A18YA measured in 1981 and by Westbrook [24] in 1978.

The three guiding regions observed in the stripe devices of width 17-30μm suggested that each of the three minima in the $\Delta\varepsilon_r$ profile of Fig.6.13 is capable of supporting a waveguide mode. Westbrook analysed the guiding properties by approximating the refractive-index profiles to ones for which the wave equation can be solved analytically. He chose a parabolic profile for the centre regions and $1/\cosh^2$ ones for the edge regions. The experimental results he obtained showed good agreement with his theoretical predictions.

To gain further insight into the validity of these approximations the guiding properties of an edge waveguide ($F = 360$ Nm^{-1}) were analysed using the $1/\cosh^2$ approximation, an exponential one [26], [75] and a one-dimensional finite-difference technique. Using the refractive index variation at a depth of 2μm the intensity half-widths and effective refractive indices of Table 6.4 were found. Effective indices obtained using the finite-difference method at depths of 1.5μm and 2.5μm are 3.440975 and 3.44064 respectively and corresponding half-widths are 5μm and 6.3μm. For a full two-dimensional analysis field profiles at each depth were in precise agreement with the finite-difference values above and a value of $N_{eff} = 3.43845$ is obtained (this analysis includes the substrate refractive index of 3.4375). Experimentally determined half-widths were 7.6μm for a TE mode and 7.3μm for a TM mode.

Finite-difference calculations for a 28μm stripe with $F = 360Nm^{-1}$ show light mainly guided in the edge region with a secondary peak under the stripe centre having a maximum

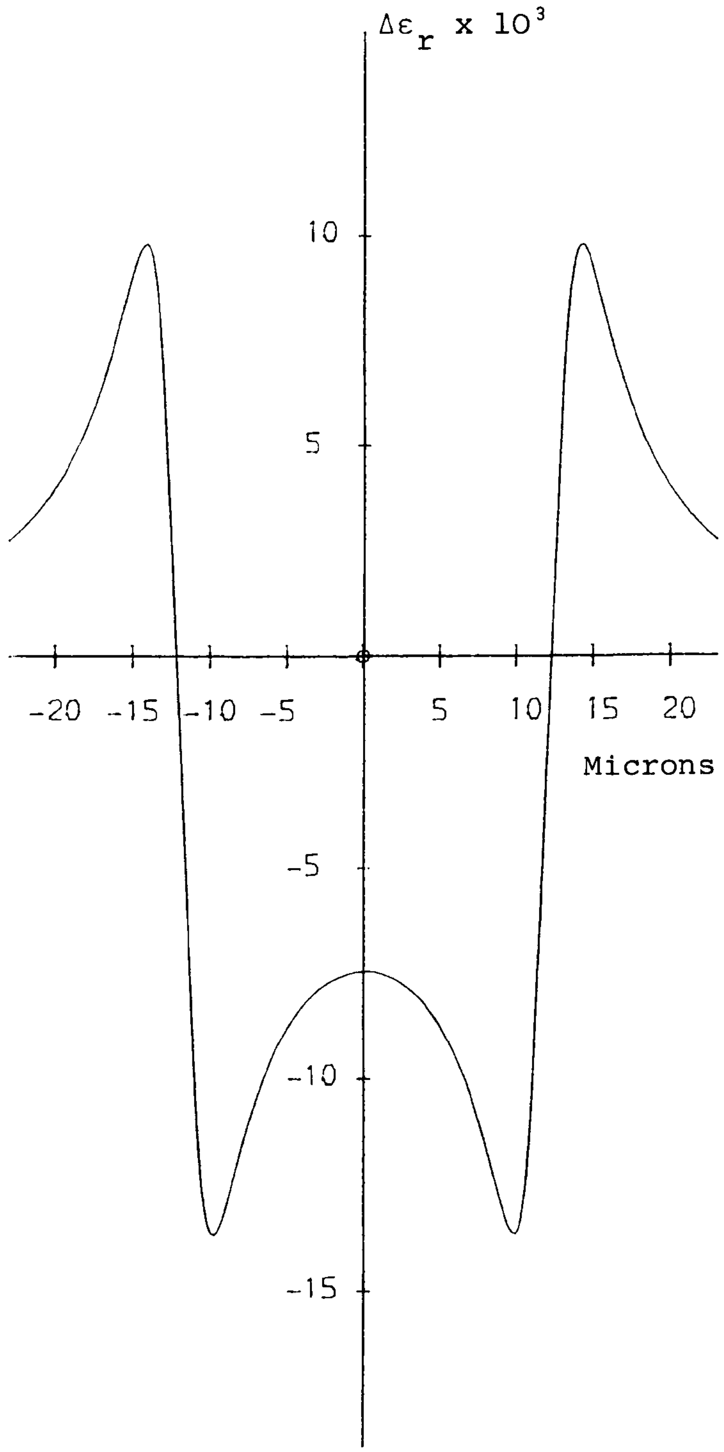

Fig.6.13 The variation of ε_r with y for TE polarised waves at a depth of 1.5μm produced beneath a 24μm wide stripe (F = 360Nm^{-2})

amplitude less than 20% of that in the edge mode. By artificially forcing zero field "walls" at the stripe edges modes with half-widths of 11μm and 12μm are found under a 27μm stripe with $F = 360Nm^{-1}$ and $1200Nm^{-1}$ respectively. The parabolic profile approximation of Westbrook predicts a half-width of 10.6μm for $F = 360Nm^{-1}$.

In device 10FE80A6, with a 10μm stripe width, no central guiding region was found. This is in agreement with strain-induced refractive index changes since the central guiding region vanishes for this stripe width as illustrated by the perturbation in ε_r for TE waves shown in Fig.6.14.

It was shown in section 3.1 that by evaporating aluminium onto a substrate pre-cooled using a Peltier cooling element metal films with no measurable stress could be formed. A stripe of width 12.7μm was formed in such a film using a 5 : 1 orthophosphoric acid : acetic acid etch at 70°C and a positive-photoresist mask. No waveguiding was observed in this sample. As the laser was coupled into slab modes a short distance to either side of the stripe some bright and dark regions were observed in the guiding layer. As the stripe was approached the spacing of these increased until just the bright centre region remained and finally this spread out and disappeared. The origin of these regions is thought to be interference between the incident light and that reflected from the region under the stripe. This indicates some very slight change in refractive index either due to the loading effect of the metal on effective refractive index or to a small residual metal stress not detectable by the method of section 3.1.

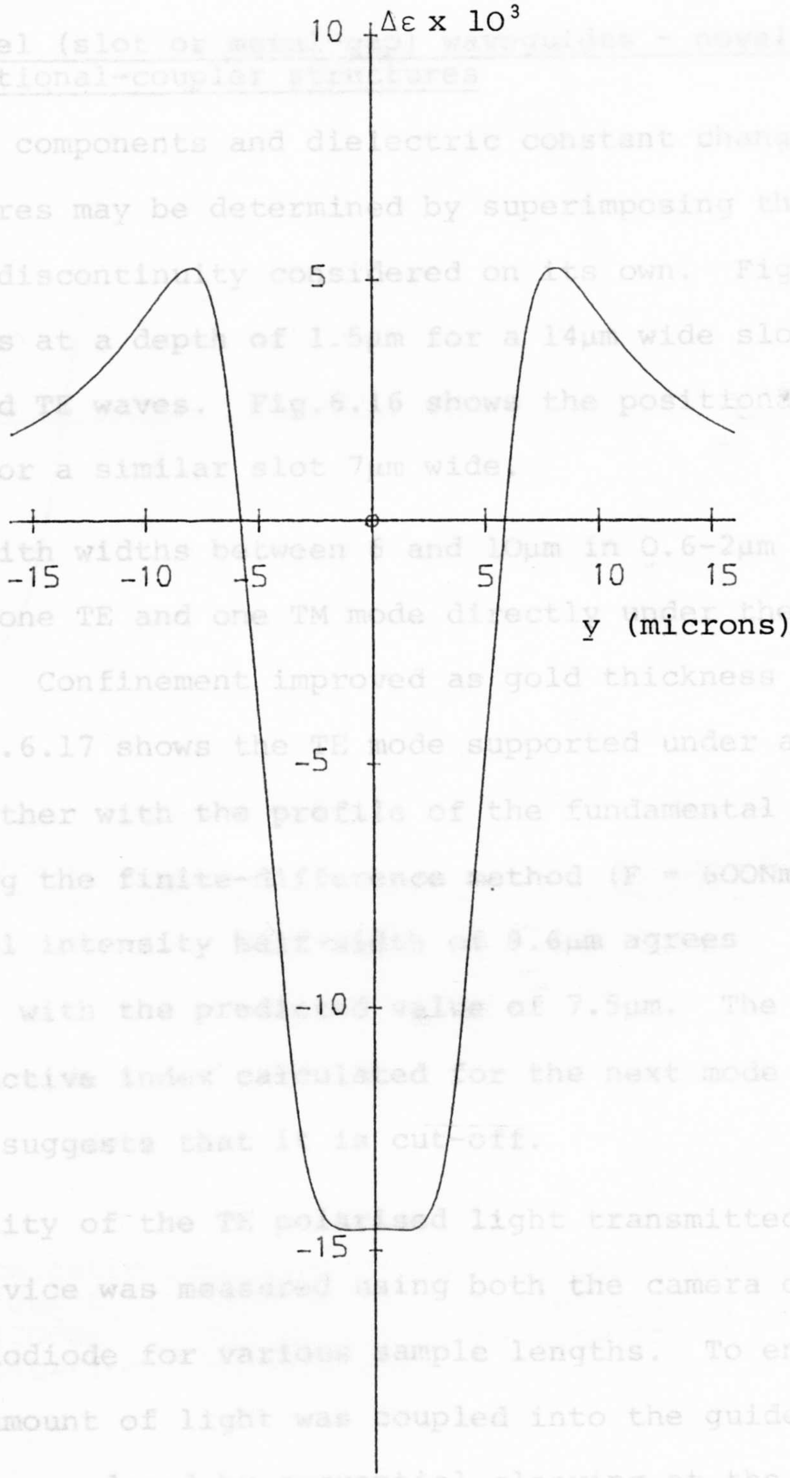

Fig.6.14 The variation of ε_r with y for TE polarised waves at a depth of 2μm produced beneath a 10μm wide stripe (F = 360Nm^{-1})

The bright and dark interference bands were observed in all the stripe samples examined but in general an edge waveguide was seen on approaching the stripe edge.

6.5.3 Channel (slot or metal-gap) waveguides - novel directional-coupler structures

The strain components and dielectric constant changes in channel structures may be determined by superimposing those found for each discontinuity considered on its own. Fig.6.15 illustrates this at a depth of 1.5μm for a 14μm wide slot with $F = 1200\,Nm^{-1}$ and TE waves. Fig.6.16 shows the positional change in $\Delta\varepsilon_r$ for a similar slot 7μm wide.

Channels with widths between 6 and 10μm in 0.6-2μm of gold supported one TE and one TM mode directly under the channel centre. Confinement improved as gold thickness was increased. Fig.6.17 shows the TE mode supported under a slot 10μm wide, together with the profile of the fundamental mode calculated using the finite-difference method ($F = 600\,Nm^{-1}$). The experimental intensity half-width of 9.6μm agrees reasonably well with the predicted value of 7.5μm. The effective refractive index calculated for the next mode in this structure suggests that it is cut-off.

The intensity of the TE polarised light transmitted through this device was measured using both the camera output and the Ge photodiode for various sample lengths. To ensure that the same amount of light was coupled into the guide the device length was reduced by sequential cleaving at the output side only and aligned by observing that the sample remained in focus over all of the cross-section when viewed using white

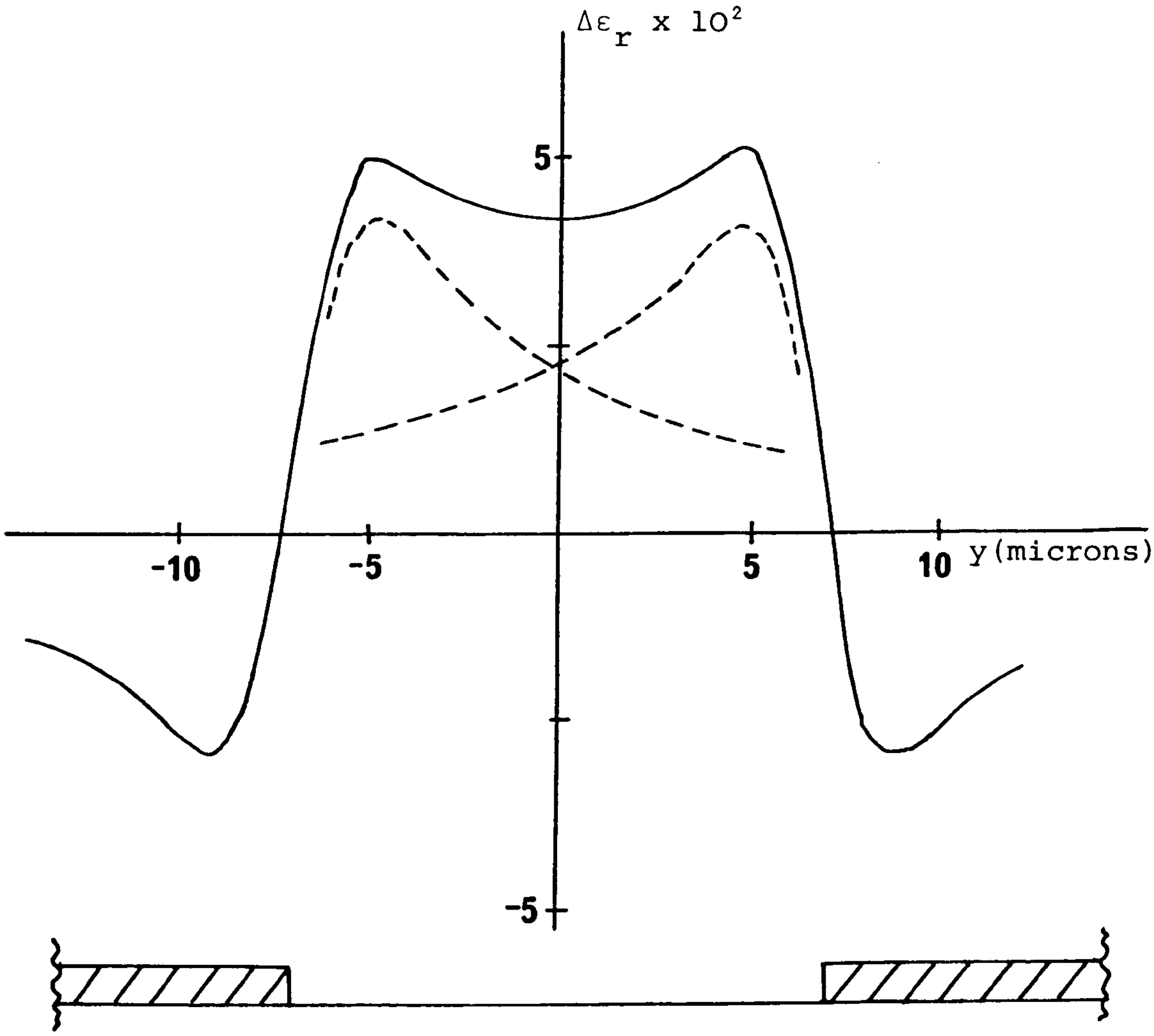

Fig.6.15 Photoelastic contribution to dielectric constant at a depth of 1.5μm for a 14μm slot with $F = 1200Nm^{-1}$. The dotted lines show the contribution from each edge.

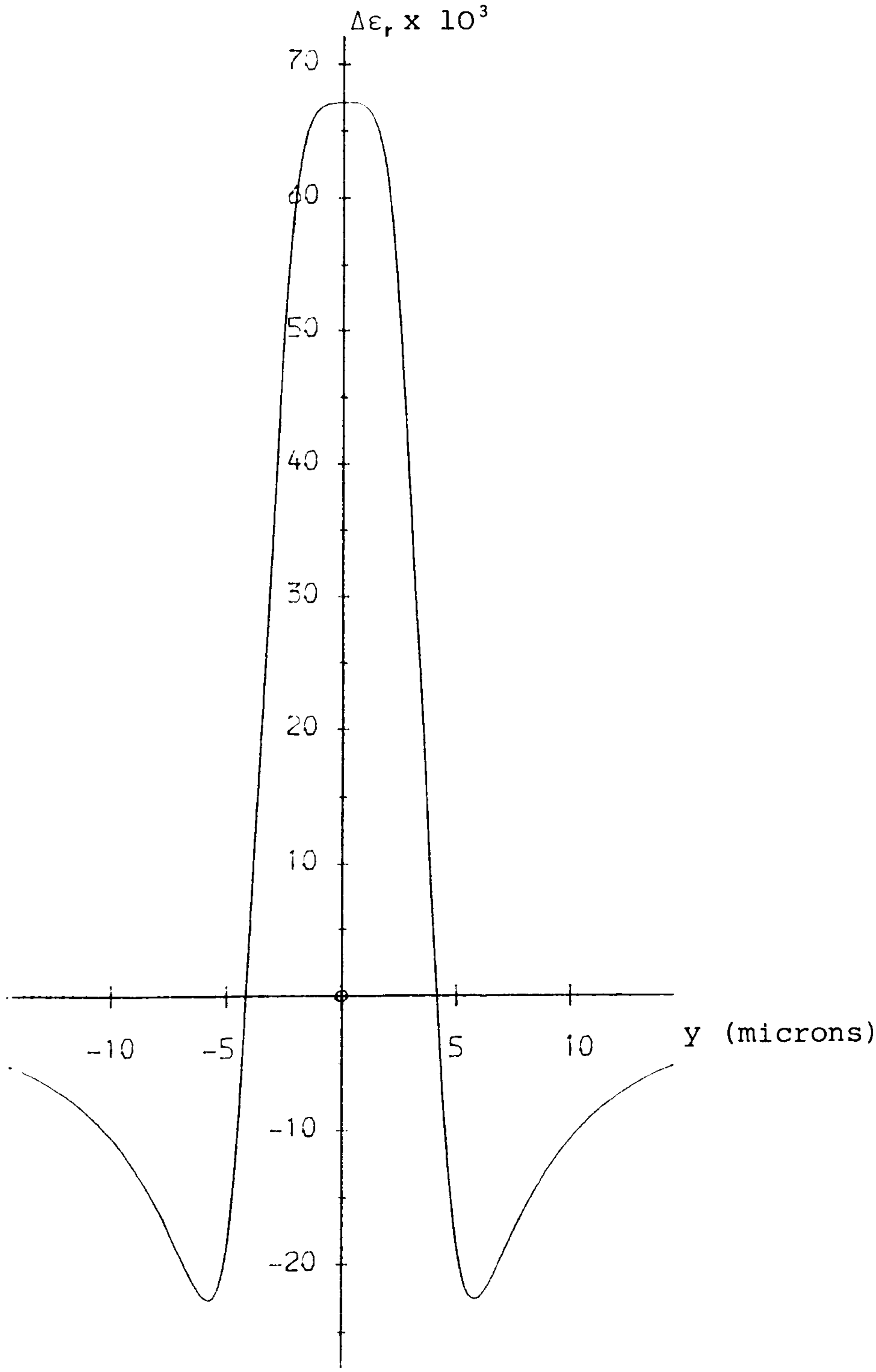

Fig.6.16 Variation of ε_r with y for TE polarised waves at a depth of 1.5μm produced beneath a 7μm slot ($F = 1200Nm^{-1}$)

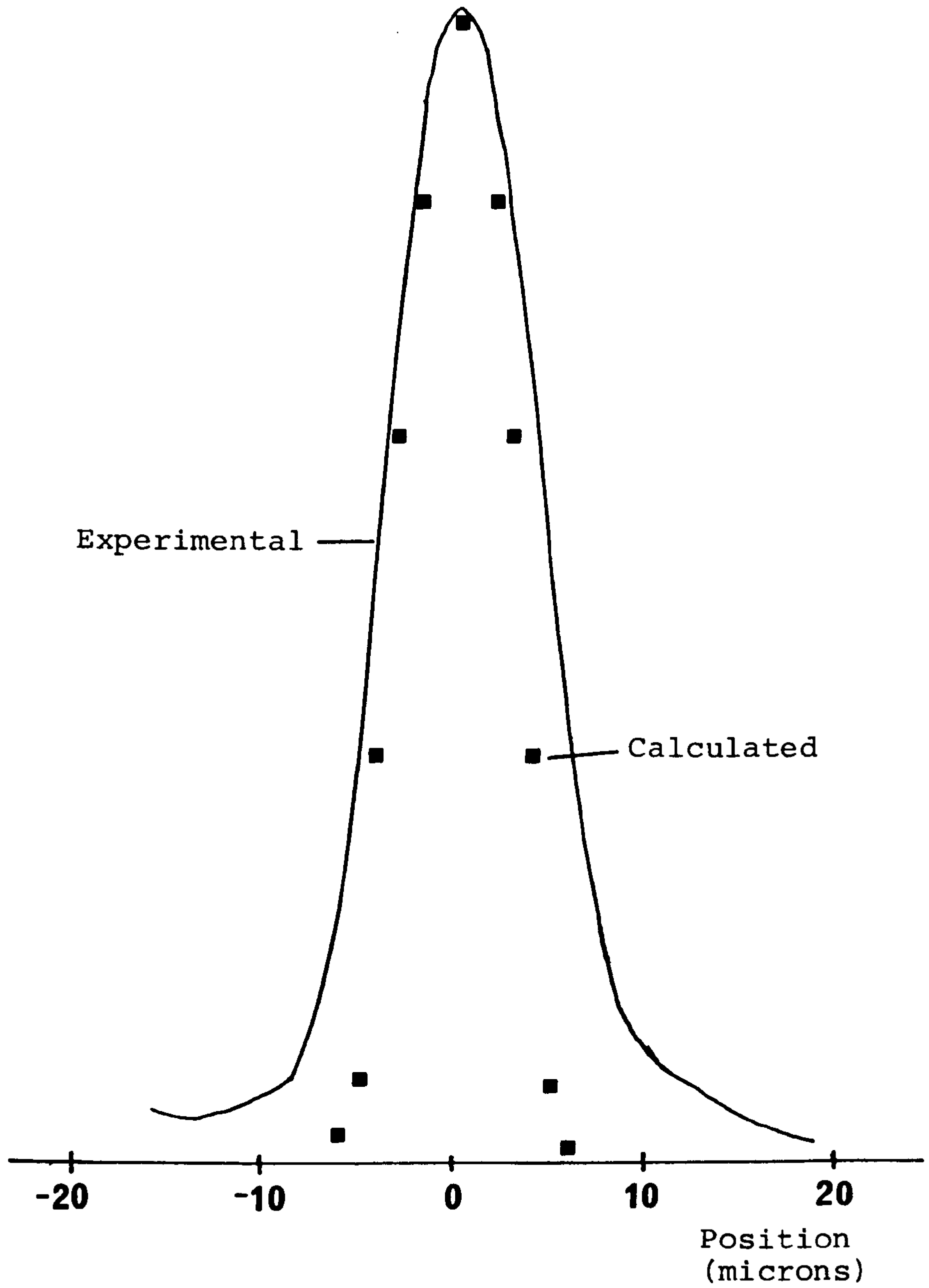

Fig.6.17 Predicted and experimental profiles for the TE mode supported by a 10μm-wide channel in a 1μm thick gold film.

light from the back illuminator. Fig.6.18 gives the resulting plot of $\log_e$ (intensity) against sample length.

If the intensity varies as :

$$I = I_o \exp(-\alpha Z) \tag{6.9}$$

a value for the attenuation coefficient α of 1.7cm^{-1} is found from the gradient of Fig.6.18. This value is in good agreement with the predictions made in section 6.2. The epitaxial layer thickness was $2.8\mu\text{m}$ and its carrier concentration $6\text{-}8 \times 10^{15}\text{cm}^{-3}$. Multiple reflections can be ignored as they contribute less than 3% to the total output intensity even for the shortest sample length used (2.5mm).

By extrapolating the straight line of Fig.6.18 to Z = 0 comparison can be made with the intensity of the incident laser beam (found with a neutral density filter included in the optical system). If 30% reflection is assumed at each cleaved facet [76] an extra loss of ≈10% is found. This can be explained by imperfect matching between the exciting laser beam and the guided- wave profile and the resulting excitation of unwanted slab modes. Total insertion loss of a sample 2mm long is therefore 5.5dB.

For a channel width of $15\mu\text{m}$ and a gold thickness of $2\mu\text{m}$ two guiding regions were observed with a centre separation of about $12\mu\text{m}$. The two regions were observed simultaneously with relative light intensities dependent upon the sample length. The relative light intensity in the initially excited guide followed closely a $\cos^2$ variation with sample length as in Table 6.5. It follows from the discussion of Appendix 9.8

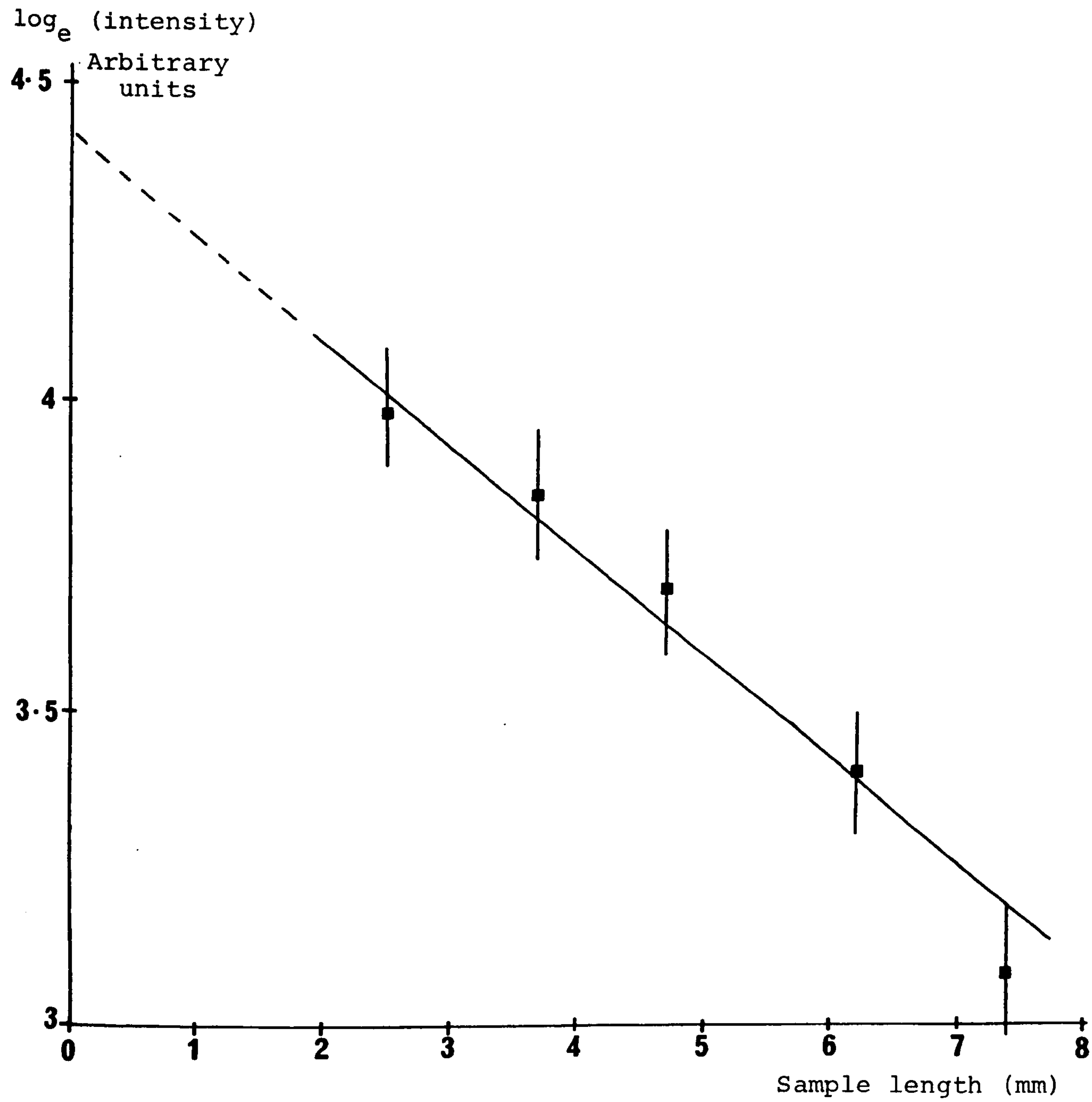

Fig.6.18 $\log_e$ (intensity) as a function of sample length for the waveguide described in Fig.6.17.

that the structure forms a novel, highly synchronous directional coupler. The coupling length, L_c, consistent with the experimental results of Table 6.5 is (2.2 ± 0.2)mm. Thus two synchronous waveguides forming the directional coupler are the respective edge guiding regions at each discontinuity forming the channel. As the laser beam was scanned across the waveguide input slab guiding could be seen at first, then the intensity pattern corresponding to exciting one guide, then nothing, then the intensity pattern for excitation of the second guide and finally slab guiding once more. The input coupling lens moved about 12μm between excitation positions in agreement with the guide separation measured from the near-field intensity pattern.

Applying a bias to one electrode introduces a propagation constant difference $\Delta\beta$ in one guide through the electro-optic effect and so alters the amount of light in each guide at the output facet. From the coupled-wave theory of Appendix 9.8 it is expected that the power in the initially excited guide obeys :

$$P_{excited} = \cos^2\alpha L + \frac{\Delta\beta^2}{4\alpha^2}\sin^2\alpha L \qquad (6.10)$$

where $\alpha^2 = \{C^2 + (\frac{\Delta\beta}{2})^2\}$ and C is the coupling coefficient, $C = \pi/2L_c$. It was mentioned in section 4.1.2 that the total metallised area of the device was reduced to give the configuration of Fig.4.2. A guided mode could be excited at the edge of each electrode remote from the channel and the electro-optic interaction with the TE mode measured using the method of section 6.5.1. This value of $\Delta\beta$ can be used as an estimate of the phase change introduced between the two coupled TE waves in the directional coupler on the application of bias to one electrode. Equation (6.10) may then be used to estimate the power in the initially excited guide as a function of bias; giving the plot of Fig.6.19 for a 15μm wide channel 1.9mm long, assuming a coupling length of 2.4mm (which is within the error limits of the L_c value measured by sequential cleaving). This plot is consistent with the experimental results presented in Fig.6.20.

The directional-coupler switch proposed by Kogelnik and Schmidt [18], [19] in which the sign of $\Delta\beta$ is reversed midway along the sample length allows for electro-optic control of the cross-over state (i.e. light at the device output is confined to the non-excited or coupled guide) for a broad range of sample lengths greater than L_c. This can only be achieved for a sample length of $(n+1)L_c$ where n is an integer for normal biasing. In principle both switch states can be achieved using a reversed $\Delta\beta$ configuration but in practice uniform biasing requires a lower value of $\Delta\beta$ to achieve the "straight through" state.

The device was realised by etching a 20μm gap in each electrode perpendicular to the guiding channel. Bias voltage may then be applied in such a way that the sign of $\Delta\beta$ is reversed along the sample length or kept the same. Extra loss introduced by the gap was negligible.

Fig.6.21 presents experimental results on the transfer of light with applied bias for a 15μm wide channel orientated along the (011) crystallographic direction for a device with

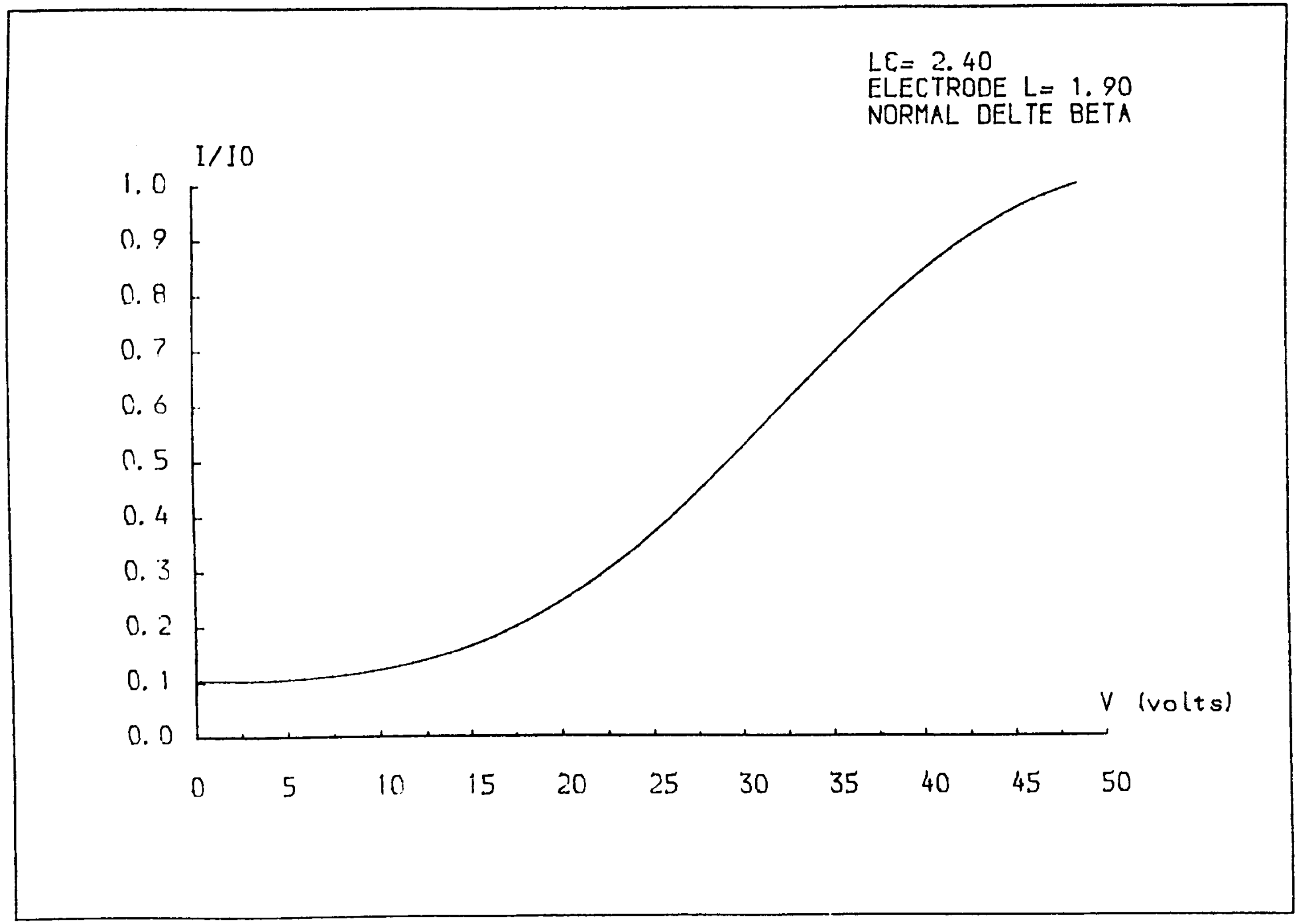

Fig.6.19 Calculated normalised power at the output of excited guide as a function of bias for a 1.9mm length of a 15μm wide channel waveguide. L_c = 2.4mm

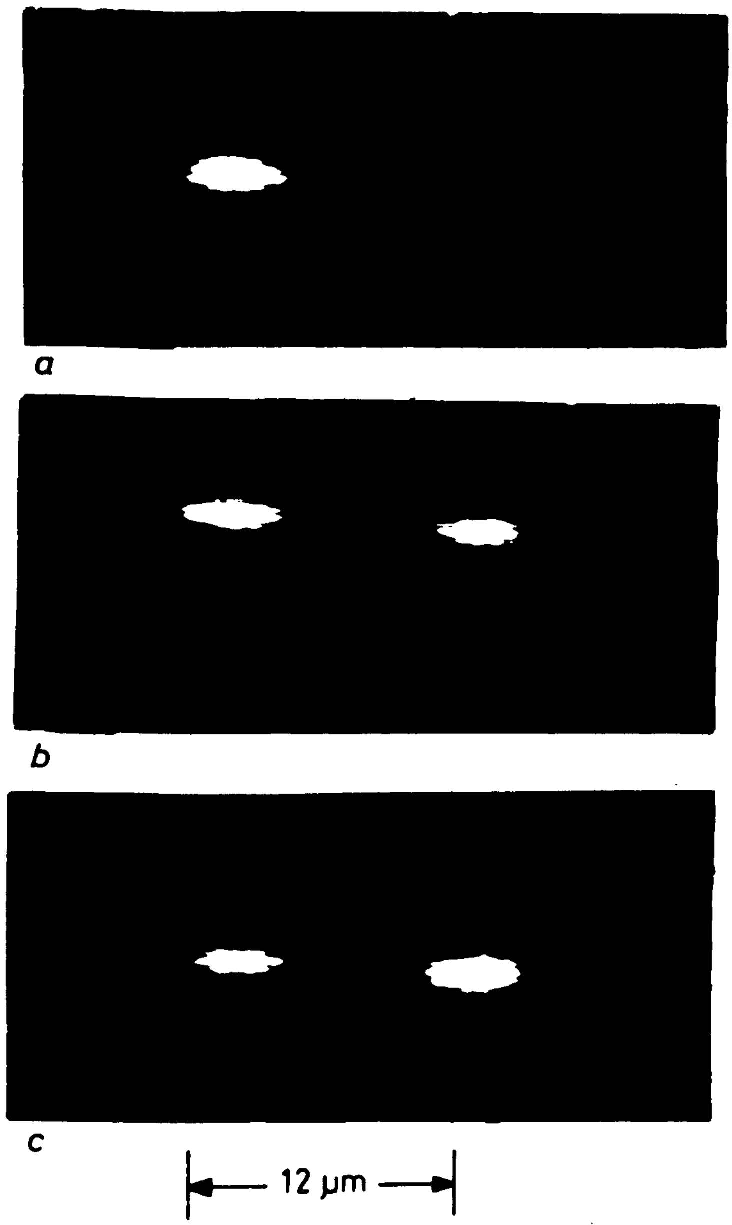

Fig.6.20 Near-field intensity pattern at the output of a 15μm wide channel 1.9mm long. At the waveguide input, the laser is focussed on the right-hand guide (a) with zero bias light emerges mainly from the unexcited guide since sample length $\approx L_c$. For biases of -21V (b) and -30V (c) on the right-hand electrode the amount of light coupled to the non-excited guide is reduced.

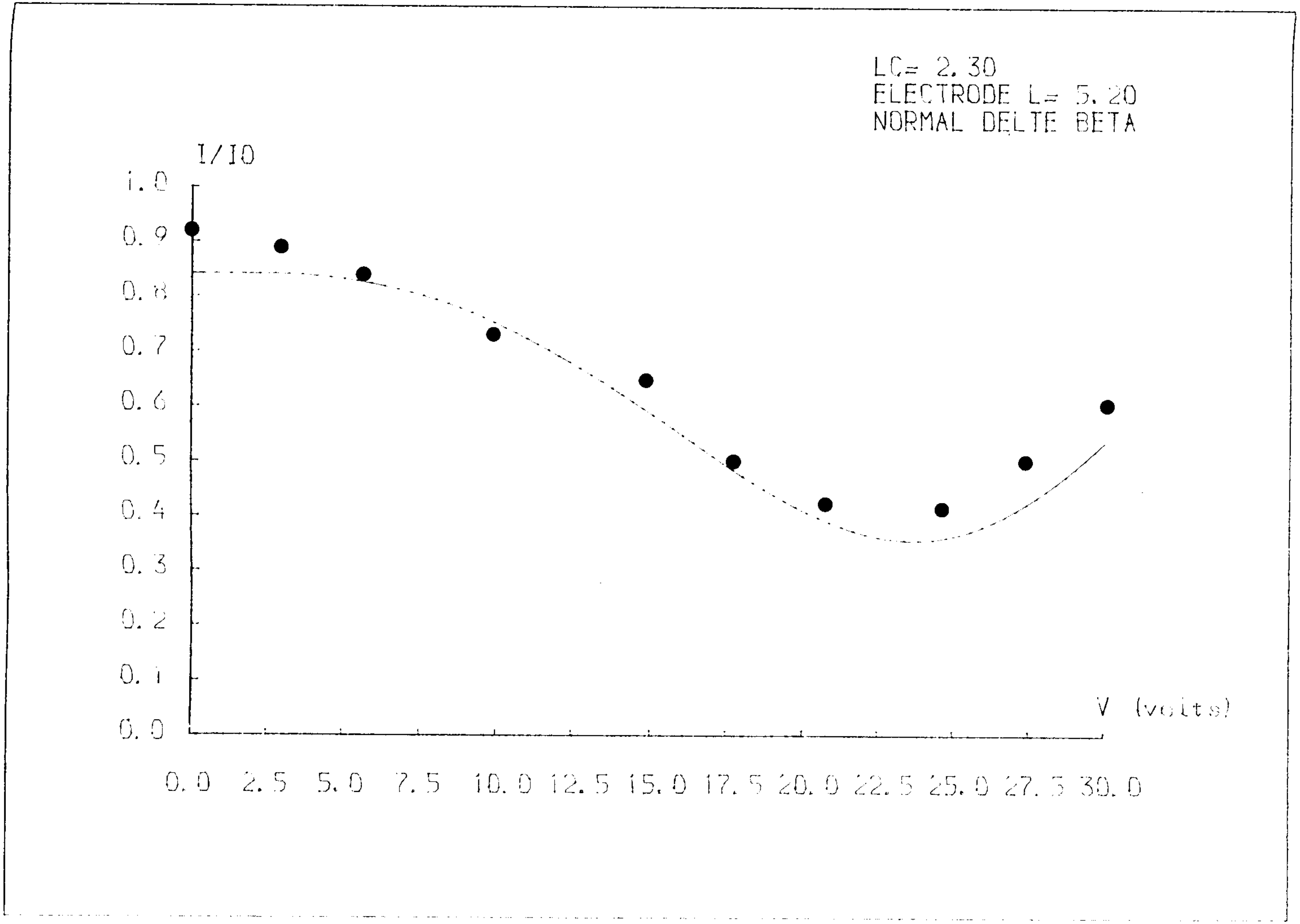

Fig.6.21 Plot of the intensity in the initially excited guide, normalised to the total intensity as a function of bias V in the normal $\Delta\beta$ configuration. Points are experimental, the continuous curve from coupled wave theory.

electrode lengths 2.9mm (near the input) and 2.3mm (near the output). Bias was applied in the normal $\Delta\beta$ configuration and unbiased electrodes were grounded. Fig.6.21 also gives a curve calculated from (6.10). Biasing in the reverse $\Delta\beta$ configuration (Fig.6.22) gave an improved switching performance with 9% of the light emerging from the excited guide at a bias of -20V. The best isolation obtained was 15dB in the crossed-over state (3% of the intensity in the excited guide) using a reverse $\Delta\beta$ configuration with the bias on the first electrode -15V and that on the second electrode -20V. The different biases are required because of the unequal electrode lengths enforced by a fabrication error. Families of curves taken for this device by fixing the bias on the "input" electrode at values between 0 and 30V and varying the bias on the "output" electrode all showed good agreement with the predictions of coupled-wave theory.

A similar $\Delta\beta$ directional-coupler switch was fabricated with a 14μm channel orientated along the $(01\bar{1})$ crystallographic direction. Electrode lengths for this device were 2.6 and 1.9mm. It was intended to make this device length equal to $2L_c$ with a channel width of 15μm. Switching into both states was achieved as shown in Figs.6.23 and 6.24 although a rather large bias of -42V was required in the normal $\Delta\beta$ configuration to achieve 13dB isolation in the "straight through" condition. Isolation of 16dB in the crossed-over state (2.5% in the excited guide) was achieved with the reversed $\Delta\beta$ configuration.

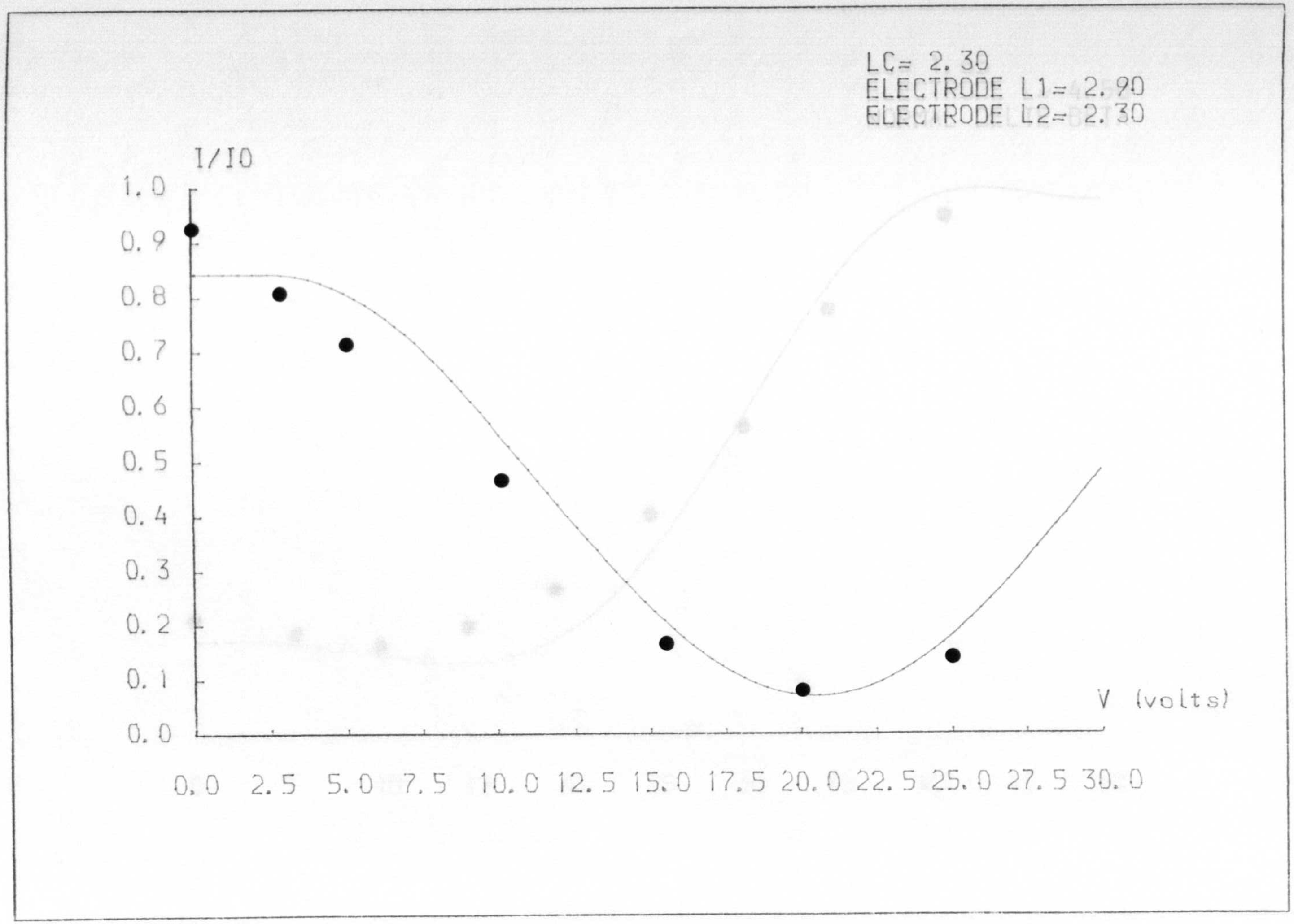

Fig.6.22 Plot of the intensity in the initially excited guide, normalised to the total intensity as a function of bias V in the reversed $\Delta\beta$ configuration. Points are experimental, the continuous curve from coupled wave theory.

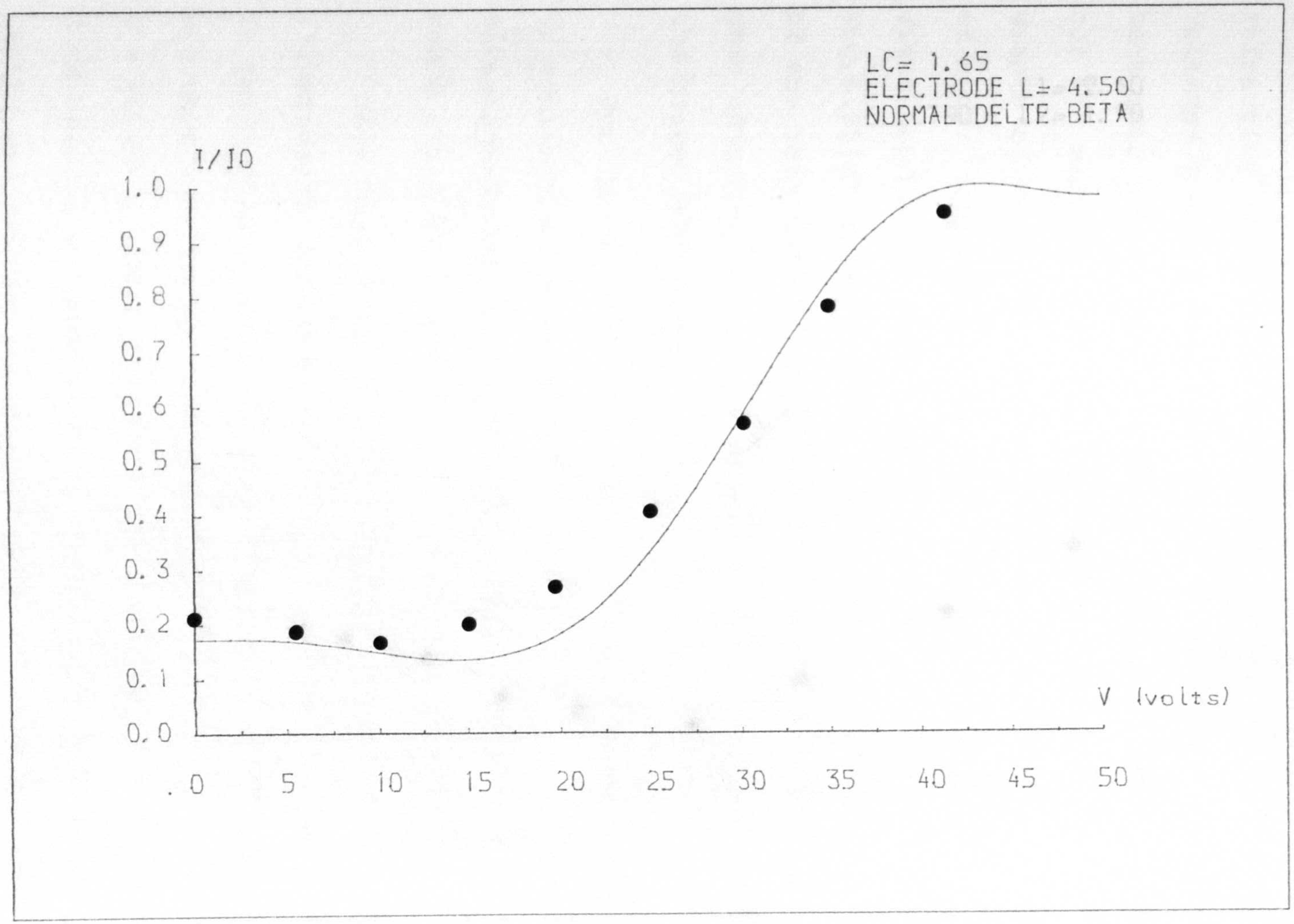

Fig.6.23 Normalised intensity in excited guide as a function of bias in the normal $\Delta\beta$ configuration. Points are experimental, the continuous curve from coupled wave theory.

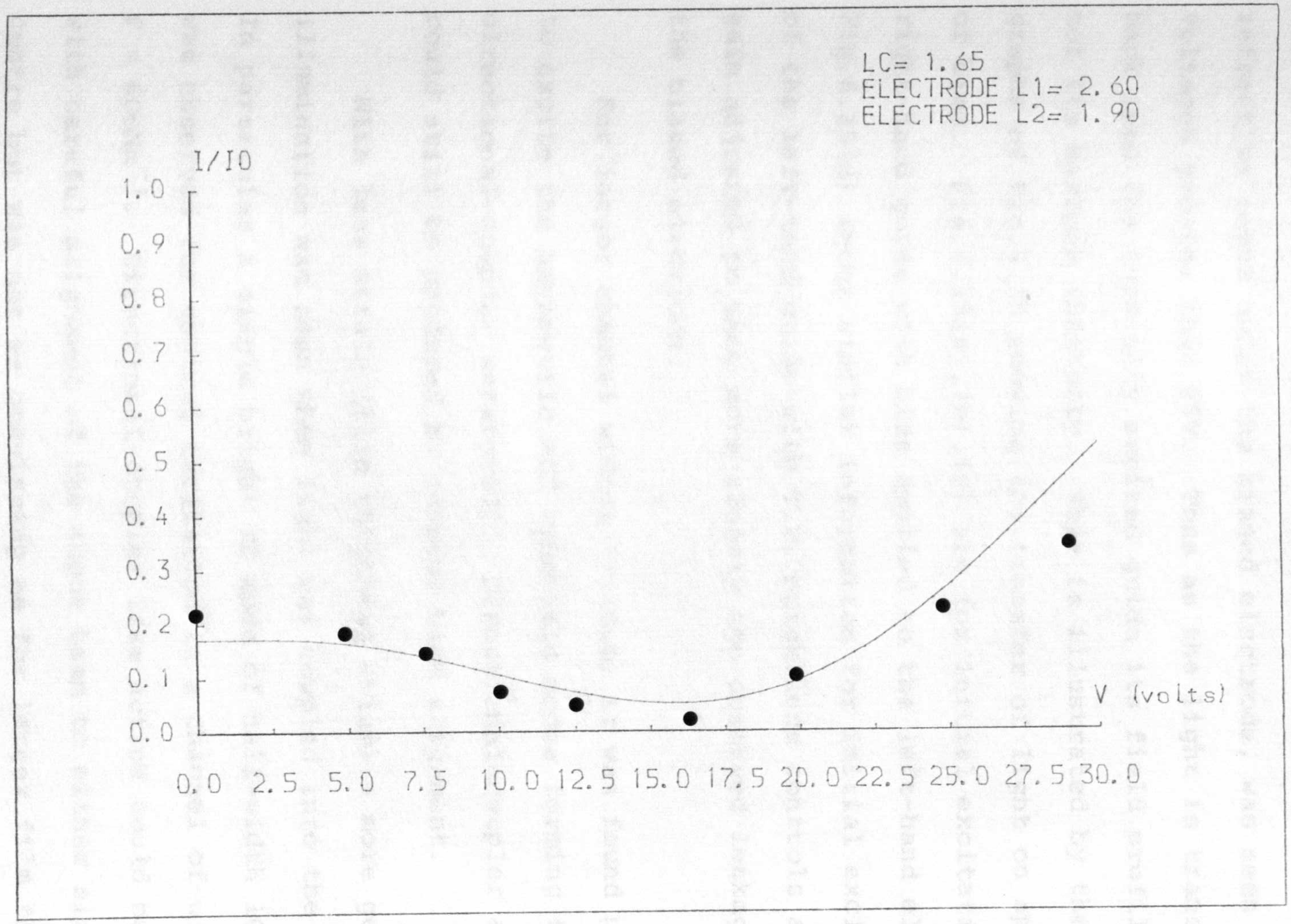

Fig.6.24 Normalised intensity in initially excited guide as a function of bias in the reversed $\Delta\beta$ configuration. Points are experimental, the continuous curve from coupled wave theory.

When bias was applied in the normal $\Delta\beta$ configuration to the electrode pair near the excited waveguide some leakage of light, from the directional coupler to the increased region of refractive index under the biased electrode, was seen for voltages greater than 25V. Thus as the light is transferred back into the initially excited guide its field profile changes not its maximum intensity. This is illustrated by the photographs of Fig.6.25 showing the transfer of light on application of bias. Fig.6.25(a),(b),(c) are for initial excitation of the right-hand guide with bias applied to the left-hand electrode. Fig.6.25(d) shows similar information for initial excitation of the left-hand guide with T.V. brightness controls and camera gain adjusted to show more clearly the observed leakage under the biased electrode.

For larger channel widths ($>\sim 20\mu m$) it was found possible to excite the asymmetric and symmetric modes forming the directional-coupler separately. Directional-coupler action could still be produced by careful beam alignment.

With less strain (film thickness $<\sim 1\mu m$) a more general illumination was seen when light was coupled into the slot. In particular a single bright TE mode of half-width $10.6\mu m$ was observed for central excitation in a channel of width $14\mu m$, $F = 600Nm^{-1}$. Directional-coupler like action could be observed with careful alignment of the input beam to either side of the centre but was not as convincing as for larger film thicknesses.

No change in passive guiding properties has been noticed in channel structures examined regularly over periods of up to 18 months.

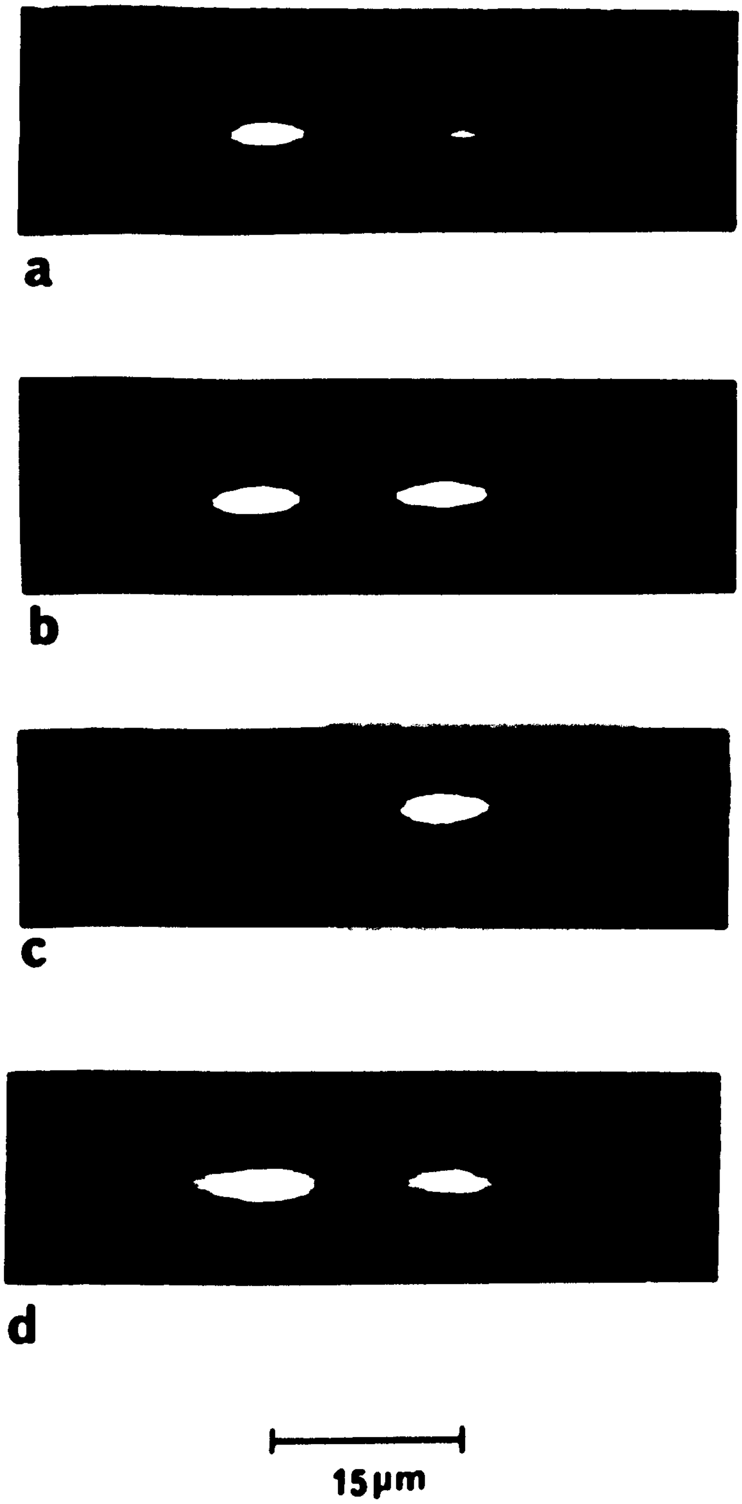

Fig.6.25 Transfer of light on application of bias in the normal $\Delta\beta$ configuration for the device described in Fig.6.23. In (a), (b), (c) the guide on the right-hand side is excited at the input cleave and bias of (a) 0V (b) -25V and (c) -38V applied to the left-hand electrode. (d) shows similar information for initial excitation of the left-hand guide and a bias of -33V. Note leakage under the biased electrode.

Experimentally determined values for the coupling length for various slot widths and gold thicknesses are summarised in Table 6.6. These values and the guiding properties of channels with width between 14 and 20μm are now discussed in the light of results from finite-difference calculations.

The asymmetric and symmetric TE mode profiles are found by considering half the waveguide cross-section and applying relevant boundary conditions at the symmetry plane as described in section 2.3. Fig.6.26 shows the normalised TE amplitude and intensity profiles at 1.5μm calculated for a 14μm slot with $F = 1200Nm^{-1}$. From the amplitudes of the asymmetric and symmetric modes output intensity patterns can be modelled. Fig.6.27 shows the predicted intensity output profiles for $Z = 2nL_c$, $(2n-1)L_c$, $nL_c/2$, $1.38L_c$ and $1.62L_c$. From the superimposition of the computed symmetrical and asymmetrical normal mode profiles (Fig.6.26(a) and (b)) it was noted that a 25dB isolation in each state, in agreement with the value reported by Leonberger and Bozler [20], could be expected. Calculations using coupled-wave theory show that the experimental isolation of better than 16dB in the crossed-over state is limited by the unequal electrode lengths used. Du and Chen [77] show that with equal bias in the reverse $\Delta\beta$ configuration a cross-talk level better than 20dB requires that $|L_1-L_2| < 0.0198 (L_1+L_2)$.

From the calculated effective refractive indices N_S and N_A of the symmetric and asymmetric modes the coupling length, L_c, for the directional coupler was found using (9.55). Fig. 6.28 shows the theoretical variation of L_c with F for a 14μm

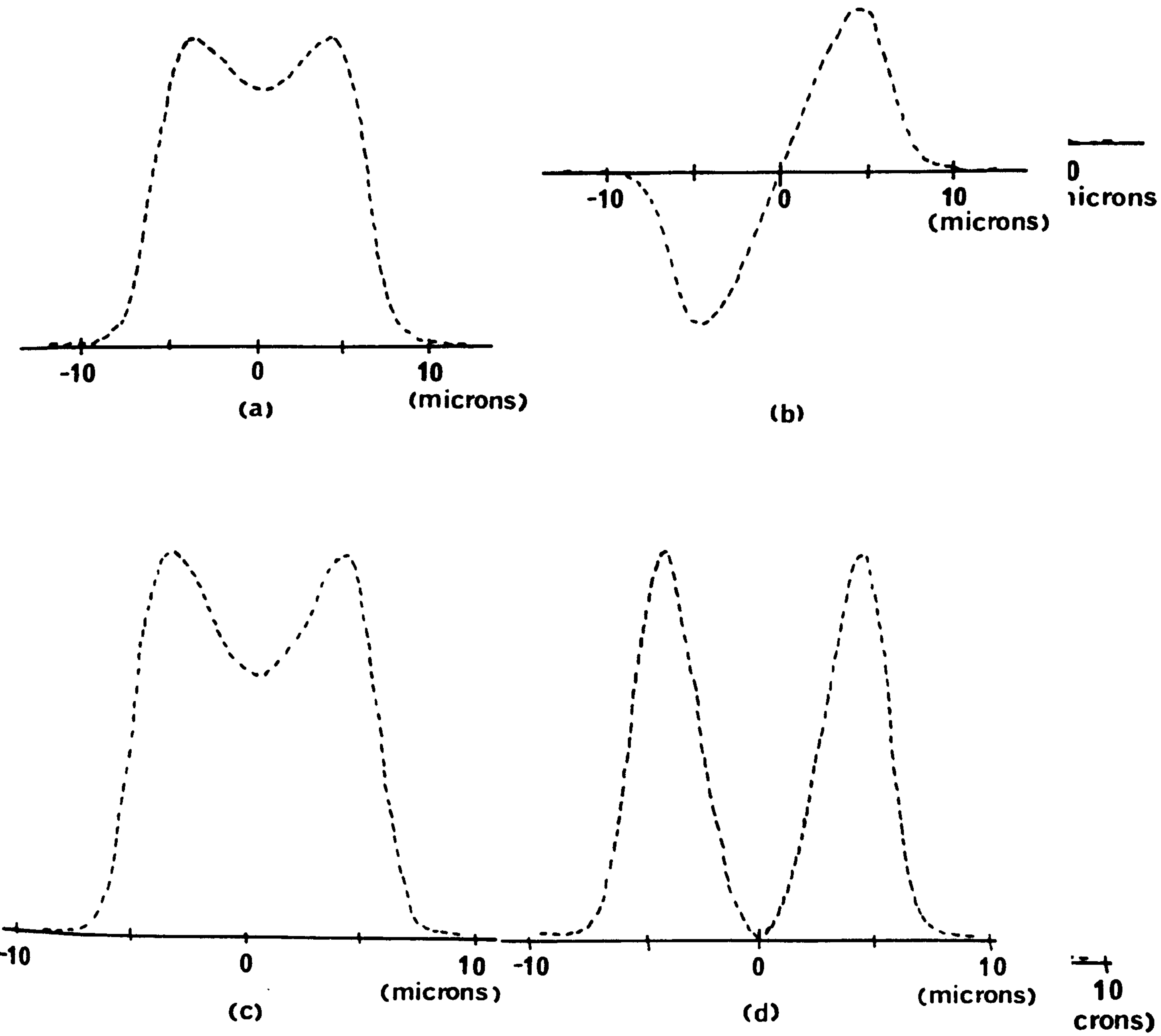

Fig.6.26 Normalised wave profiles at a depth of 1.5μm calculated for the fundamental symmetrical and asymmetrical modes in a 14μm wide slot device with $F = 1200Nm^{-1}$

(a) Amplitude of the symmetrical mode
(b) Amplitude of the asymmetrical mode
(c) Intensity of the symmetrical mode
(d) Intensity of the asymmetrical mode

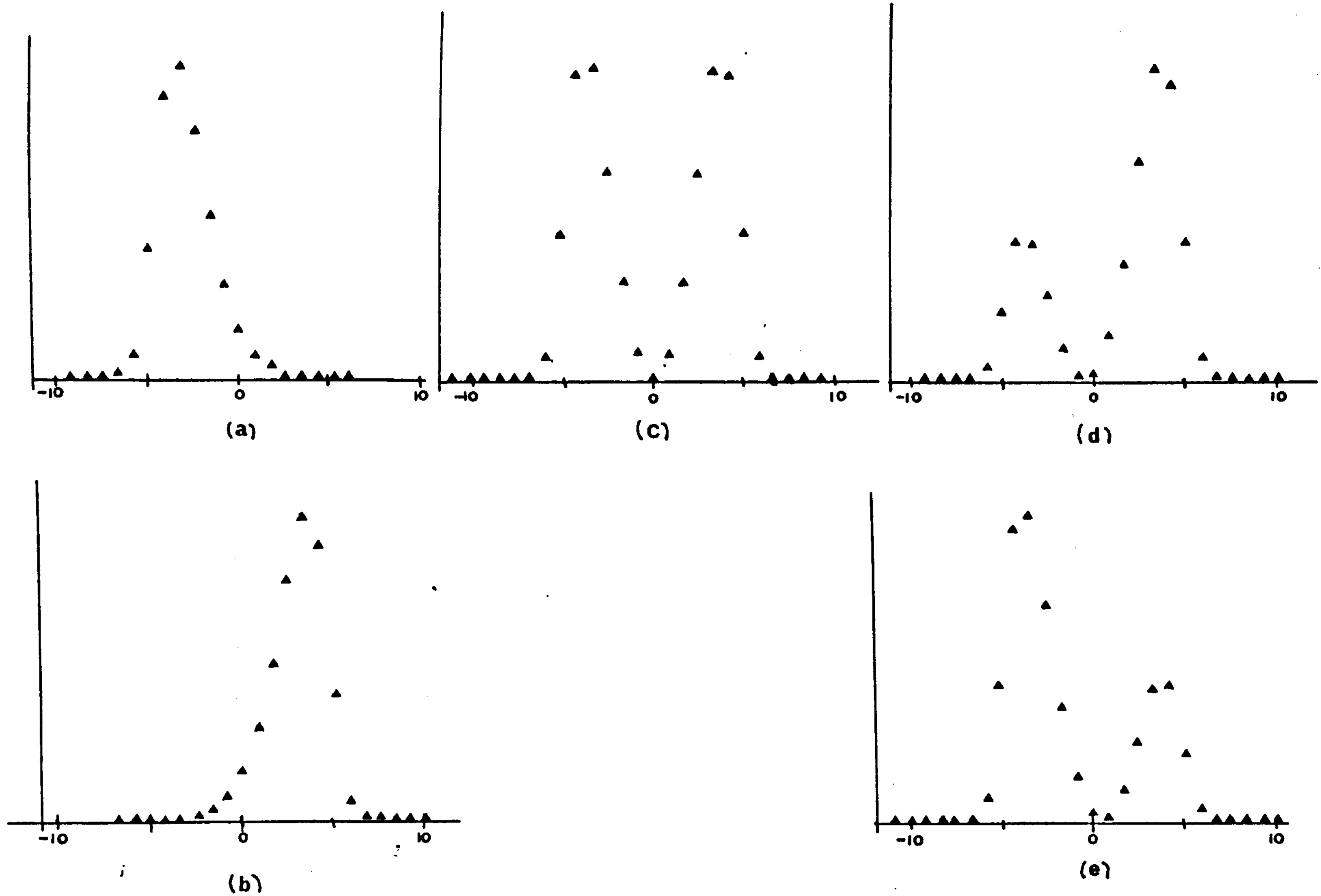

Fig.6.27 Predicted intensity output profiles for (a) $Z = 2nL_c$ (b) $Z = (2n-1)L_c$ (c) $nL_c/2$ (d) $1.38L_c$ (e) $1.62L_c$

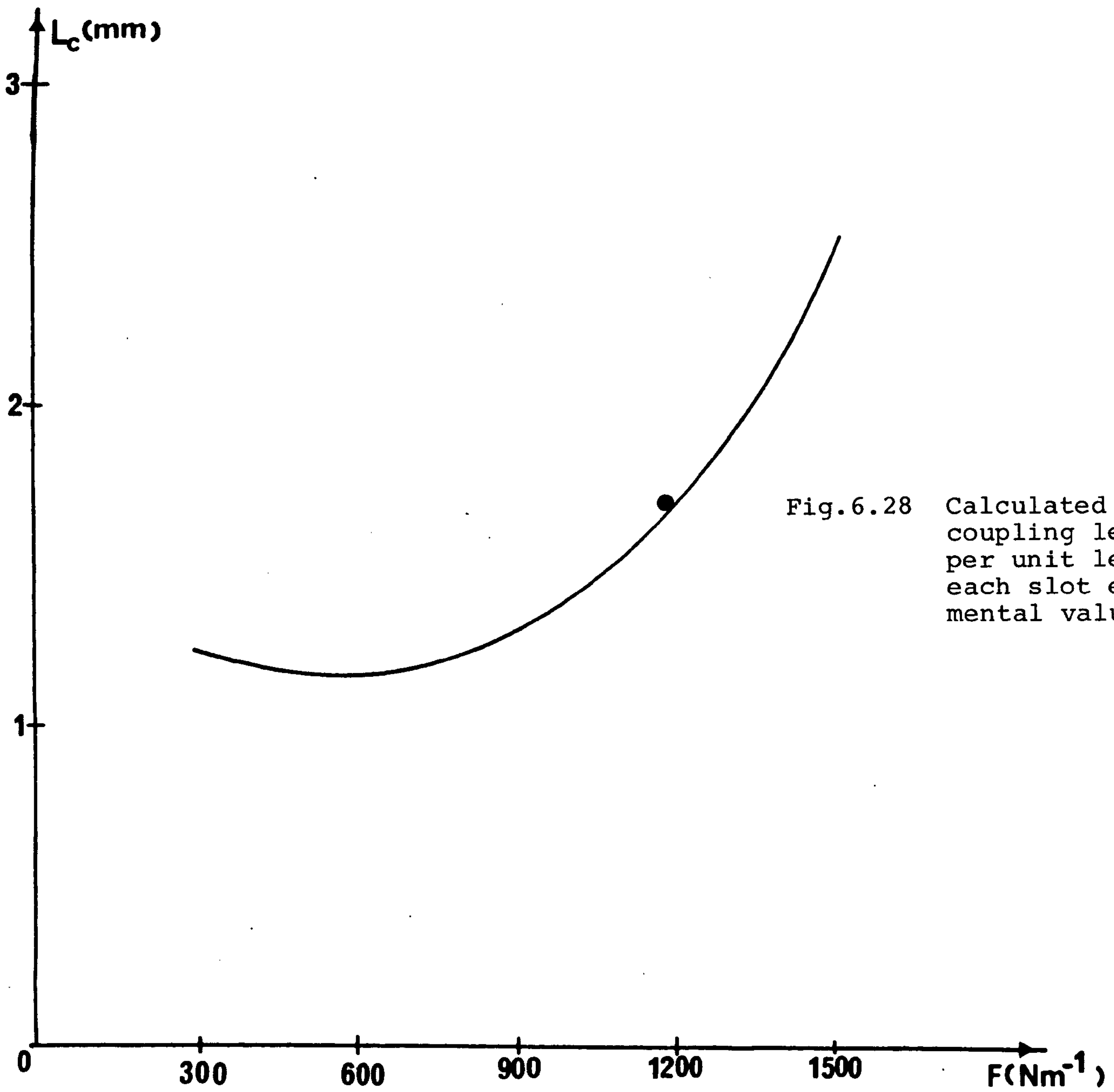

Fig.6.28 Calculated variation of coupling length with force per unit length acting at each slot edge. Experimental value also shown.

channel with a 2.5μm thick epitaxial layer together with experimental values from Table 6.6. Small deviations in epitaxial thickness in the experimental devices have been ignored. As the confinement of each mode increases with F so the coupling between the two guides is reduced and the coupling length increased. The minimum observed in this curve may be explained by imagining an effective index model as in section 2.2.2. For a small refractive index difference $N_{II}-N_I$ Kogelnik [26] shows that the effective refractive indices N_S and N_A may be written in terms of a normalised guide index b as :

$$N_{\substack{A\\S}} \simeq N_I + b_{\substack{A\\S}} \, (N_{II}-N_I) \tag{6.11}$$

$$\text{where } b_{\substack{A\\S}} = \frac{N^2_{\substack{A\\S}} - N_I^2}{(N_{II}^2 - N_I^2)} \, .$$

From (9.55) :

$$L_c = \frac{\lambda}{2(N_S-N_A)} = \frac{\lambda}{2(b_S-b_A)(N_{II}-N_I)} \tag{6.12}$$

As $F \to 0$ $N_I \to N_{II}$ and $L_c \to \infty$. The increase in L_c as $F \to \infty$ described qualitatively above is also explained by this model since $F \to \infty$, $b_S \to b_A$ and $L_c \to \infty$.

By assuming a $\cos^2(Cz)$ variation in intensity in the excited guide Fig.6.28 shows that with F nominally 1200Nm^{-1} a 20% error in strain can be tolerated whilst still maintaining a 90% cross-over condition at the nominal coupling length. Using the thermal-stress model of section 3.1 this corresponds to an operating temperature range of $\pm 45^{\circ}$C. In the directional-coupler of length 4.5mm described, however, light would switch from being mainly in the coupled guide to the excited one for a similar increase in F.

Fig.6.29 presents the theoretical variation of L_c with slot width for $F = 1200Nm^{-1}$, together with experimental data from Table 6.6. In this case L_c increases as slot width is increased and coupling between the two guides is reduced.

Fig.6.30 illustrates the change of L_c with epitaxial thickness. As the layer thickness is increased the field maximum occurs deeper in the material where $\Delta\varepsilon_r$ is smaller. Here lateral confinement is less and coupling lengths are consequently reduced. The reduction of coupling length with depth was confirmed by solving the wave-equation for N_S and N_A for one-dimensional strain-induced refractive index profiles at various depths beneath a 14μm channel with $F = 1200Nm^{-1}$. It is interesting to note that Leonberger et al [78] found a slight increase in coupling length with epitaxial layer thickness for their $p^+n^-n^+$ channel-stop stripe guides. This was confirmed by effective index calculations based on the method of section 2.2.2.

Fig.6.31(a)(b) show intensity profiles of the symmetric and asymmetric modes for a 14μm wide slot with $F = 500Nm^{-1}$. There is no central dip in the symmetric mode profile of Fig. 6.31(a) as for the $F = 1200Nm^{-1}$ case of Fig.6.26. Excitation of this symmetric mode (with a half-width of ∿11μm) would explain the experimentally observed guiding for central excitation in slots with metal thickness 1μm or less.

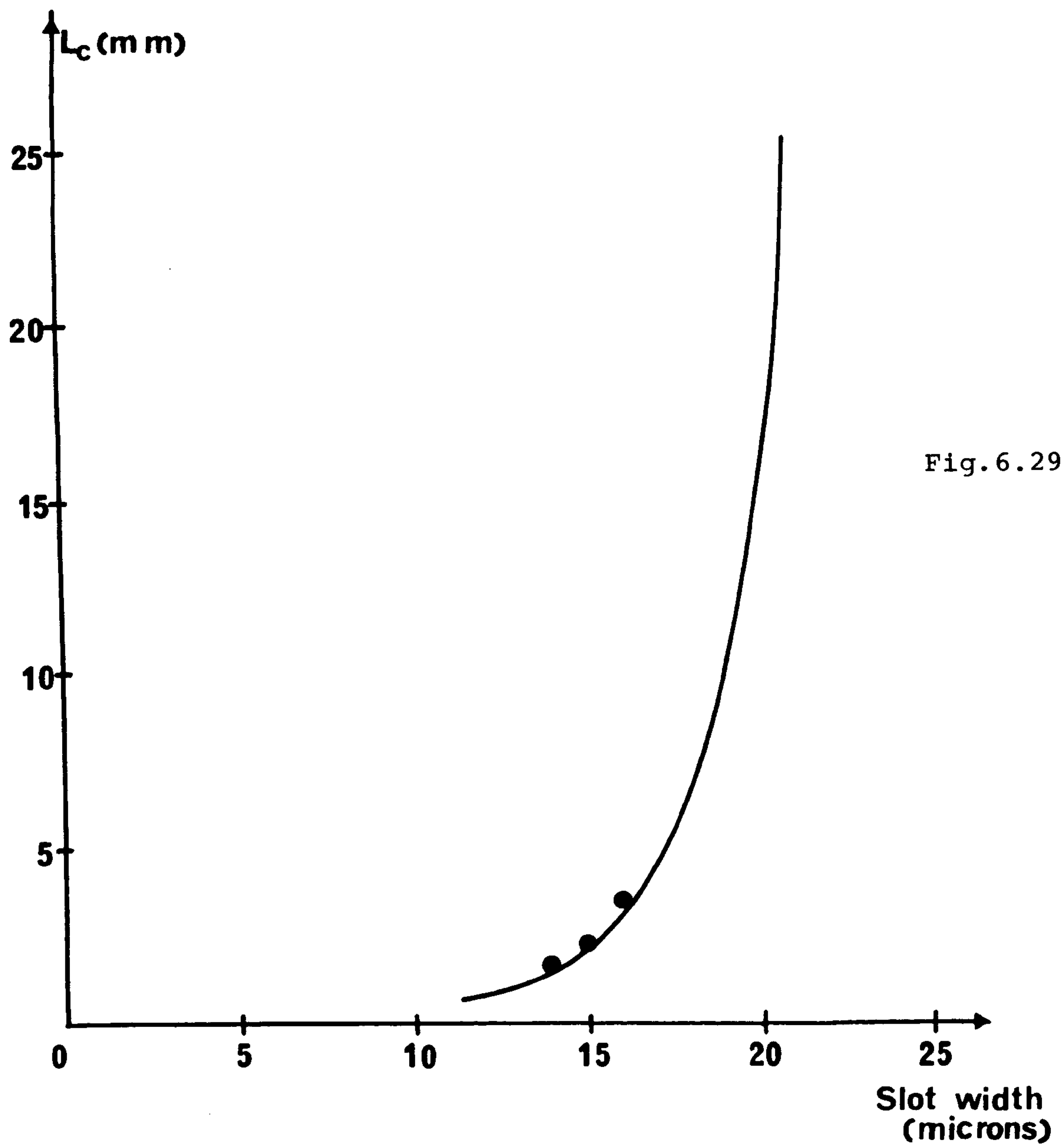

Fig.6.29 Calculated variation of coupling length with slot width, $F = 1200 Nm^{-1}$. Points are experimental values.

Fig.6.30 Calculated variation of coupling length with slot width, $F = 1200Nm^{-1}$. Point represents experimental value.

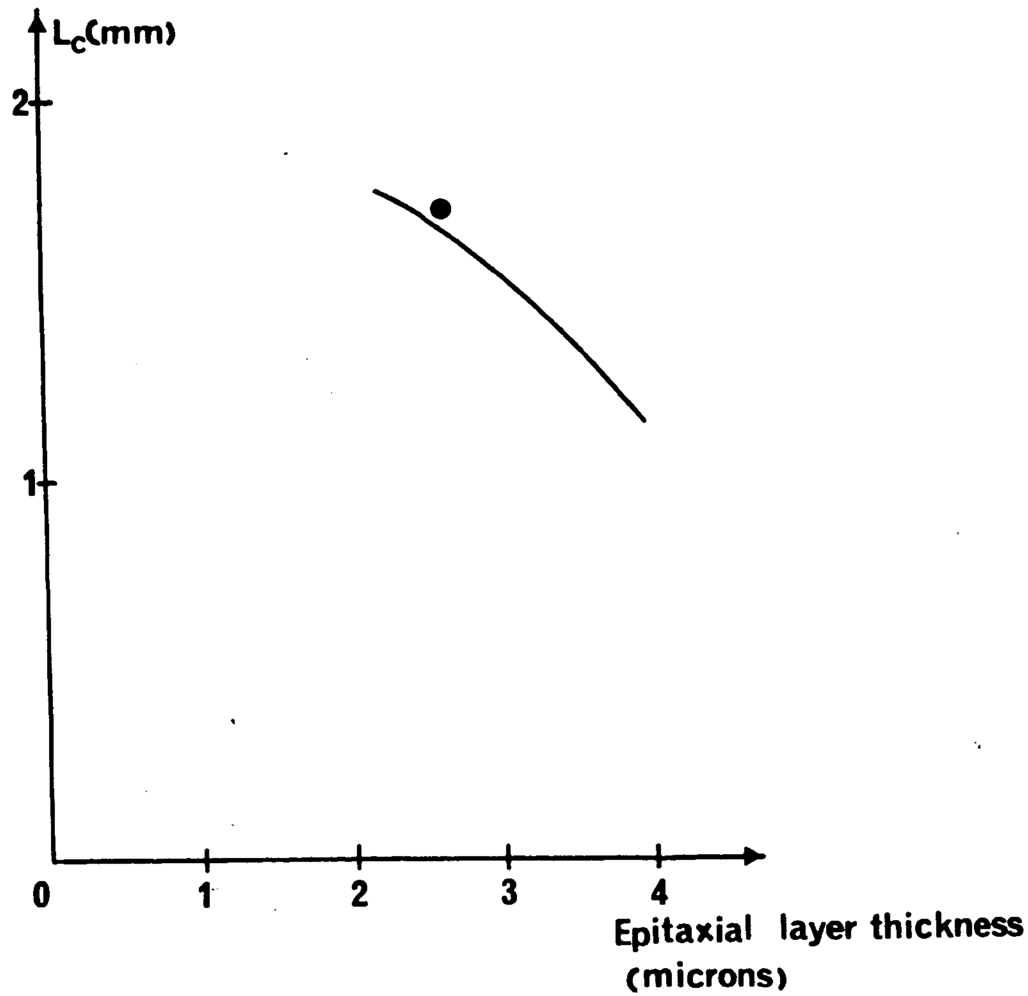

Fig.6.31 Normalised intensity profiles for (a) symmetric and (b) asymmetric modes for a 14μm wide slot with $F = 500\ Nm^{-1}$. (c) shows the normalised intensity profile resulting from adding equal amplitudes of each of these modes.

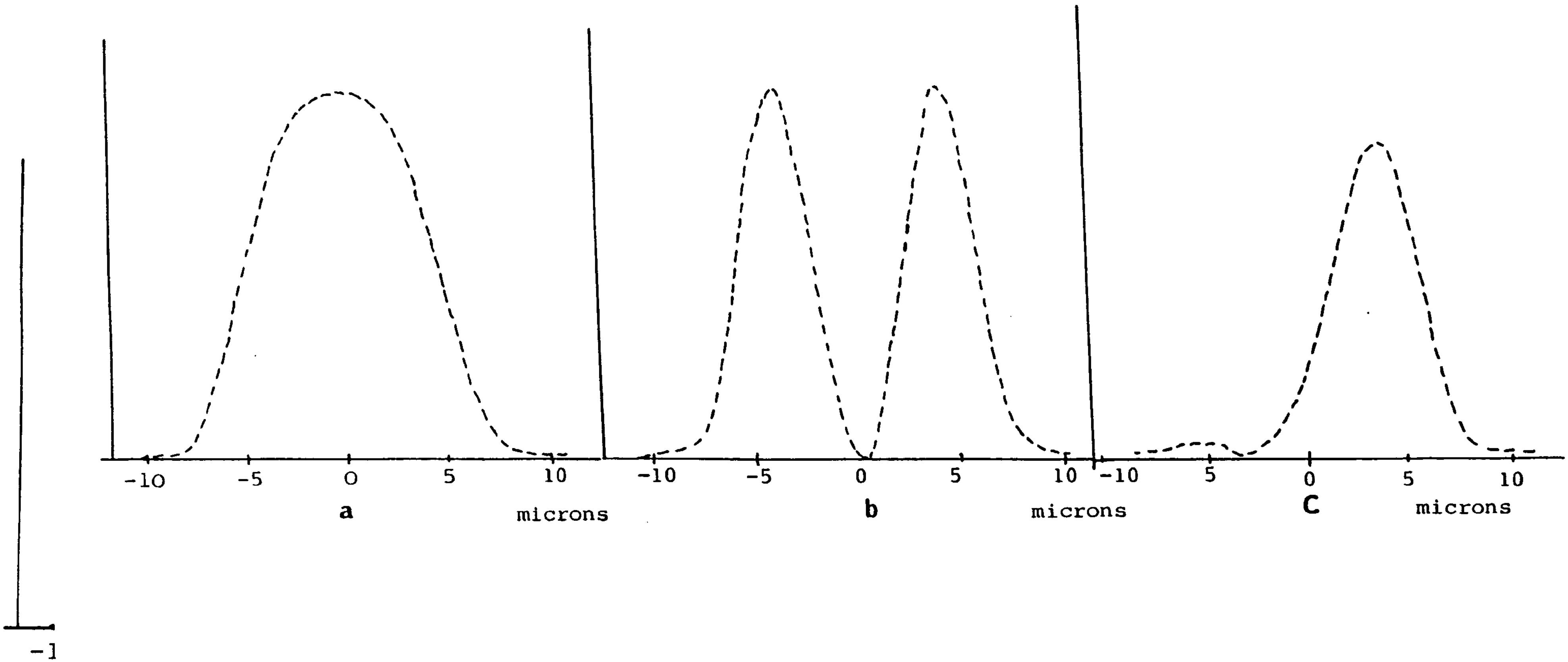

Addition of equal amplitudes of each of these modes and squaring the result gives the intensity distribution of Fig.6.31(c) confirming the experimental observation that directional-coupler like action could still be observed experimentally by careful alignment of the exciting beam. Because the directional-coupler behaviour is more distinct for larger F this outweighs other advantages of working near the minimum in the L_c/F curve of Fig.6.28.

No propagating modes of higher order could be found in the calculations for these structures.

After the metal film was removed from a slot-waveguide sample there was no evidence for lateral waveguiding. In another experiment a single-mode slot waveguide was formed in a 2μm thick gold film and a further 0.2μm of gold then deposited over the whole surface to eliminate topographic guiding effects. Waveguiding was still observed, although the attenuation of the TM polarised mode in particular appeared to increase slightly.

A 12.4μm wide slot waveguide produced in a "strain-free" aluminium film using the method of section 4.1.3 showed no lateral confinement for TE polarised waves. Slab modes were seen for excitation on either side of the slab and some interference effects similar to those described in section 6.5.2 for a "strain-free" stripe device. For TM polarised waves no slab guiding was seen except for excitation immediately under the channel when evidence was seen for very weak guiding.

6.5.4 Single-mode channel waveguides in close proximity

Results for passive directional-coupler structures with the geometry of Fig.4.3 are described in this section. The aim of the present study is to show the importance of strain-induced refractive index changes on device coupling length.

Fig.6.32 illustrates the variation of coupling length with F for two 7μm wide channel guides separated by various widths as calculated using the finite-difference technique. Fig.6.33(a),(b) shows the predicted symmetric mode intensity profiles for a 1μm central electrode for F = $1200Nm^{-1}$ and $300Nm^{-1}$ respectively. Comparing this Fig. with Fig.6.26 and Fig.6.31(a) shows the considerable difference to the profile even such a narrow electrode makes. Table 6.7 presents coupling lengths determined by the sequential cleaving method of section 6.5.3 for directional-coupler structures with wave-guide widths ∿8μm and separation 3-4μm. Coupling lengths calculated from the finite-difference method, using measured guide dimensions and a value of film stress determined from a sample placed adjacent to the device during evaporation, are shown for comparison.

In each case the separation of the guided modes was about 15μm. For excitation directly under the central thin electrode the device SS1 with F $\sim 150Nm^{-1}$ (i.e. the smallest film thickness) showed two peaks separated by ∿12μm but of lower intensity than for excitation of one or other guide. Nothing was seen at the output for similar excitation in the samples with larger values of F.

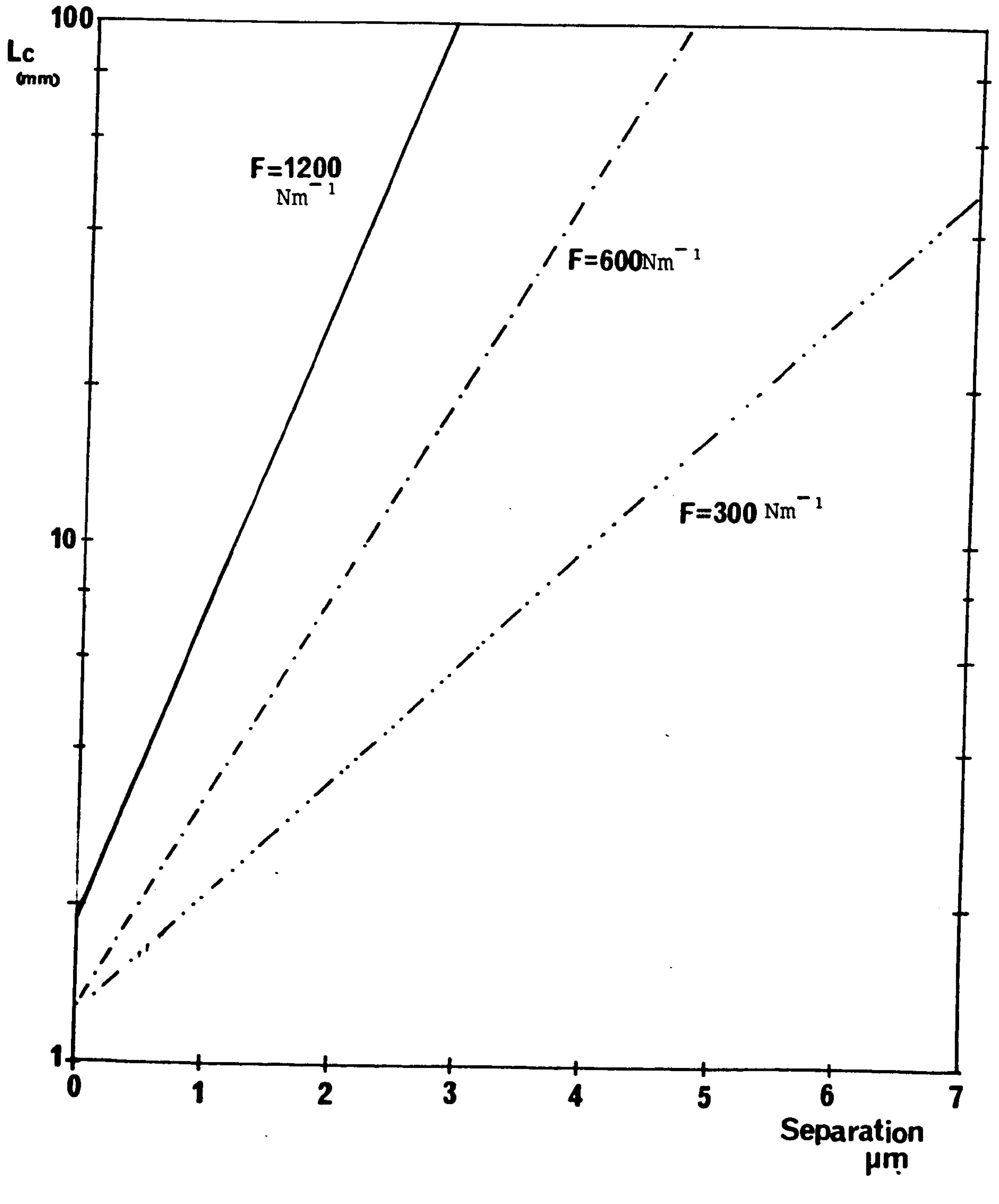

Fig.6.32 Variation of coupling length with edge separation and F for two 7μm wide channel guides.

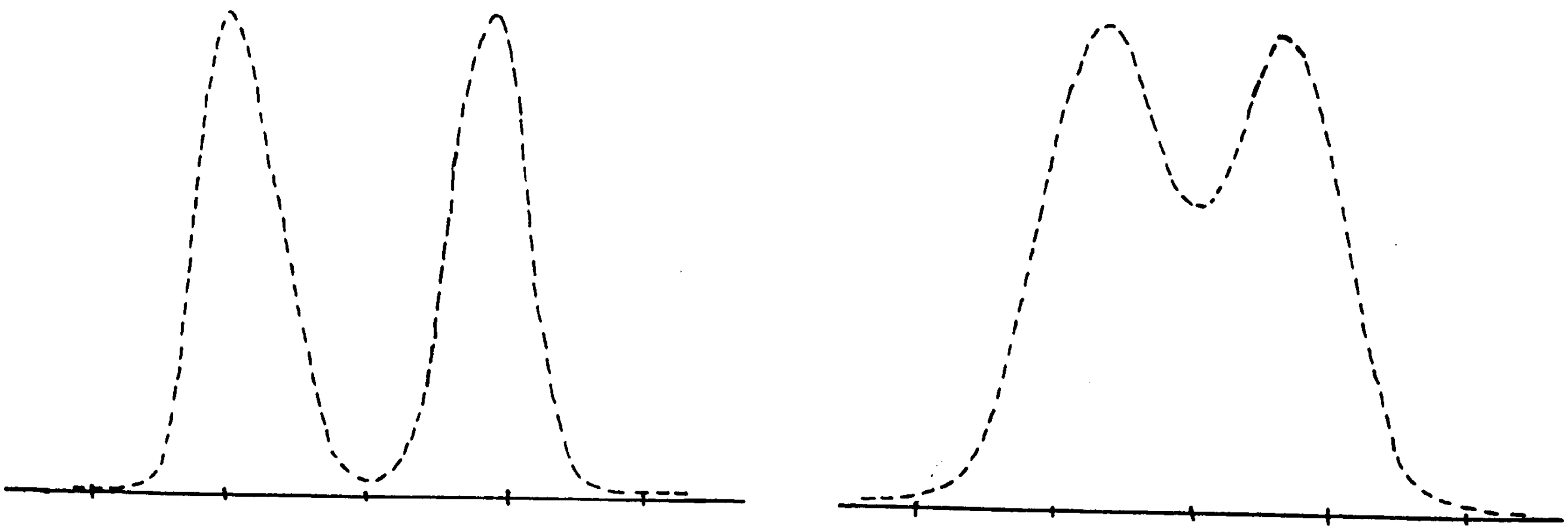

a

b

Fig.6.33 Predicted symmetric mode intensity profiles for a directional coupler structure formed by two 7μm channel waveguides separated by 1μm (a) $F = 1200Nm^{-1}$ (b) $F = 300Nm^{-1}$.

In most cases the calculated coupling length agrees well with those determined experimentally, the exception being sample SS2. For this sample, however, examination under an S.E.M. showed that the metal film thickness was greater than that of the photoresist. In devices SS3 and SS4 therefore multiple layers of photoresist were used for masking as described in section 4.1.3. The other devices show a clear trend of coupling length increasing with F indicating the importance of strain. The increase between device SS1 and devices SS3 and SS4 is not, perhaps, as marked as might be expected but is masked to a degree by a slightly smaller guide separation arising from the thicker photoresist mask used. Fig.6.34 shows the near-field intensity profiles recorded on the X-Y plotter for various lengths of device SS3 and excitation of each guide in turn.

In the small lengths of the samples remaining after the sequential cleaving to determine coupling length no change in guiding properties with time have been seen over a period of up to 3 months.

No attempt was made to switch the devices using electro-optically induced phase changes as such studies have already been reported by Campbell et al [14] and Leonberger and Bozler [20] who each quote coupling lengths which, using the curves of Fig.6.32 suggest $F \approx 300\mathrm{Nm}^{-1}$. The metal films used by these authors were electrodeposited so there is no thermal component to film stress but it is feasible that the guiding behaviour they observed was caused by refractive index changes arising from an intrinsic film-stress component [44].

Fig.6.34 Near-field intensity profiles recorded experimentally for various lengths of device SS3 and excitation of each guide in turn.

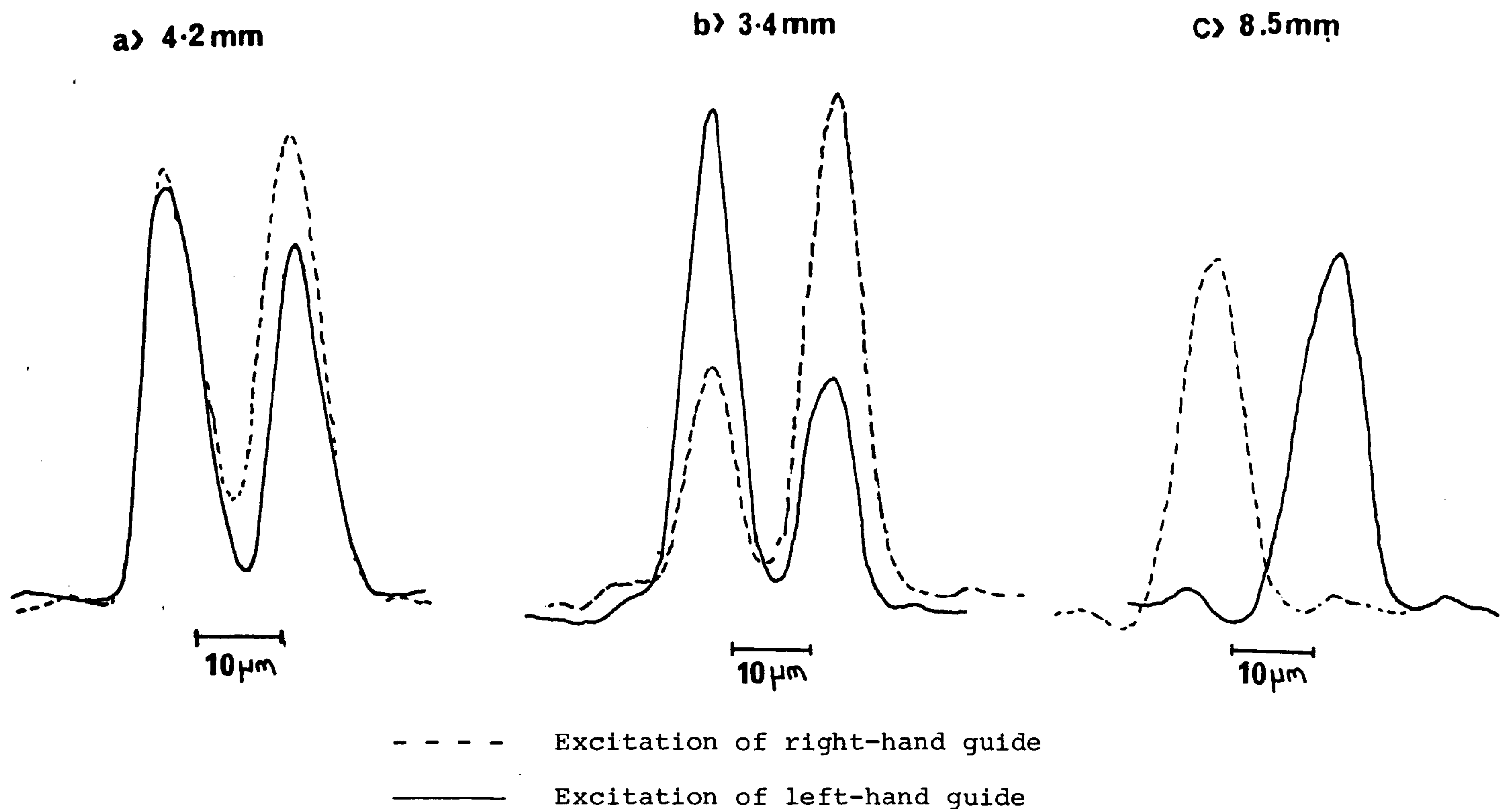

6.5.5 Evaluation of 90° waveguiding

Infra-red radiation from the laser was coupled into the input waveguide by 'end-fire' coupling, using a x45 objective lens in the usual manner. The small sample sizes meant that a similar objective could not be brought physically close enough to image the orthogonal output cleaved facet onto the Vidicon camera. A long-working distance x20 microscope objective was therefore used for this purpose. A x10 objective at the output was found to make preliminary alignment easier as it required a smaller change in position to focus the guided light after initially imaging the waveguide with white light from the back illuminator.

The effectiveness of the reflection was first evaluated by forming an etched edge on n/n^{+} GaAs material and cleaving in a position to dissect the "wall" formed. On subsequent examination slab waveguiding was observed as far as the etch only. In the vicinity of the exposed end of the edge no evidence of radiation into slab modes or other forms of loss was found, even using a high camera sensitivity.

Extra loss introduced by the reflection was estimated by producing a straight waveguide section from an adjacent piece of material using the same fabrication technique. The length of this waveguide was cleaved to match the total length of the two orthogonal guides in the bent structures. Loss measured in this way showed that for different devices between 35 and 70% of the light was reflected into the second waveguide by the etched wall. Typical etch profiles are presented in

Fig.6.35(a),(b) and show some roughness of about 0.5μm in magnitude. From an examination of waveguide structures under an S.E.M. (as for example in Fig.6.35(c)) a qualitative relationship between edge roughness near the point of reflection and loss was found. The smoothness of the etched wall is limited by the resolution of the optical photolithography used. Although the reflection technique has been successfully demonstrated it is thought that reproducibility and improvement of results will require better definition of the edge, perhaps using a combination of electron-beam lithography and dry etching.

6.6 InP Devices

6.6.1 InP Schottky diodes

This section describes measurements to verify the work of Wada [66], [67] on increased barrier height in Au/n-InP Schottky barriers incorporating an interfacial native oxide. Current-voltage (I/V) measurements were performed on 600μm diameter circular diodes fabricated on epitaxial InP slices with carrier concentration $1 \times 10^{15} cm^{-3}$. Measurements were taken either using a Tekronix 577 I-V curve tracer or an electrometer (model Keithley 602) and in the dark as the characteristics were light-sensitive. Fig.6.36 shows a typical forward-bias characteristic for an unoxidised device and a device oxidised for 10s and subsequently annealed as described in Chapter 4. Fig.6.37 shows the reverse-bias characteristics for the same devices.

The I/V results are analysed using the thermionic-emission

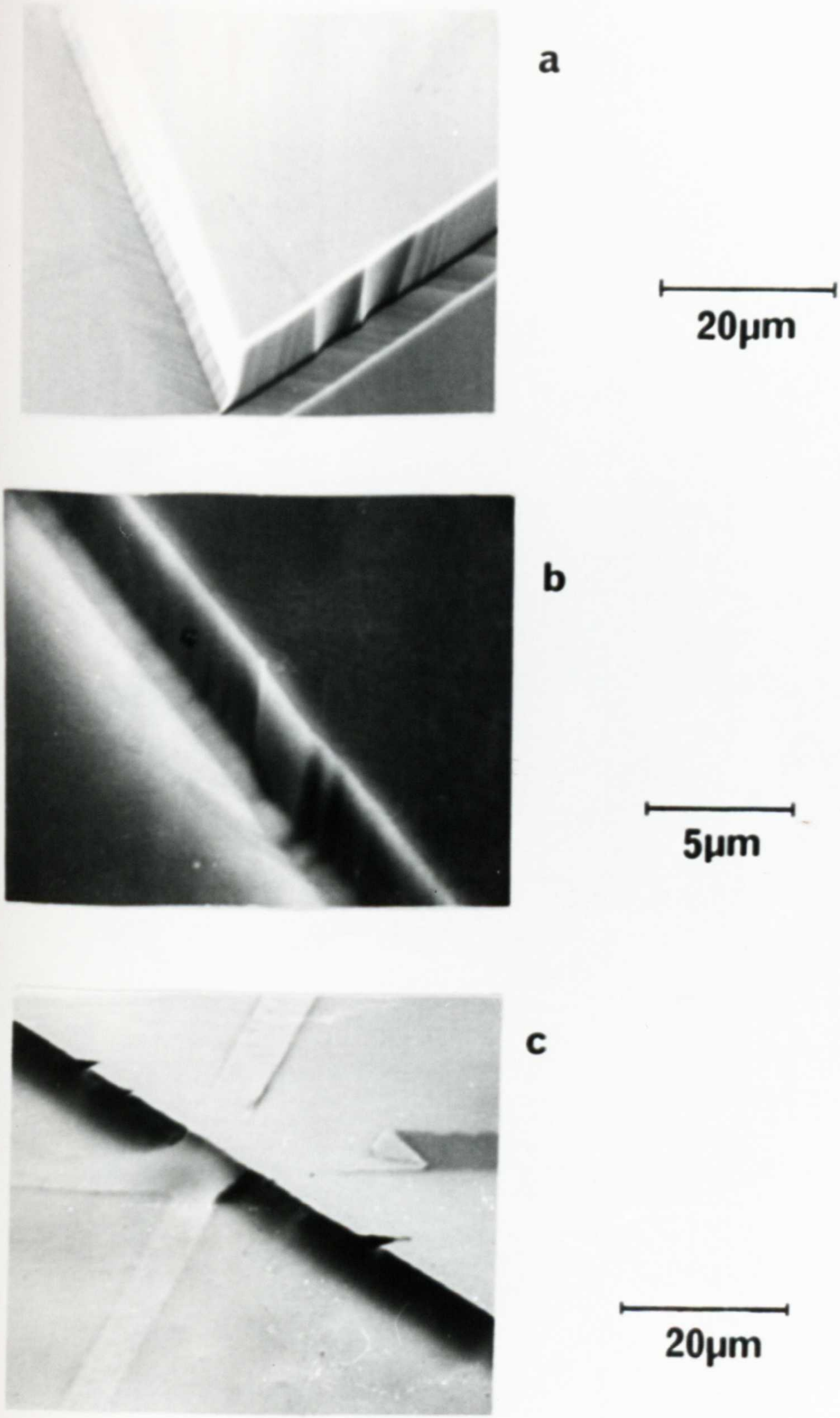

Fig.6.35 Etch wall profiles (a),(b) and waveguide structure (c) for proposed bent-waveguide structure.

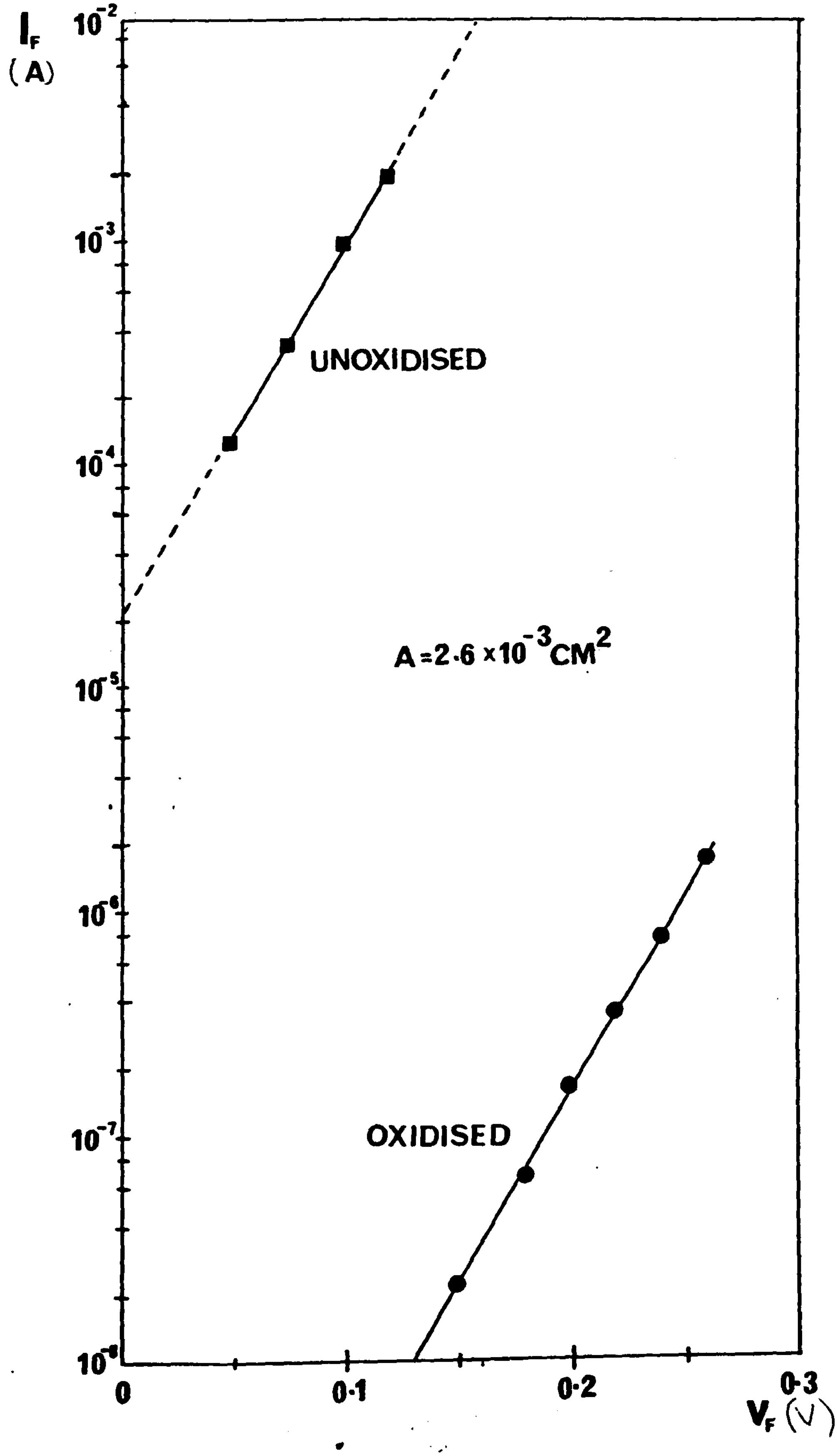

Fig.6.36 Forward I-V characteristics of unoxidised and oxidised Schottky barriers. Oxidation for 10s was followed by annealing at 250°C for 30 min.

A = area

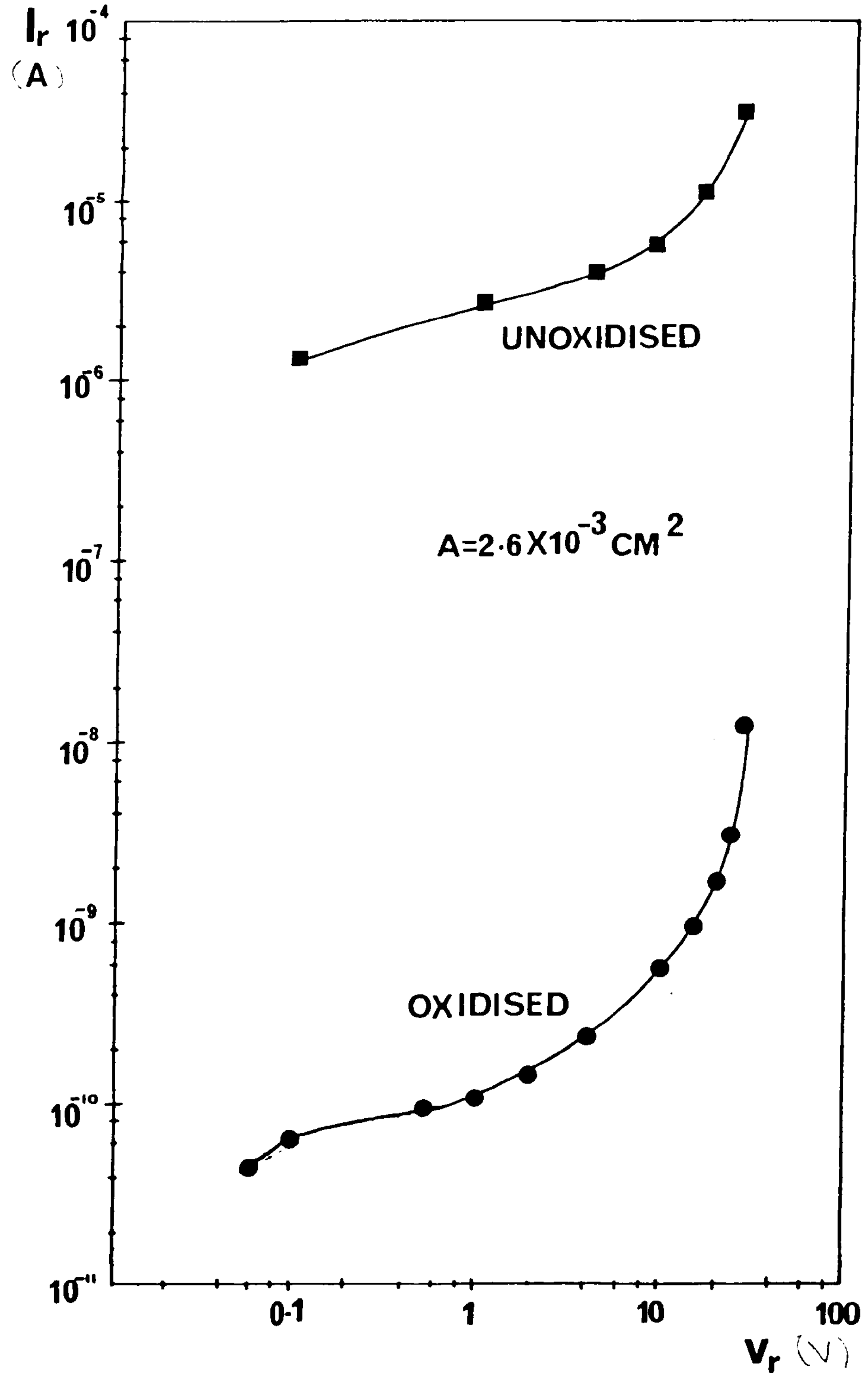

Fig.6.37 Reverse I-V characteristics for the same Schottky barriers as in Fig.6.36.

A = area

model for a Schottky barrier given by Wada as

$$J = J_s \; [\exp(\frac{eV}{n_I k_B T}) - 1] \tag{6.13}$$

where the saturation current density

$$J_s = A^{**} T^2 \exp(- \frac{e\phi_b}{k_B T}) \tag{6.14}$$

A^{**} is the effective Richardson constant, for an effective mass $m^* = 0.078\ m_e$, $A^{**} = 8.4\ \mathrm{Acm^{-2}K^{-2}}$, k_B is Boltzmann's constant, V the applied voltage, and n_I is an ideality factor which accounts for departures from the simple thermionic-emission model.

From the gradient of Fig.6.36 an ideality factor of 1.05 is obtained from (6.13) for both unoxidised and oxidised barriers. Using (6.14) barrier heights of 0.46eV (unoxidised) and 0.77eV (oxidised) are found from the current-axis intercepts. The reverse characteristics of Fig.6.37 show that due to the oxidation leakage current is reduced considerably.

The results obtained show excellent agreement with those of Wada who successfully applied a general theory of oxidised Schottky barriers incorporating the effect of fixed charges in the oxide layer to interpret his results.

A linear (capacitance C)$^{-2}$/V characteristic taken on another oxidised device confirms that the Schottky barrier behaves normally but with an increased barrier height. The technique is useful therefore for forming Schottky barrier stripes for the waveguide structures described in Chapter 4.

6.6.2 InP waveguides

6.6.2.1 Stripe structures

Schottky barrier stripe structures with various gold thicknesses and stripe widths have been studied.

A 39μm wide stripe with a 2μm gold thickness showed two very intense, well-confined- guiding regions one at each stripe edge for both TE and TM polarisations. Further a broader, less-intense guiding region could be excited directly under the stripe centre for both polarisations. Fig.6.38 shows the three TM polarised modes for this structure. The half-width measured for the centre mode is 15μm, those for the edge modes 6μm.

Both TE and TM polarised modes are guided under the Schottky barrier stripe at zero bias enabling the electro-optic interaction with the TE waves to be measured using the technique described in section 6.5.1. Fig.6.39 shows the resulting plot of $|(\beta_{TE}-\beta_{TM})|L = \Delta\beta L$ as a function of the bias voltage. Using (6.5) and (6.8) the non-zero electro-optic coefficient r_{41} of InP was found to be $(1.6 \pm 0.4) \times 10^{-12}mV^{-1}$. This is in good agreement with the value of $1.45 \times 10^{-12}mV^{-1}$ measured at 1.06μm by Tada and Suzuki [79]. The intercept on the voltage axis agrees closely with that calculated as required to deplete the epitaxial layer. It is larger than the intercept of Fig. 6.11 due to a thicker layer and a slightly higher carrier concentration.

Stripes of width 27μm and gold thicknesses of 0.3, 0.7 and 2μm also showed guiding at both stripe edges together with

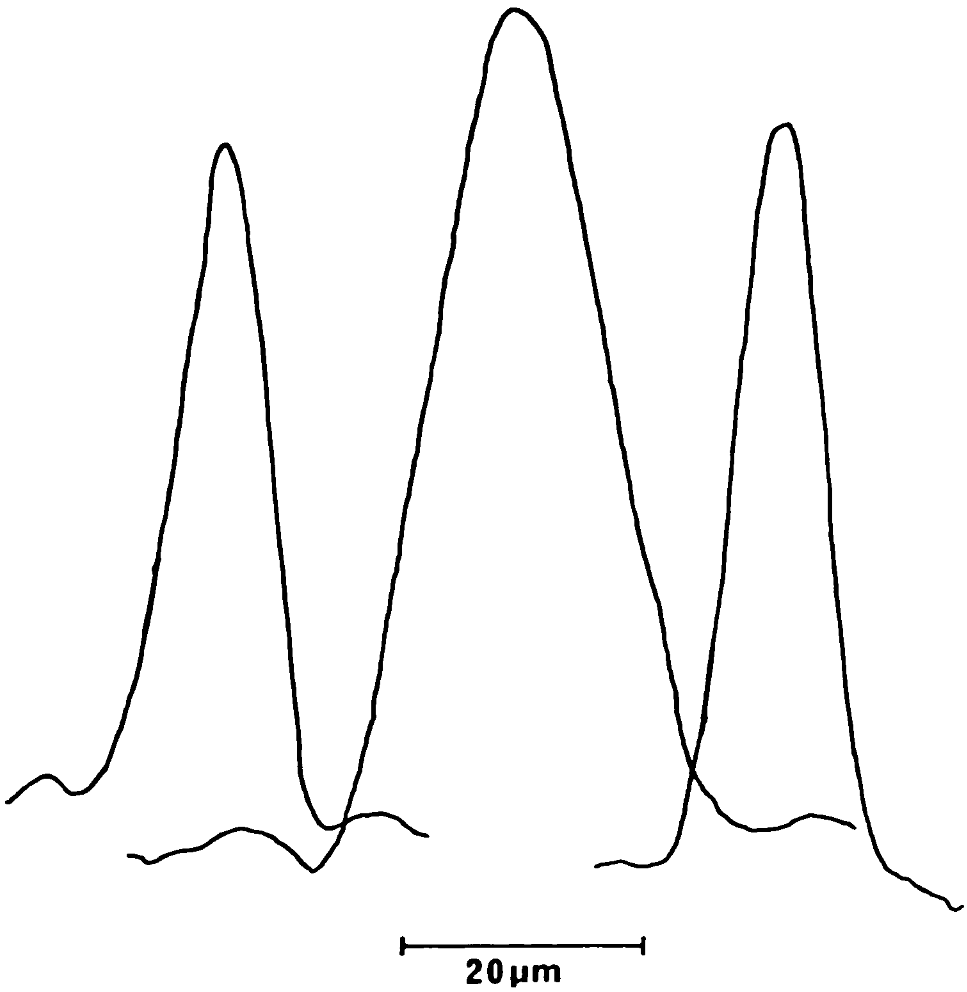

Fig.6.38 Experimental mode profiles for the three TM polarised modes supported by the photo-elastic refractive index changes from a 39μm wide gold stripe 2μm thick on n/n^+ InP.

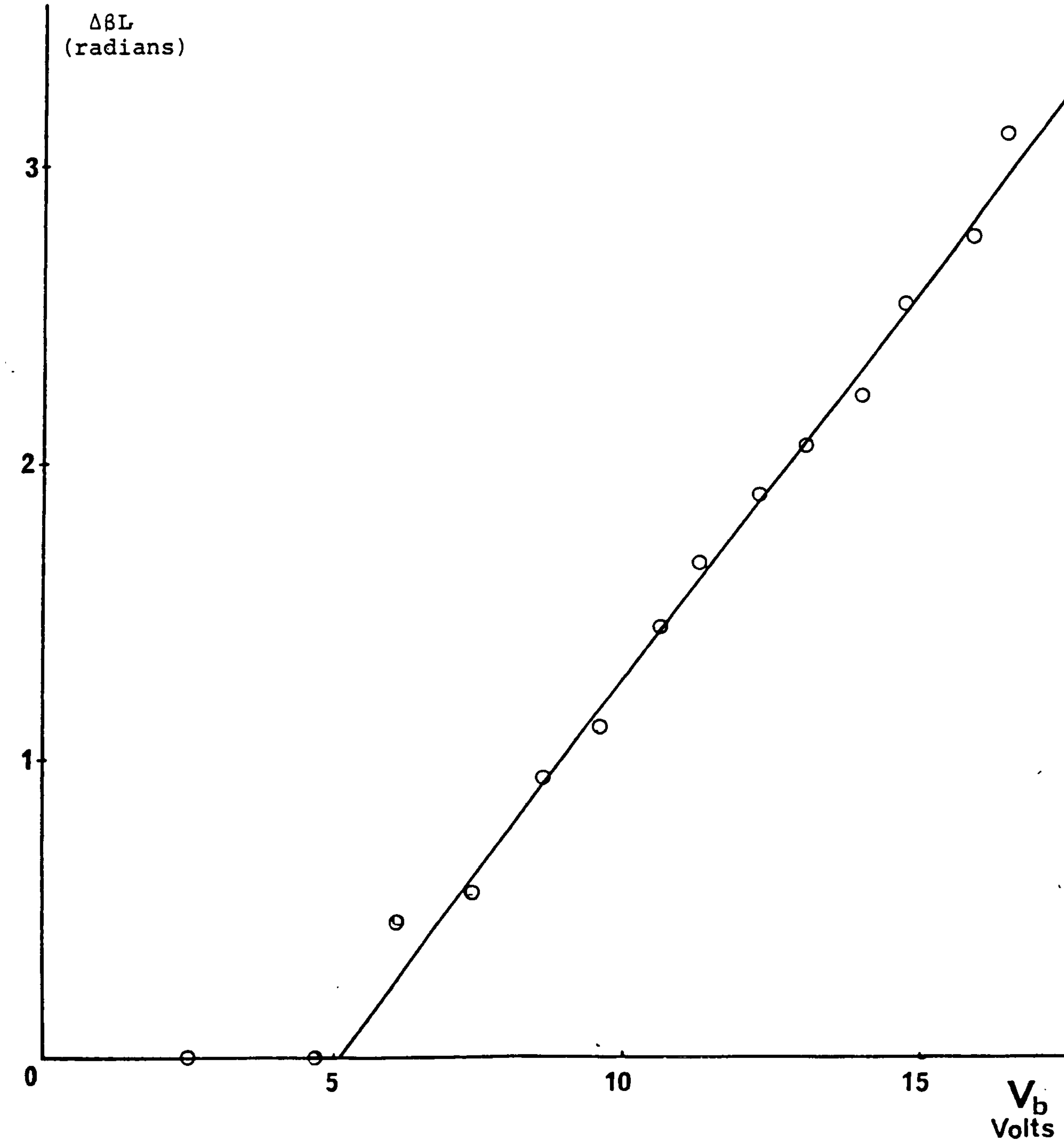

Fig.6.39 Phase modulation characteristic obtained from the interference of the TE and TM polarised centre guided modes of a 39µm wide gold stripe on n/n^+ InP.

less-intense but well-defined guiding under the stripe centre. Figs. 6.40 and 6.41 are composite pictures of the three TM polarised guided modes for the 2μm and 0.7μm gold thicknesses respectively. The ease with which the guided modes could be excited increased with gold thickness.

The results on stripe structures described so far may be explained by a positional change in $\Delta\varepsilon_r$ similar to that shown for a similar stripe on GaAs in Fig.6.13. The two edge guiding regions only were observed in 16 and 18μm stripe devices with 2μm gold thicknesses and a 24μm stripe structure with a 1μm gold film. In these cases light input under the stripe was expelled to either side probably because of the central increase in refractive index being absent or too small to support a guided mode.

A summary of the guiding properties of stripe waveguides fabricated in InP is given in Table 6.8.

6.6.2.2 Channel structures

Channels less than 10μm wide showed single-mode wave-guiding for both TE and TM polarised waves. Fig.6.42 gives the guided mode profile for the TE mode beneath a 10μm wide channel in a gold film 2μm thick. By observing the output intensity for various sample lengths progressively reduced by sequential cleaving at the output side the intensity attenuation coefficient was measured as 1.2cm^{-1}. This value is slightly larger than expected from section 6.2 but a poor quality layer (incorporating several "pin-holes") might account for this.

Channels of widths between 14μm and 18μm showed two

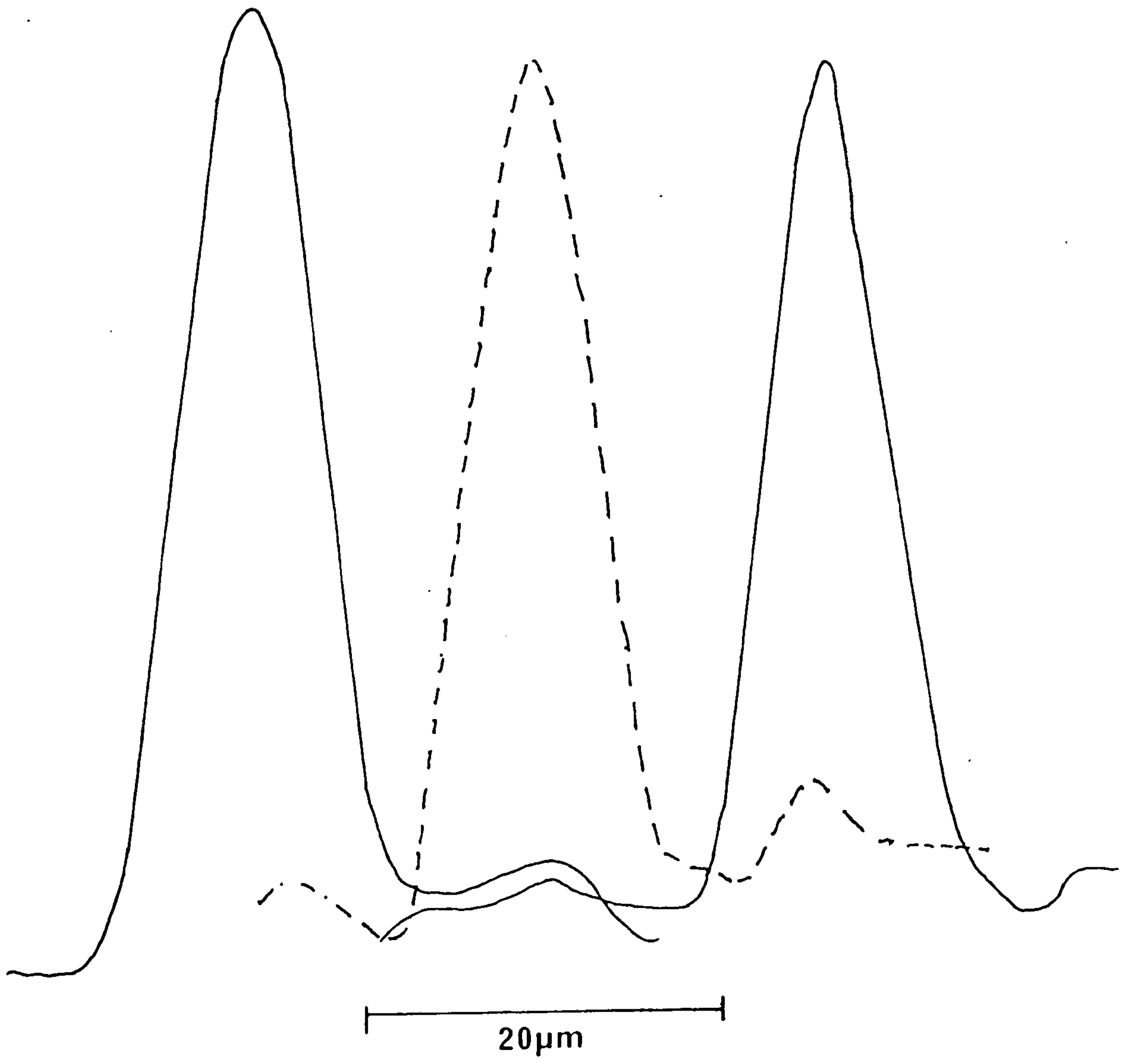

Fig.6.40 The three experimental TM modes for a 27μm wide gold stripe 2μm thick on n/n^+ InP.

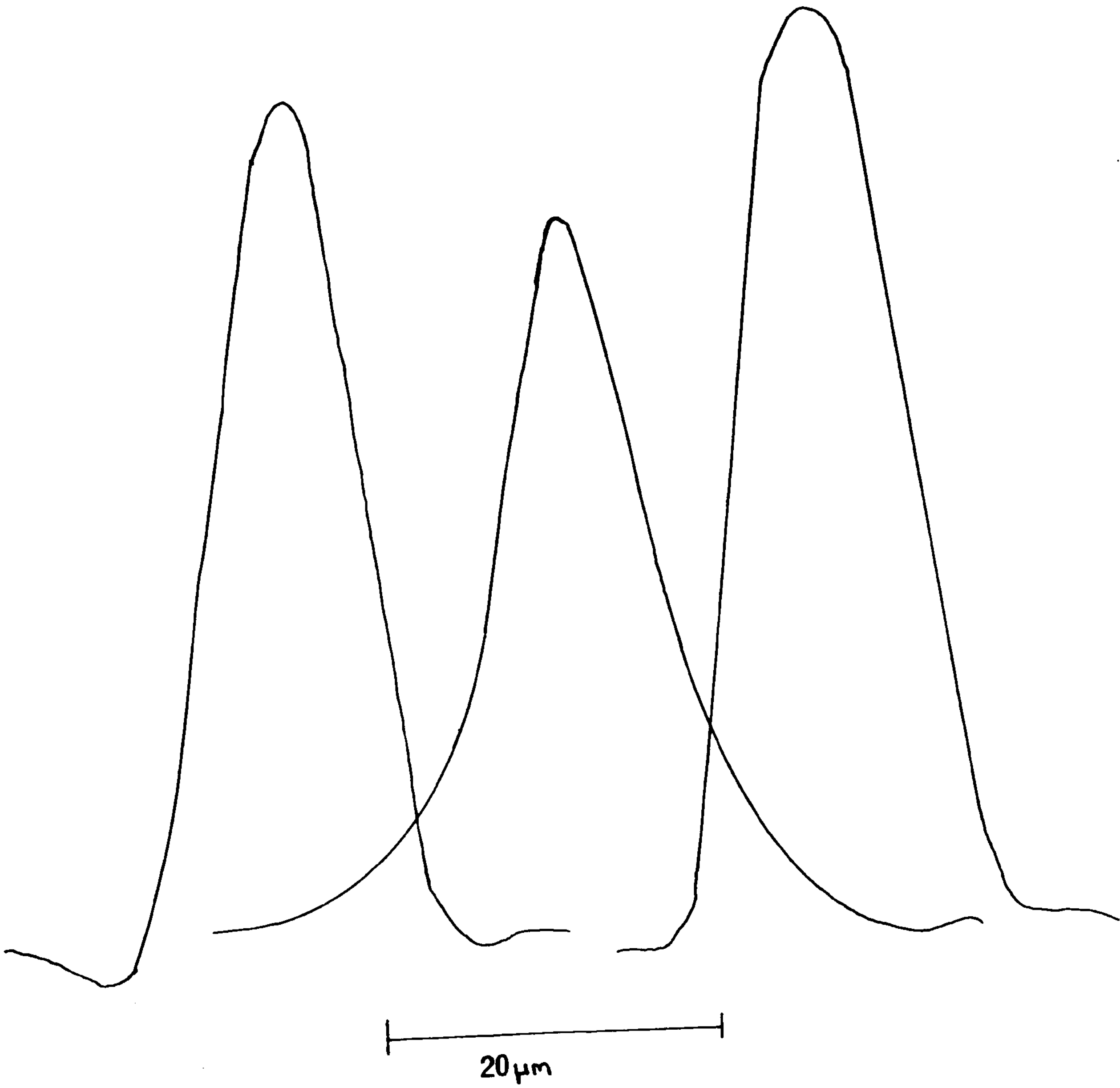

Fig.6.41 The three experimental TM mode profiles for a 27μm wide gold stripe 0.7μm thick on n/n$^+$ InP.

Fig.6.42 Guided mode profile for the TE mode beneath a 10μm wide channel in a gold film 2μm thick on n/n^+ InP.

guiding regions positioned under the channel itself. The two regions were observed simultaneously with their relative intensities dependent on the sample length. Fig.6.43(a),(b) shows intensity profiles recorded on the X-Y plotter for a 2.1mm length of a 15μm wide channel structure with a 2μm gold film. At the input cleave light was coupled into the guide on the right-hand side in Fig.6.43(a) and into that on the left-hand side in Fig.6.43(b). Fig.6.44 shows a similar profile for a 2.6mm length of the same sample with the guide on the left excited at the input cleave. The relative light intensity in the initially excited guide plotted against sample length followed closely a $\cos^2$ variation showing that, as for similar GaAs structures, a highly synchronous directional coupler is formed. A coupling length of (3.1 ± 0.4)mm consistent with the $\cos^2$ intensity variation is larger than that of (2.2 ± 0.2)mm for a similar channel in GaAs indicating confinement is tighter in InP strain-induced waveguides. If the photo-elastic coefficients are assumed the same in InP as for GaAs the increase in confinement would be explained by a smaller value of E' and a larger value of ν, calculated for InP from the data of Neuberger [60] using the method of Kirkby et al [57], and the subsequent increase in e_{xx} and e_{yy} from (3.14) and (3.15).

6.7 Strain-Induced Waveguiding With No Epitaxial Layer

It is apparent from the discussion of section 3.2 that strain-induced refractive index changes decrease rapidly with depth into the crystal as well as laterally. It is reasonable to expect that some form of strain-induced waveguiding will be

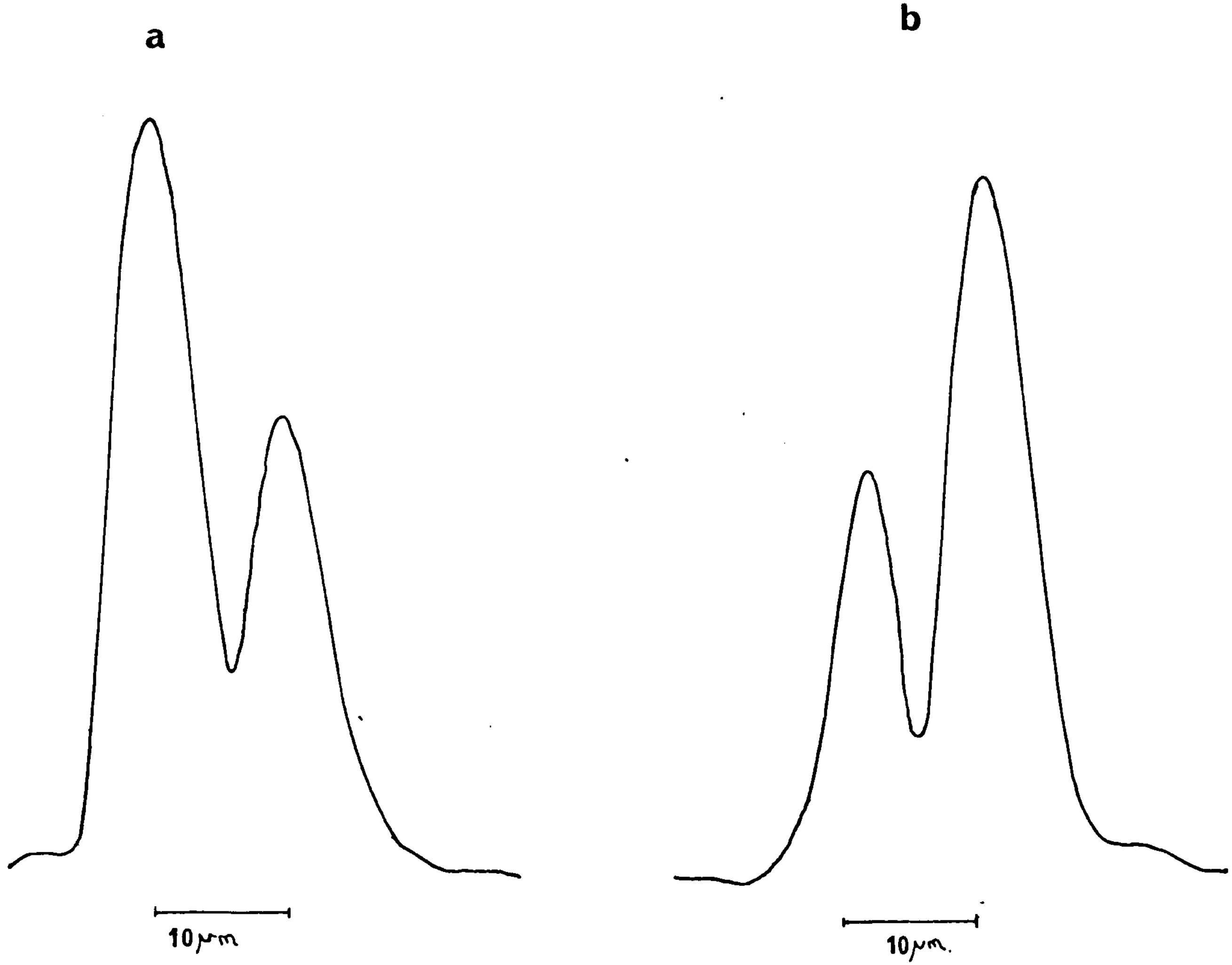

Fig.6.43 The intensity profiles for a 2.1mm length of 15μm wide channel in a 2μm gold film (a) Right hand guide excited (b) left hand guide excited at the input cleave.

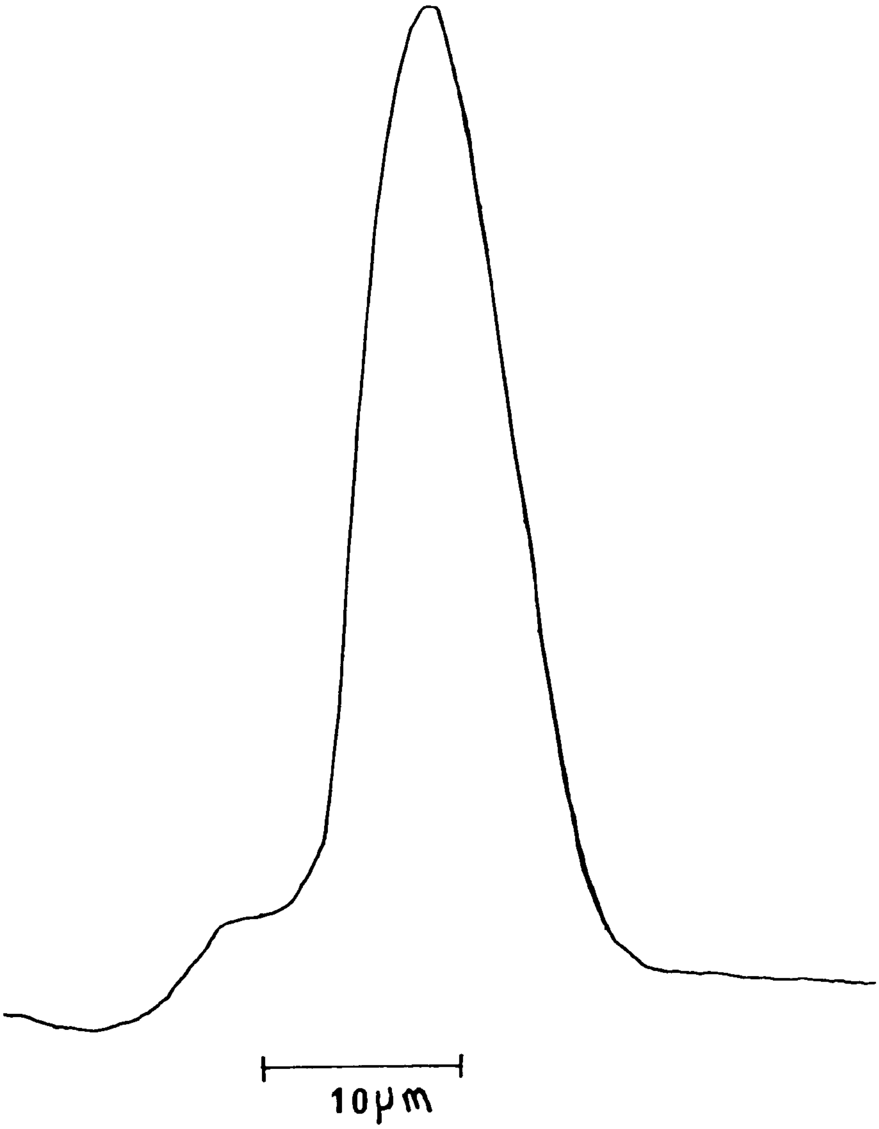

Fig.6.44 TE intensity profile for a 2.6mm length of the guide described in Fig.6.43 with the guide on the left excited at the input cleave.

present in a channel structure without the initial confinement of the epitaxial layer and this is confirmed by finite-difference calculations.

Experimentally, guiding was found in a short InP slot device with a gold thickness of 2μm but confinement was poor and there was much leakage of light into other parts of the semiconductor. The finite-difference calculations suggest that under an 8μm slot with $F = 1200\,Nm^{-1}$ most of the light should be confined in the first 10μm or so of the substrate and under the slot. By using different box depths for these calculations the guiding was shown not to be an artefact of the imposed boundary conditions.

TABLE 6.1

n_1	h (μm)	N_{eff}	Method of calculation	Finite difference boundary conditions and interval length (μm)	α (cm^{-1})
1	2.5	3.43762	Analytical	-	4.12
1×10^{-7}	2.5	3.43761	Analytical	-	4.13
Al	2.5	3.43760	Analytical	-	4.37
Au	2.5	3.43760	Analytical	-	4.29
0	2.5	3.43757	Finite Difference	Arithmetic mean 0.25	4.17
0	2.5	3.43757	Finite Difference	Arithmetic mean 0.5	4.17
0	2.5	3.43759	Finite Difference	As (6.1) 0.25	4.17
0	2.5	3.43774	Finite Difference	Larger of n's	-
0	2.5	3.43750	Finite Difference	Smaller of n's	-

Optical loss and effective refractive index calculated for a slab waveguide

TABLE 6.2

X (μm)	Y (μm)	N_S	N_A	L_C (mm)	Iterations for 6 dp
0.5	0.5	3.44230	3.442016	2.0	70
0.5	0.25	3.44229	3.44201	2.0	70
0.25	0.5	3.44253	3.44220	1.7	150
0.25	0.25	3.44253	3.44220	1.7	230
0.125	0.25	3.44268	3.44232	1.6	-

Effective indices N_S and N_A of the symmetric and asymmetric modes calculated using the finite-difference method for a 14μm wide slot waveguide with $F = 1200\,\mathrm{Nm}^{-1}$ and different mesh sizes.

TABLE 6.3

Device	Stripe Width (μm)	Stripe Thickness (μm)	Half-width, centre (μm) TE	Half-width, centre (μm) TM	Half-width Edge (μm) TE	Half-width Edge (μm) TM	Position (μm) of guides
A18YA (1978)	29	1.8	11	8.2	-	9.2	0, ±18
A18YA (June 1980)	29	1.8	12	9.6	11	9.0	0, ±18
A18YA (Nov. 1981)	29	1.8	12	9.2	-	9.0	0, ±18
A6XA (June 1978)	28	0.6	Not isolated	10	12	10-13?	0, ±17
A6XA (June 1980)	28	0.6	13	11.6	12	10	0, ±17
A6XA (Nov. 1981)	28	0.6	13	10.8	12	10	0, ±18
27AP80A	27	1-1.2	10.2	10.6	7.2	6.4	0, ±17
21FE80A5	21	1.5	10.0	10.0	7.2	6.8	0, ±13
17MA80	17	1	Not isolated	10.4	9.6	8.4	0, ±11
10FE80A6	10	0.6	Not	Seen	14	12	0, ±6
"EDGE 1"	>100	0.6	Not	Seen	7.6	7.3	-
"EDGE 2"	>100	2	Not	Seen	6	5.6	-

Summary of Guiding Properties of GaAs Stripe Waveguides

TABLE 6.4

Method of calculation	N_{eff}	$t_{\frac{1}{2}}$ (μm)
Exponential approximation	3.44033	7.1
$1/\cosh^2$ approximation	3.44019	7.3
One-dimensional finite difference	3.44077	6

Guiding Properties of an Edge Guide ($F = 360Nm^{-1}$)
Analysed at Depth 2μm by Various Methods.

TABLE 6.5

Sample Length (mm)	Percentage of Light in excited guide at Output Cleave (Experimental)	$\cos^2$ (Cz) (L_c = 2.2mm)
2.1	<5	0.01
3.4	~50	0.57
5.6	35	0.43
7.6	40	0.43
9	95	0.98

Experimentally determined light intensity in the initially excited guide for various lengths of a 15μm channel waveguide and proposed $\cos^2$ variation

TABLE 6.6

Slot Width (μm)	F (Nm^{-1})	L_c (mm)	Method of Finding L_c	Comment
14	1200	1.65	Fitting of biased waveguide data	See Figs. 6.20 and 6.21
15	1200	2.2 ± 0.2	Sequential cleaving	See Table 6.5
15	1200	2.4	Fitting of biased waveguide data	See Figs. 6.16 and 6.17
15	1200	2.3		See Figs. 6.18 and 6.19
16	1200	3.4	Sequential cleaving	Fit to only four experimental points
22	600	4.9	Fitting biased waveguide data	Sample length 3.9mm. Normal Δβ bias only

Experimental coupling lengths for various slot Directional Couplers

TABLE 6.7

Sample	F_{-} (Nm^{-1})	Experimental Coupling length (mm)	Calculated Coupling length (mm)
SS1	150	5.6 ± 1	4.2
SS2	600	6.6 - 9.6	∿20
SS3	450	8.7	6.6 - 8.8
SS4	325	6	6-7

Experimental and Calculated coupling lengths for directional-coupler structures formed by two single-mode channel waveguides in close proximity

TABLE 6.8

Stripe width (μm)	Gold thickness (μm)	Centre guiding Region Half-width (μm)		Edge mode half-width (μm)		Position of Guides (μm)
		TE	TM	TE	TM	
16	2	Not	Seen	7.2	7.0	0, ±10
17.5	2	Not	Seen	7.4	6.8	0, ±10
24	1	Not	Seen	8.0	7.7	0, ±14
27	0.3	Not separable	12	Not separable	10.4	0, ±15
27	0.7	12	10.8	12	9.6-10.8	0, ±15
27	2	9.2	8.4	7.8	7.8	0, ±15
39	2	17	15	6.0	6.0	0, ±22

Summary of the Guiding Properties of InP Stripe Waveguides

CHAPTER 7

CONCLUSIONS

It has been demonstrated that optical waveguides may be produced in both GaAs and InP epitaxial layers through the photo-elastic effect. Such waveguides have been exploited to produce a novel directional-coupler structure for integrated optics with the advantages of high phase synchronism and a short coupling length ($\sim$ 2mm) without rigid tolerances on the fabrication process. By applying reverse-bias in suitable configurations one of these directional couplers could be switched to give either the straight-through or the crossed-over state at the device output. The capacitance of each electrode was $\sim$2pF per mm. corresponding to a 3dB bandwidth of 1.6GHz with a 50Ω line system for a 2mm long coupler. This bandwidth could be improved by reducing the electrode width thereby lowering capacitance. However, to ensure guiding properties under the channel are not affected by strain-induced refractive index changes arising from the remote metal edges, an electrode width of at least 15μm is needed. The Schottky diode structure of Fig.4.2 can be used as a microwave strip-line. Ono [80] proposed a modulator, based on the novel directional coupler structure described, in which a microwave modulation signal propagates along the line together with the light wave. The proposed structure allows for an increase in operation frequency above the limit imposed by the time-constant of the diode.

A new method of analysing electromagnetic wave propagation in waveguides where refractive index may vary in both directions of the cross-section but is constant in the longitudinal direction has been developed. Using this method of calculation, which is based on finite-difference techniques, experimental results in GaAs have successfully been described in terms of the strain-induced refractive index changes. The importance of strain in directional-coupler structures formed by having two "metal-gap" guides in close proximity has also been demonstrated both experimentally and theoretically.

In InP epitaxial layers similar strain-induced waveguiding has been observed experimentally. Although refractive index changes cannot be calculated the experimental results indicate that these are slightly bigger than in GaAs, possibly as a result of larger strains due to a smaller Young's modulus and a larger Poisson's ratio in InP. By applying electrical bias to a Schottky metal stripe under which a guided wave with equal amplitudes of the TE and TM polarised modes propagates the non-zero electro-optic coefficient r_{41} of InP was successfully measured. This was the second measurement of this coefficient in the world and the first using this technique.

Strain-free devices have been fabricated by evaporating aluminium films onto cooled substrates and confirm that the dominant lateral-guiding mechanism is strain-induced refractive index changes. This technique might be useful for eliminating strain-effects in other devices incorporating evaporated films.

A proposed method for forming bends in waveguides by reflection off an etched vertical wall has been shown to be practicable, although different masking and etching techniques, possibly using electron beam lithography are required if the negligible loss predicted theoretically is to be achieved.

The ease of fabrication of all these strain-induced waveguides makes them ideal for producing other devices, for example Y junctions and Mach Zehnder interferometers could be made using strain-induced waveguides with suitable electrode geometries. Further work is required to understand more fully the nature of the stress in evaporated metal films. These studies should include an examination of the film structure during growth and on subsequent cooling.

CHAPTER 8

REFERENCES

[1] I.G.A. Davies, A.R. Goodwin, P.A. Kirkby and R.F. Murison: "Semiconductor Light Sources", Electrical Communication (The Technical Journal of I.T.T.) 56, 338, 1981.

[2] A.C. Carter :"Active Components for Long Wavelength Fibre Optic Systems", Allen Clark Research Centre, (Plessey), Annual Review 1981 (page 48).

[3] J.E. Goell and R.D. Standley :"Sputtered Glass Waveguide for Integrated Optical Circuits", Bell Syst. Tech.J. 48, 3445, 1969.

[4] A.R. Billings :"Integrated Optics in Later Generation Optical Communication Systems", Proc. IREE Aust., 137, 1979.

[5] S. Shimada :"Fully-Engineered and Non-Repeatered Fibre Optic Inter-Office Transmission Systems", Technical Digest of 6th E.C.O.C. (York), 427, 1980.

[6] R. Bouillie, R. Auffret and G. Le Noane :"Tuileries-Philippe Auguste : The First Operational Junction Line in France" Technical Digest of 7th E.C.O.C. (Copenhagen), 15.3, 1981.

[7] C.J. Lilly and D.R. Bissell :"Some initial Results and Experience of Operational Optical Fibre Systems in the U.K.", Technical Digest of 7th E.C.O.C. (Copenhagen), 15.4, 1981.

[8] H.J.M. Otten :"Fibre-optic Communications", Electronic Components and Applications, 3, 87, 1981.

[9] D.H. Newman :"Devices for Fibre Systems", New Electronics, 55, 1982.

[10] T. Kimura :"Single-mode Systems and Components for Long Wavelengths", IEEE Trans. Circuits Syst. CAS-26, 987, 1979.

[11] R.C. Alferness :"Guided-Wave Devices for Optical Fibre Communications", 1st European Conference on Integrated Optics, 46, 1981.

[12] F.K. Reinhart, W.R. Sinclair, R.A. Logan :"Simple Heterostructure $As_xGa_{1-x}As$ Phase Modulator with SnO_2-Doped In_2O_3 Cladding Layer", Appl. Phys. Lett. 29, 21, 1976.

[13] M. Papuchon, Y. Combemale, X. Mathieu, D.B. Ostrowsky, L. Reiber, A.M. Roy, B. Sejourne and M. Werner :"Electrically Switched Optical Directional Coupler: Cobra", Appl. Phys. Lett., 27, 289, 1975.

[14] J.C. Campbell, F.A. Blum, D.W. Shaw and K.L. Lawley : "GaAs Electro-optic Directional-Coupler Switch", Appl. Phys. Lett., 27, 202, 1975.

[15] A. Carenco, L. Menigaux, F. Alexandre, M. Abdalla and A. Brenac :"Directional-Coupler Switch in Molecular-Beam Epitaxy GaAs", Appl. Phys. Lett., 34, 755, 1979.

[16] J.C. Shelton, F.K. Reinhart and R.A. Logan :"Rib Waveguide Switches with M.O.S. Electro-optic Control for Monolithic Integrated Optics in GaAs-$Al_xGa_{1-x}As$", Appl. Opt., 17, 2548, 1978.

[17] F.J. Leonberger, J.P. Donnelly and C.O. Bozler :"GaAs $p^+n^-n^+$ Directional-Coupler Switch", Appl. Phys. Lett., 29, 652, 1976.

[18] H. Kogelnik and R.V. Schmidt :"Switched Directional Couplers with Alternating $\Delta\beta$", IEEE J. Quantum Electronics QE-12, 396, 1976.

[19] R.V. Schmidt and H. Kogelnik :"Electro-Optically Switched Coupler with Stepped $\Delta\beta$ Reversal Using Ti-Diffused $LiNbO_3$ Waveguides", Appl. Phys. Lett., 28, 503, 1976.

[20] F.J. Leonberger and C.O. Bozler :"GaAs Directional-Coupler Switch with Stepped $\Delta\beta$ Reversal", Appl. Phys. Lett., 31, 223, 1977.

[21] G.E. Stillman, C.M. Wolfe, C.O. Bozler and J.A. Rossi :"Electroabsorption in GaAs and Its Application to Waveguide Detectors and Modulators", Appl. Phys. Lett., 28, 544, 1976.

[22] H. Sasaki and I. Anderson :"Theoretical and Experimental Studies on Active Y-Junctions in Optical Waveguides", IEEE J. Quantum Electronics, QE-14, 883, 1978.

[23] P.J.R. Laybourn and J. Lamb :"Integrated Optics : A Tutorial Review", Radio and Electronic Engineer, 51, 397, 1981.

[24] L.D. Westbrook :"Strain-Induced Optical Waveguiding in Epitaxial GaAs Layers", Ph.D. Thesis, University of Sheffield, 1979.

[25] E. Garmire :"Semiconductor Components for Monolithic Applications" in "Integrated Optics", ed. T. Tamir, Springer-Verlag, Second Edition 1979.

[26] H. Kogelnik :"Theory of Dielectric Waveguides" in "Integrated Optics", ed. T. Tamir, Springer-Verlag, Second Edition 1979.

[27] J.E. Goell :"A Circular-Harmonic Computer Analysis of Dielectric Rectangular Waveguides", Bell Syst. Tech. J. 48, 2133, 1969.

[28] E.A.J. Marcatili :"Dielectric Rectangular Waveguide and Directional Coupler for Integrated Optics", Bell Syst. Tech. J. 48, 2071, 1969.

[29] R.M. Knox and P.P. Toulios :"Integrated Circuits for the Millimetre Through-Optical Frequency Range". Proc. MRI Symposium on Submillimetre Waves (ed. J. Fox), Polytechnic Press, Brooklyn, 1970.

[30] H. Furuta, H. Noda and A. Ihaya :"Novel Optical Wave-guide for Integrated Optics", Appl. Opt. 13, 322, 1974.

[31] Y. Yamamoto, T. Kamiya and H. Yanai :"Propagation Characteristics of a Partially Metal-Clad Optical Guide Metal-Clad Optical Strip Line", Appl. Opt., 14, 322, 1975.

[32] T. Itoh :"Inverted Strip Dielectric Waveguide for Millimetre-Wave Integrated Circuits", IEEE Trans. Microwave Theory and Techniques, MTT-24, 821, 1976.

[33] W. McLevige, T. Itoh and R.Mittra :"New Waveguide Structures for Millimetre-Wave and Optical Integrated Circuits", IEEE Trans. Microwave Theory and Techniques, MTT-23, 788, 1975.

[34] J. Hamasaki and K. Nosu :"A Partially Metal-Clad-Dielectric-Slab Waveguide for Integrated Optics", IEEE J. Quantum Electronics QE-10, 822, 1974.

[35] J. Buus :"The Effective Index Method and Its Application to Semiconductor Lasers", IEEE J. Quantum Electronics, QE-18, 1083, 1982.

[36] J.K. Butler and J.B. Delaney :"A Rigorous Boundary Value Solution For the Lateral Modes of Stripe Geometry Injection Lasers", IEEE J. Quantum Electronics QE-14, 507, 1978.

[37] R.W. Hornbeck :"Numerical Methods", Quantum Publishers, 1975.

[38] G. Forsythe and W.R. Wasow :"Finite-Difference Methods For Partial Differential Equations", J. Wiley and Sons, 1959.

[39] J.B. Davies and C.A. Muilwyk :"Numerical Solution of Uniform Hollow Waveguides With Boundaries of Arbitrary Shape", Proc. IEEE 113, 277, 1966.

[40] D.H. Sinnott :"The Computation of Waveguide Fields and Cut-off Frequencies Using Finite Difference Techniques", Weapons Research Est., Australia, Technical Note PAD158, 1969.

[41] D.H. Sinnott, G.K. Cambrell, C. Carson and H.E. Green :"The Finite Difference Solution of Microwave Circuit Problems", IEEE Trans. Microwave Theory and Techniques, MTT-17, 464, 1969.

[42] B.A. Carré :"The Determination of the Optimum Accelerating Factor for Successive Over-Relaxation", Computer J, 4, 73, 1961.

[43] D. Marcuse :"Light Transmission Optics", Van Nostrand, 1972.

[44] R.W. Hoffman :"Mechanical Properties of Thin Films", in "Thin Films" American Society of Metals, 1964.

[45] J.D. Wilcock :"Stress in Thin Films", Ph.D. Thesis, Imperial College, University of London, 1967.

[46] R.M. Tennent :"Science Data Book", Oliver and Boyd, 1974.

[47] R. Feder and T. Light :"Precision Thermal Expansion Measurements of Semi-Insulating GaAs", J. Appl. Phys. 39, 4870, 1968.

[48] R.W. Hoffman :"The Mechanical Properties of Thin Condensed Films", Phys. of Thin Films, 3, 211, 1966.

[49] A. Brenner and S. Senderoff :"Calculation of Stress in Electrodeposits from the Curvature of a Plated Strip", J. Res. Natl. Bur. Std., 42, 105, 1949.

[50] H.P. Murbach and H. Wilman :"The Origin of Stress in Metal Layers Condensed from the Vapour in High Vacuum", Proc. Phys. Soc., B66, 905, 1953.

[51] C.W. Haworth : Department of Metallurgy, University of Sheffield, Private Communication.

[52] C.A. Neugebauer :"Tensile Properties of Thin, Evaporated Gold Films", J. Appl. Phys., 31, 1096, 196.

[53] C.J. Madams, D.V. Morgan and M.J. Howes :"Out migration of Gallium from Au-GaAs Interfaces", Elec. Lett., 11, 574, 1975.

[54] A. Durelli, E. Phillips and C. Tsao :"Analysis of Stress and Strain", McGraw-Hill, 1958.

[55] E. Volterra and J. Gaines :"Advanced Strength of Materials", Prentice-Hall, 1971.

[56] J.F. Nye :"Physical Properties of Crystals", Oxford, 1957.

[57] P.A. Kirkby, P.R. Selway and L.D. Westbrook :"Photo-elastic Waveguides and their Effect on Stripe-Geometry GaAs/$Ga_{1-x}Al_xAs$ Lasers", J. Appl. Phys., 50, 4567, 1979.

[58] R.W. Dixon :"Photoelastic Properties of Selected Materials and Their Relevance for Applications to Acoustic Light Modulators and Scanners", J. Appl. Phys., 38, 5149, 1967.

[59] F. Canal, M. Grimsditch and M. Cardona :"Piezobirefringence in GaP and InP", Solid State Comm., 29, 523, 1979.

[60] M. Neuberger :"Handbook of Electronic Materials Vol.2, III-V Semiconducting Compounds", Plenum, 1971.

[61] A. Feldman and D. Horowitz :"Dispersion of the Piezo-birefringence of GaAs", J. Appl. Phys. 39, 5597, 1968.

[62] A.C. Adams and B.R. Pruniaux :"Gallium Arsenide Surface Film Evaluation by Ellipsometry and its Effect on Schottky Barriers", J. Electrochem. Soc., 120, 408, 1973.

[63] E.A.J. Marcatili :"Bends in Optical Dielectric Guides", Bell Syst. Tech. J. 48, 2103, 1969.

[64] M. Otsubo, T. Oda, H. Kumabe and H. Miki :"Preferential Etching of GaAs Through Photoresist Masks", J. Electrochem. Soc., 123, 676, 1976.

[65] S. Iida and K. Ito :"Selective Etching of Gallium Arsenide Crystals in H_2SO_4-H_2O_2-H_2O System", J. Electrochem. Soc., 118, 768, 1971.

[66] O. Wada :"Junctions, Barrier and Traps in InP", Ph.D. Thesis, University of Sheffield, 1979.

[67] O. Wada and A. Majerfeld :"Low Leakage Nearly Ideal Schottky Barriers to n-InP", Elect. Lett., 14, 125, 1978.

[68] M.W. Austin : British Telecom Research Labs., Martlesham Heath. Private Communication.

[69] D.N. Macfadyen :"Components for Gallium Arsenide Integrated Optics Fabricated by Wet Chemical Etching", Ph.D. Thesis, University of Glasgow, 1980.

[70] W.P. Dumke, M.R. Lorenz and G.D. Pettit :"Intra- and Interband Free-Carrier Absorption and the Fundamental Absorption Edge in n-Type InP", Phys. Rev. B1, 4668, 1970.

[71] W.G. Spitzer and J.M. Whelan :"Infrared Absorption and Electron Effective Mass in n-Type Gallium Arsenide", Phys. Rev. 114, 59, 1959.

[72] E.P. Rashevskeya and V.I. Fistul :"Infra-red Absorption of GaAs Doped with Group VI Impurities", Sov. Phys. Solid State, 9, 2849, 1968.

[73] C.F. Buhrer, L.R. Bloom and D.H. Baird :"Electro-Optic Light Modulation with Cubic Crystals", Appl. Opt.3, 839, 1963.

[74] D.E. Gray ed. :"American Institute of Physics Handbook", McGraw-Hill, 3rd Edition, 1972.

[75] E.M. Conwell :"Modes in Optical Waveguides Formed by Diffusion", Appl. Phys. Lett., 23, 328, 1973.

[76] R.J. Elliott and A.F. Gibson :"An Introduction to Solid State Physics and its Applications", Macmillan, 1976.

[77] L.J. Du and C-L Chen :"Stepped Switched Optical Directional Couplers with Unequal Section Lengths", SPIE, 176, 36, 1979.

[78] F.J. Leonberger, J.P. Donnelly and C.O. Bozler :"Wave-length Dependence of GaAs Directional Couplers and Electro-optic Switches", Appl. Opt., 17, 2250, 1978.

[79] K, Tada and N. Suzuki :"Linear Electro-optic Properties of InP", Jap. J. Appl. Phys., 19, 2295, 1980.

[80] S. Ono : Internal Report, University of Sheffield, Department of Electronic & Electrical Engineering, 1981.

[81] G. Stephenson :"Mathematical Methods for Science Students", Longman, 2nd Edition, 1973.

[82] H-G Unger :"Planar Optical Waveguides and Fibres", Clarendon Press, 1st Edition, 1977.

CHAPTER 9

APPENDICES

9.1 Reflection of Plane Waves at Plane Interfaces

Consider a ray of light incident on the general boundary between two regions with refractive indices n_1 and n_2 at an angle θ_1 to the normal. Let E_i, E_t and E_r be the electric field amplitudes of incident, transmitted and reflected rays and H_i, H_t, H_r the corresponding magnetic field amplitudes.

TE Polarisation

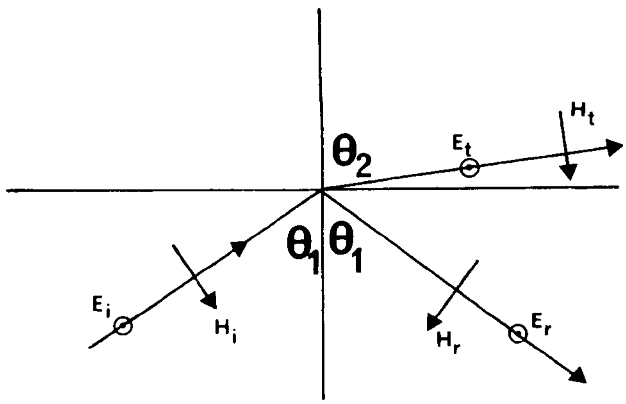

Matching E components :

$$(E_i + E_r) = E_t \tag{9.1}$$

Matching tangential H :

$$H_i \cos\theta_1 - H_r \cos\theta_1 = H_t \cos\theta_2 \tag{9.2}$$

Also

$$\frac{E_i}{H_i} = \frac{\eta_0}{n_1} \tag{9.3}$$

and

$$\frac{E_t}{H_t} = \frac{\eta_0}{n_2} \tag{9.4}$$

where

$$\eta_0 = \sqrt{\mu_0/\varepsilon_0}$$

From equations (9.2), (9.3) and (9.4) :

$$\left.\begin{aligned} n_1E_i\cos\theta_1-n_1E_r\cos\theta_1 &= n_2E_t\cos\theta_2 \\ \text{From equation (9.1)} \quad & \\ &= n_2(E_i + E_r)\cos\theta_2 \end{aligned}\right\} \tag{9.5}$$

Hence
$$\frac{E_r}{E_i} = \frac{n_1\cos\theta_1-n_2\cos\theta_2}{n_2\cos\theta_2+n_1\cos\theta_1} \tag{9.6}$$

Now
$$n_1\sin\theta_1 = n_2\sin\theta_2$$

so
$$\cos\theta_2 = \sqrt{1-\frac{n_1^2\sin^2\theta_1}{n_2^2}} \tag{9.7}$$

$\therefore$
$$\frac{E_r}{E_i} = \frac{n_1\cos\theta-\sqrt{n_2^2-n_1^2\sin^2\theta_1}}{n_1\cos\theta+\sqrt{n_2^2-n_1^2\sin^2\theta_1}} \tag{9.8}$$

For total internal reflection at the interface $n_1\sin\theta_1>n_2$ equation (9.8) may then be written as :

$$\frac{E_r}{E_i} = \frac{n_1\cos\theta-j\sqrt{n_1^2\sin^2\theta_1-n_2^2}}{n_1\cos\theta+j\sqrt{n_1^2\sin^2\theta_1-n_2^2}} \tag{9.9}$$

which is of the form

$$(a-jb/a+jb) = \frac{\sqrt{a^2+b^2}\ e^{-j\phi_{TE}}}{\sqrt{a^2+b^2}\ e^{j\phi_{TE}}}$$

where $\tan\phi_{TE} = b/a$.

The phase shift is therefore $2\phi_{TE}$ where

$$\tan\phi_{TE} = \{\sqrt{n_1^2\sin^2\theta_1-n_2^2}\}/n_1\cos\theta_1 \tag{9.10}$$

If $n_2 = -jn_2''$ equation (9.9) becomes:

$$\frac{E_r}{E_i} = \frac{\dfrac{n_1\cos\theta_1}{n_2''} - j\sqrt{1+\dfrac{n_1^2\sin^2\theta_1}{(n''_2)^2}}}{\dfrac{n_1\cos\theta_1}{n''_2} + j\sqrt{1+\dfrac{n_1^2\sin^2\theta_1}{(n_2'')^2}}} \tag{9.11}$$

and the new phase shift is $2\phi_{TE}$ where

$$\tan\phi_{TE} = \frac{n_2''}{n_1\cos\theta_1}\sqrt{1+\frac{n_1^2\sin^2\theta_1}{(n_2'')^2}} \tag{9.12}$$

TM Polarisation

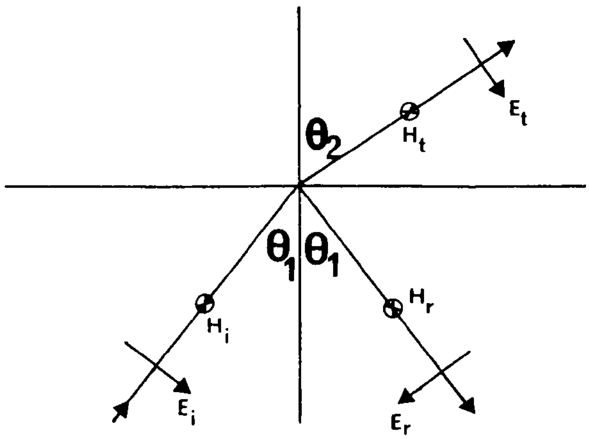

Matching tangential H

$$H_i + H_r = H_t \tag{9.13}$$

Using equations (9.3) and (9.4) this gives

$$(E_i + E_r)n_1 = n_2E_t \tag{9.14}$$

Matching tangential E :

$$(E_i - E_r)\cos\theta_1 = E_t \cos\theta_2 \tag{9.15}$$

Eliminating E_t from equations (9.14) and (9.15) :

$$\frac{E_r}{E_i} = \frac{n_2\cos\theta_1 - n_1\cos\theta_2}{n_2\cos\theta_1 + n_1\cos\theta_2}$$

$$= \frac{\dfrac{n_2\cos\theta_1}{n_1} - \sqrt{1-\left(\dfrac{n_1}{n_2}\right)^2\sin^2\theta_1}}{\dfrac{n_2\cos\theta_1}{n_1} + \sqrt{1-\left(\dfrac{n_1}{n_2}\right)^2\sin^2\theta_1}} \tag{9.16}$$

As in the TE case there is a phase shift $2\phi_{TM}$ on total internal reflection where

$$\tan\phi_{TM} = \frac{n_1^2}{n_2^2}\,\frac{\sqrt{n_1^2\sin^2\theta_1 - n_2^2}}{n_1\cos\theta_1} \tag{9.17}$$

If n_2 is purely imaginary ($n_2 = -jn_2''$) equation (9.16) leads to

$$\tan\phi_{TM} = \frac{(n_2'')^2 n_1\cos\theta_1}{n_1^2\sqrt{(n_2'')^2 + n_1^2\sin^2\theta_1}} \tag{9.18}$$

since the numerator becomes :

$$\frac{-jn_2''}{n_1}\cos\theta_1 - \sqrt{1 + \frac{n_1^2\sin^2\theta_1}{(n_2'')^2}}$$

9.2 Computer Program for the Solution of the Eigenvalue Equation

```
      PROGRAM(ITSI)
      INPUT 1=CR0
      OUTPUT 2=LP0
      TRACE 1
      END
      MASTER SLABS
      COMPLEX CN(3),CGUESS,CMGUESS,CSOLN,CMSOLN
      COMPLEX CEGAMMA,CFK,CMGAMMA
      DIMENSION RK(3),DECUT(4),DMCUT(4)
      REAL MSOLN
      COMMON WAVEL,PI,FK
    5 PI=3.14159265
   10 READ(1,15) CN
   15 FORMAT(2(2E0.0/),2E0.0)
   20 READ(1,25) T,WAVEL
   25 FORMAT(E0.0/E0.0)
   30 READ(1,35) NY
   35 FORMAT(I1)
   40 WRITE(2,45) CN
   45 FORMAT(1H ,2(2F10.7,5X),2F10.7/1H )
   50 WRITE(2,55) T,WAVEL,NY
   55 FORMAT(1H ,'SLAB THICKNESS=',E14.7/
   5511H ,'FREE SPACE WAVELENGTH=',E14.7/
   5521H ,'MODE=',I1)
   60 FK=2.0*PI/WAVEL
   65 CFK=CMPLX(FK,0.0)
   70 DO 80 J=1,3
   75 RK(J)=REAL(CN(J)*CN(J))
   80 CONTINUE
   85 CALL EMODES(RK(1),RK(2),RK(3),T,MODES)
   90 WRITE(2,95) MODES
   95 FORMAT(1H ,'NO. TE MODES=',I1)
  100 DO 120 JK=1,4
  105 CALL ECUT(RK(1),RK(2),RK(3),JK,DECUT(JK))
  110 WRITE(2,115) JK,DECUT(JK)
  115 FORMAT(1H ,'TE MODE ',I1,' CUT OFF WIDTH=',E14.7)
  120 CONTINUE
  125 IF(T.LT.DECUT(NY)) GO TO 400
  130 CALL RBETA(RK(1),RK(2),RK(3),T,NY,MODES,ESOLN)
  135 CGUESS=CMPLX(ESOLN,0.0)
  140 CALL CNTE(CN(1),CN(2),CN(3),T,CGUESS,CSOLN)
  145 CEGAMMA=CMPLX(0.0,1.0)*CSQRT(CN(2)*CN(2)*CFK*CFK-CSOLN*CSOLN)
  150 WRITE(2,155) NY,ESOLN,CSOLN,CEGAMMA
  155 FORMAT(1H ,'TE MODE ',I1,' : '/1H ,'ESOLN=',E14.7,5X,
  1551'CSOLN=',2E14.7/1H ,'GAMMA=',2E14.7/1H ,'*********************')
  160 CALL PLOT(RK(1),RK(2),RK(3),ESOLN,T)
  165 CALL MMODES(RK(1),RK(2),RK(3),T,MODMS)
  170 WRITE(2,175) MODMS
  175 FORMAT(1H ,'NO. TM MODES=',I1)
  180 DO 200 JMK=1,4
  185 CALL MCUT(RK(1),RK(2),RK(3),JMK,DMCUT(JMK))
  190 WRITE(2,195) JMK,DMCUT(JMK)
  195 FORMAT(1H ,'TM MODE ',I1,' CUT OFF WIDTH=',E14.7)
  200 CONTINUE
  210 IF(T.LT.DMCUT(NY)) GO TO 400
  220 CALL RBMTA(RK(1),RK(2),RK(3),T,NY,MODMS,MSOLN)
  225 CMGUESS=CMPLX(MSOLN,0.0)
  230 CALL CNTM(CN(1),CN(2),CN(3),T,CMGUESS,CMSOLN)
  235 CMGAMMA=CMPLX(0.0,1.0)*CSQRT(CN(2)*CN(2)*CFK*CFK-CMSOLN*CMSOLN)
  240 WRITE(2,245) NY,MSOLN,CMSOLN,CMGAMMA
  245 FORMAT(1H ,'TM MODE ',I1,' : '/1H ,'MSOLN=',E14.7,5X,
  2451'CMSOLN=',2E14.7/1H ,'GAMMA=',2E14.7)
  255 CALL PLOT(RK(1),RK(2),RK(3),MSOLN,T)
  260 GO TO 500
  400 WRITE(2,405)
  405 FORMAT(1H ,'MODE CUT OFF')
  500 STOP
      END
```

```
      SUBROUTINE EMODES(RK1,RK2,RK3,T2,NE2)
      COMMON WAVEL,PI,FK
C
C THIS SUBROUTINE FINDS NO. TE MODES
C
    5 G1=1.
    7 Q22=(RK2-RK3)*FK*FK
   10 Q2=SQRT(Q22)
   15 P1=SQRT((RK2-RK1)*FK*FK-Q22)
   35 NE2=INT((Q2*T2-ATAN((G1*P1)/Q2))/PI+1.)
   50 RETURN
      END
      SUBROUTINE ECUT(RK1,RK2,RK3,NE2,D)
      COMMON WAVEL,PI,FK
    5 G1=1.
    7 Q22=(RK2-RK3)*FK*FK
   10 Q2=SQRT(Q22)
   15 P1=SQRT((RK2-RK1)*FK*FK-Q22)
   45 D=(ATAN((G1*P1)/Q2)+FLOAT(NE2-1)*PI)/Q2
   65 RETURN
      END


      SUBROUTINE RBETA(RK1,RK2,RK3,T2,NX,NE2,GUESS)
      COMMON WAVEL,PI,FK
    5 Q22=0.0
   10 L=0
   15 IF(NX.GT.NE2) GO TO 110
C
C THIS PART FINDS THE TE MODES BETWEEN 1 AND NE2
C
  110 Q2=(FLOAT(2*NX-1)*PI/(2.0*T2))-1.0E-7/T2
  115 Q=SQRT(RK2-RK3)*FK
  120 IF(Q.LT.Q2) GO TO 170
  125 CALL FE(RK1,RK2,RK3,Q2,T2,F1,F2)
  130 IF(F2.LT.0.0) GO TO 250
  140 QA=(FLOAT(NX-1)*PI)/T2
  150 QB=Q2
  160 GO TO 175
  170 QB=Q
  172 QA=(FLOAT(NX-1)*PI)/T2
  175 Q2=(QA+QB)/2.0
  177 L=L+1
  178 IF(L.GE.100) GO TO 410
  180 IF(ABS((Q2-Q22)/Q2).LE.1.0E-5) GO TO 400
  185 CALL FE(RK1,RK2,RK3,Q2,T2,F1,F2)
  190 IF(F1.GE.0.0.AND.F2.LT.0.0) GO TO 230
  195 IF(F1.LT.0.0.AND.F2.GE.0.0) GO TO 210
  200 IF((F1-F2).LT.0.0) GO TO 230
  210 Q22=Q2
  215 QB=Q2
  220 GO TO 175
  230 Q22=Q2
  235 QA=Q2
  240 GO TO 175
  250 QA=Q2+2.0E-7/T2
  255 QB=(FLOAT(NX)*PI)/T2
  260 IF(Q.GE.QB) GO TO 175
  265 QB=Q
  270 GO TO 175
  400 GUESS=Q2
  405 RETURN
  410 STOP
      END
```

```
      SUBROUTINE MNODES(RK1,RK2,RK3,T2,NE2)
      COMMON WAVEL,PI,FK
C
C THIS SUBROUTINE FINDS NO. TM MODES
C
    5 G1=RK2/RK1
    7 Q22=(RK2-RK3)*FK*FK
   10 Q2=SQRT(Q22)
   15 P1=SQRT((RK2-RK1)*FK*FK-Q22)
   35 NE2=INT((Q2*T2-ATAN((G1*P1)/Q2))/PI+1.)
   50 RETURN
      END
      SUBROUTINE MCUT(RK1,RK2,RK3,NE2,D)
      COMMON WAVEL,PI,FK
    5 G1=RK2/RK1
    7 Q22=(RK2-RK3)*FK*FK
   10 Q2=SQRT(Q22)
   15 P1=SQRT((RK2-RK1)*FK*FK-Q22)
   45 D=(ATAN((G1*P1)/Q2)+FLOAT(NE2-1)*PI)/Q2
   65 RETURN
      END


      SUBROUTINE RBMTA(RK1,RK2,RK3,T2,NX,NE2,GUESS)
      COMMON WAVEL,PI,FK
    5 Q22=0.0
   10 L=0
   15 IF(NX.GT.NE2) GO TO 110
C
C THIS PART FINDS THE TM MODES BETWEEN 1 AND NE2
C
  110 Q2=(FLOAT(2*NX-1)*PI/(2.0*T2))-1.0E-7/T2
  115 Q=SQRT(RK2-RK3)*FK
  120 IF(Q.LT.Q2) GO TO 170
  125 CALL FM(RK1,RK2,RK3,Q2,T2,F1,F2)
  130 IF(F2.LT.0.0) GO TO 250
  140 QA=(FLOAT(NX-1)*PI)/T2
  150 QB=Q2
  160 GO TO 175
  170 QB=Q
  172 QA=(FLOAT(NX-1)*PI)/T2
  175 Q2=(QA+QB)/2.0
  177 L=L+1
  178 IF(L.GE.100) GO TO 410
  180 IF(ABS((Q2-Q22)/Q2).LE.1.0E-5) GO TO 400
  185 CALL FM(RK1,RK2,RK3,Q2,T2,F1,F2)
  190 IF(F1.GE.0.0.AND.F2.LT.0.0) GO TO 230
  195 IF(F1.LT.0.0.AND.F2.GE.0.0) GO TO 210
  200 IF((F1-F2).LT.0.0) GO TO 230
  210 Q22=Q2
  215 QB=Q2
  220 GO TO 175
  230 Q22=Q2
  235 QA=Q2
  240 GO TO 175
  250 QA=Q2+2.0E-7/T2
  255 QB=(FLOAT(NX)*PI)/T2
  260 IF(Q.GE.QB) GO TO 175
  265 QB=Q
  270 GO TO 175
  400 GUESS=Q2
  405 RETURN
  410 STOP
      END
```

```
      SUBROUTINE FE(RK1,RK2,RK3,Q2,T2,F1,F2)
      COMMON WAVEL,PI,FK
    5 G1=1.0
    7 G3=1.0
   10 P1=SQRT((RK2-RK1)*FK*FK-Q2*Q2)
   15 P3=SQRT((RK2-RK3)*FK+FK-Q2*Q2)
   35 F1=TAN(Q2*T2)
   40 F2=Q2*(G1*P1+G3*P3)/(Q2*Q2-G1*G3*P1*P3)
   45 RETURN
      END
      SUBROUTINE FM(RK1,RK2,RK3,Q2,T2,F1,F2)
      COMMON WAVEL,PI,FK
    5 G1=RK2/RK1
    7 G3=RK2/RK3
   10 P1=SQRT((RK2-RK1)*FK*FK-Q2*Q2)
   15 P3=SQRT((RK2-RK3)*FK*FK-Q2*Q2)
   35 F1=TAN(Q2*T2)
   40 F2=Q2*(G1*P1+G3*P3)/(Q2*Q2-G1*G3*P1*P3)
   45 RETURN
      END


      SUBROUTINE CNTM(RN1,RN2,RN3,T2,GUESS,SOLN)
      COMPLEX RN1,RN2,RN3,GUESS,SOLN,P1,Q2,P3,QQ2,FUNCT,DIFF,CFK,CT2
      COMPLEX CG1,CG3
      COMMON WAVEL,PI,FK
C
C THIS SUBROUTINE SOLVES THE COMPLEX EIGENVALUE EQN. FOR TM MODES
C
   10 CFK=CMPLX(FK,0.0)
   12 CT2=CMPLX(T2,0.0)
C
C (CFK,CT2 ARE FK,T2 IN COMPLEX NOTATION)
C
   30 SOLN=CMPLX(0.0,0.0)
   40 QQ2=CMPLX(0.0,0.0)
   50 Q2=GUESS
   60 LN=1
   70 CG1=RN2*RN2/(RN1*RN1)
   75 CG3=RN2*RN2/(RN3*RN3)
  100 P1=CSQRT(CFK*CFK*(RN2*RN2-RN1*RN1)-Q2*Q2)
  120 P3=CSQRT(CFK*CFK*(RN2*RN2-RN3*RN3)-Q2*Q2)
C
  150 FUNCT=CSIN(Q2*CT2)/CCOS(Q2*CT2)-Q2*(CG1*P1+CG3*P3)/
  1501(Q2*Q2-CG1*P1*CG3*P3)
C
  170 DIFF=CT2/(CCOS(Q2*CT2)*CCOS(Q2*CT2))-((Q2*Q2-CG1*CG3*
  1701P1*P3)*(CG1*(P1-Q2*Q2/P1)+CG3*(P3-Q2*Q2/P3))-(Q2*(
  1702CG1*P1+CG3*P3))*(Q2*(CMPLX(2.0,0.0)+CG1*CG3*(P1/P3+
  1703P3/P1))))/((Q2*Q2-CG1*CG3*P1*P3)*(Q2*Q2-CG1*CG3*P1*P3))
C
  190 IF(CABS((Q2-QQ2)/Q2).LE.1.0E-9) GO TO 260
  200 IF(LN.GE.200) GO TO 270
  210 LN=LN+1
  212 WRITE(2,213) Q2,FUNCT,DIFF
  213 FORMAT(1H ,3(3X,2E14.7))
  220 QQ2=Q2
  240 Q2=Q2-FUNCT/DIFF
  250 GO TO 100
  260 SOLN=Q2
  270 RETURN
      END
```

```
      SUBROUTINE CNTE(RN1,RN2,RN3,T2,GUESS,SOLN)
      COMPLEX RN1,RN2,RN3,GUESS,SOLN,P1,Q2,P3,QQ2,FUNCT,DIFF,CFK,CT2
      COMPLEX CG1,CG3
      COMMON WAVEL,PI,FK
C
C THIS SUBROUTINE SOLVES THE COMPLEX EIGENVALUE EQN. FOR TE MODES
C
   10 CFK=CMPLX(FK,0.0)
   12 CT2=CMPLX(T2,0.0)
C
C (CFK,CT2 ARE FK,T2 IN COMPLEX NOTATION)
C
   30 SOLN=CMPLX(0.0,0.0)
   40 QQ2=CMPLX(0.0,0.0)
   50 Q2=GUESS
   60 LN=1
   70 CG1=CMPLX(1.0,0.0)
   75 CG3=CMPLX(1.0,0.0)
  100 P1=CSQRT(CFK*CFK*(RN2*RN2-RN1*RN1)-Q2*Q2)
  120 P3=CSQRT(CFK*CFK*(RN2*RN2-RN3*RN3)-Q2*Q2)
C
  150 FUNCT=CSIN(Q2*CT2)/CCOS(Q2*CT2)-Q2*(CG1*P1+CG3*P3)/
  1501(Q2*Q2-CG1*P1*CG3*P3)
C
  170 DIFF=CT2/(CCOS(Q2*CT2)*CCOS(Q2*CT2))-((Q2*Q2-CG1*CG3*
  1701P1*P3)*(CG1*(P1-Q2*Q2/P1)+CG3*(P3-Q2*Q2/P3))-(Q2*(
  1702CG1*P1+CG3*P3))*(Q2*(CMPLX(2.0,0.0)+CG1*CG3*(P1/P3+
  1703P3/P1))))/((Q2*Q2-CG1*CG3*P1*P3)*(Q2*Q2-CG1*CG3*P1*P3))
C
  190 IF(CABS((Q2-QQ2)/Q2).LE.1.0E-9) GO TO 260
  200 IF(LN.GE.200) GO TO 270
  210 LN=LN+1
  212 WRITE(2,213) Q2,FUNCT,DIFF
  213 FORMAT(1H ,3(3X,2E14.7))
  220 QQ2=Q2
  240 Q2=Q2-FUNCT/DIFF
  250 GO TO 100
  260 SOLN=Q2
  270 RETURN
      END
      SUBROUTINE PLOT(R1,R2,R3,Q2,T2)
      DIMENSION A(101)
      COMMON WAVEL,PI,FK
      DATA BLANK,STAR,LINE/1H ,1H*,1HI/
    2 P1=SQRT((R2-R1)*FK*FK-Q2*Q2)
    3 P3=SQRT((R2-R3)*FK*FK-Q2*Q2)
    4 B1=1.0/SQRT(1.0+P1*P1/(Q2*Q2))
    5 WRITE(2,10)
   10 FORMAT(1H ,'X:Y',56X,'FIELD STRENGTH')
   15 X=-T2
   20 IF(X.GE.0.0) GO TO 35
   25 FA=B1*EXP(P1*X)
   30 GO TO 60
   35 IF(X.GE.T2) GO TO 50
   40 FA=B1*(COS(Q2*X)+(P1/Q2)*SIN(Q2*X))
   45 GO TO 60
   50 IF(X.GE.(2.0*T2)) GO TO 115
   55 FA=B1*(COS(Q2*T2)+(P1/Q2)*SIN(Q2*T2))*EXP(-P3*(X-T2))
   60 NA=NINT(FA*50.0)+51
   65 DO 75 J=1,101
   70 A(J)=BLANK
   75 CONTINUE
   80 A(NA)=STAR
   85 A(51)=LINE
   90 WRITE(2,100)X,A
  100 FORMAT(1H ,E9.3,101A1)
  105 X=X+T2/20.0
  110 GO TO 20
  115 RETURN
      END
```

9.3 Characteristic Equations for the Effective Index Analysis of Directional Couplers

For TM modes in the equivalent slab guides (Fig.2.7) elementary solutions of Maxwell's equations are sought describing waves that do not radiate away from the structure. Exponential or hyperbolic functions are suitable in regions I and III: sine or cosine functions in region II. Taking advantage of symmetry, suitable mode profiles are :

$$H_x = H_1 \exp-(p_1(y-c-a)) \qquad y>(c+a)$$

$$H_2\{\cos(q_2(y-c-a)) - A\sin q_2(y-c-a)\}$$

$$(c-a) < y < (c+a)$$

$$H_3\{\cosh(p_3 y)\} \quad (c-a) > y > (a-c)$$

$$H_2\ \{\cos q_2(y+c+a) + A\sin q_2(y+c+a)\} \ -c-a < y < a-c$$

$$H_1\ \exp(p_1(y+c+a)) \quad y < -a-c.$$

p_1, q_2, p_3, c and a are as in section 2.2.2.

Asymmetric Mode

$$H_x = H_1 \exp-[p_1(y-c-a)] \qquad y > (a+c)$$

$$H_2\{\cos q_2(y-c-a) - A\sin q_2(y-c-a)\} \quad c-a < y < a+c$$

$$H_3\ \sinh(p_3 y) \quad c-a > y > a-c$$

$$-H_2\{\cos q_2(y+c+a) + A\sin q_2(y+c+a)\} \quad a-c > y > c-a$$

$$-H_1\ \exp\{p_1(y+c+a)\} \quad y < -c-a$$

Matching H_x and E_z $\left(\alpha\frac{1}{N^2}\ \frac{\partial H_x}{\partial y}\right)$ fields at y = (a+c) and x = (c-a) the characteristic equations (2.28) are derived.

9.4 Finite-Difference Form of Partial Derivatives

Consider the following mesh points :

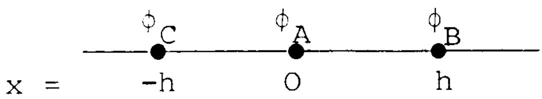

From Taylor's Theorem [81]

$$\phi(x+dx) = \phi(x) + \frac{\partial\phi}{\partial x}(x)dx + \frac{\partial^2\phi}{\partial x^2}\frac{(dx)^2}{2!} + \ldots\ldots$$

Thus

$$\phi_B = \phi_A + \left.\frac{\partial\phi}{\partial x}\right|_o h + \left.\frac{\partial^2\phi}{\partial x^2}\right|_o \frac{h^2}{2!} + \ldots \tag{9.19}$$

and

$$\phi_C = \phi_A - \left.\frac{\partial\phi}{\partial x}\right|_o h + \left.\frac{\partial^2\phi}{\partial x^2}\right|_o \frac{h^2}{2!} + \ldots \tag{9.20}$$

Adding (9.19) and (9.20) :

$$\left.\frac{\partial^2\phi}{\partial x^2}\right|_o = \frac{\phi_B+\phi_C-2\phi_A}{h^2} + h^2 D_4 \tag{9.21}$$

Where D_4 is a combination of third-order partial derivatives in the interval considered.

9.5 The Rayleigh Quotient

Multiplying the wave-equation for a trial field $\phi(x,y)$ by $\phi(x,y)$ and integrating over the cross-section yields :

$$\iint \{\phi\nabla^2\phi + n^2k^2\phi^2 - N^2k^2\phi^2\}dS = 0 \tag{9.22}$$

Replacing ϕ by $(\phi+\delta\phi)$ and k^2 by $(k^2+\delta k^2)$ and neglecting second-order variations in ϕ gives

$$\iint\{\phi+\delta\phi)\}\nabla^2\phi+\phi\nabla^2\delta\phi+(n^2-N^2)(k^2+\delta k^2)[\phi^2+2\phi\delta\phi]\}dS \tag{9.23}$$

From Green's theorem :

$$\phi\nabla^2\delta\phi-\delta\phi\nabla^2\phi = \oint[\phi\frac{\partial}{\partial n}(\delta\phi) - \delta\phi\frac{\partial\phi}{\partial n}]\, d\ell$$

and following the same arguments as in section 2.3.2.1 the contour integral is zero for guided modes. So (9.23) becomes :

$$\iint\{(\phi+2\delta\phi)\nabla^2\phi+(n^2-N^2)(k^2+\delta k^2)[\phi^2+2\phi\delta\phi]\}dS = 0 \tag{9.24}$$

But $\nabla^2\phi = -(n^2-N^2)k^2\phi$ and hence

$$\iint[\delta k^2(n^2-N^2)\{\phi^2+ 2\phi\delta\phi\}]dS = 0 \tag{9.25}$$

i.e. $\delta k^2 = 0$

Orthonormality gives :

$$\beta^2 = N^2k_0{}^2 = \frac{\sum\limits_{r=0}^{\infty} a_r{}^2\beta_r{}^2}{\sum\limits_{r=0}^{\infty} a_r{}^2}$$

$$= \beta_0{}^2 + \frac{\sum\limits_{r=1}^{\infty} a_r{}^2(\beta_r{}^2-\beta_0{}^2)}{\sum a_r{}^2} \tag{9.26}$$

The β_r are such that

$$\beta_0{}^2 > \beta_1{}^2 > \beta_2{}^2 > \ldots\ldots > \beta_r{}^2 >$$

It has been shown therefore that a variational expression for the propagation constant β of a planar waveguide follows from the wave-equation and is :

$$\beta^2 \geq \frac{\iint (\phi\nabla^2\phi + n^2k^2\phi^2)\,dS}{\iint \phi^2\,dS} \qquad (9.27)$$

Equality holds if $a_r = 0$ for $r > 0$ i.e. if $\phi = \psi_0$.

(9.27) yields a lower bound for β^2 which improves as the trial function ϕ approaches the actual mode distribution. For $\phi = \psi_0$ the expression has a maximum value equal to β^2.

The improvement of the value of β^2 as ϕ approaches the actual mode distribution is illustrated by the results of Fig.6.7.

9.6 A Method for Finding the Optimum Acceleration Factor for S.O.R. (S_o) and a Practical Scheme of Computer Solution

The problem of solving the wave-equation is reduced by the finite difference operator to solving the matrix eigenvalue problem :

$$A\phi = \lambda\phi \tag{9.28}$$

for the smallest eigenvalue λ_0 and eigenvector ϕ_0. If an initial guess b_i is made to the eigenvector an approximation μ to λ_0 may be found from the Rayleigh Quotient as :

$$\mu = \frac{b_i^* A b_i}{b_i^* b_i} \tag{9.29}$$

and a b_{i+1} found from the relation

$$b_{i+1} = Hb_i$$

where H is the S.O.R. matrix for solution of $(A-\mu)b = 0$.

Sinnott |40| shows that the eigenvalues of the matrix H converge to give $b_i = \phi_0$ and $\mu = \lambda_0$. He also states that the optimum convergence to the required eigenvector is attained when the largest subdominant eigenvalue λ_2 is a double root of magnitude (S_o-1).

S_o may be estimated from a value of λ_2 determined whilst iterating with $S < S_o$ as |42| :

$$S_o = 2\left\{ 1+ \left[1- \frac{(\lambda_2+S-1)^2}{\lambda_2 S^2}\right]^{\frac{1}{2}}\right\}^{-1} \tag{9.30}$$

If a displacement vector r_i defined as

$$r_i = b_i - b_{i-1}$$

is computed after a complete iteration then [41], [42]

$$\lambda_2 = \lim_{i\to\infty} \left\{\frac{|r_{i+1}|}{|r_i|}\right\} \tag{9.31}$$

where $|r_{i+1}|$ is any norm of the vector r_{i+1}.

The practical scheme used for solving waveguide problems using S.O.R. is :

(1) Guess eigenvalue and eigenvector.

(2) Perform 5 iterations with $S = 1$ and then use the Rayleigh Quotient to improve the eigenvalue.

(3) Estimate λ_2 using the absolute values of the elements of the displacement vector

$$\delta^{(k)} = b_k - b_{k-1}$$

A norm of the root of the sum of the squares of b_i elements has also been used successfully.

(4) Calculate S_o from (9.30) and reduce it slightly [41] using the expression :

$$S_m = S_o - \frac{(2-S_o)}{4} \tag{9.32}$$

suggested by Carré [42].

(5) Set $S = S_m$, re-iterate 3 times and recalculate S_o. If successive estimates of S_o differ by an amount ΔS_e such that

$$\frac{|\Delta S_e|}{(2-S_o)} < 0.05 \tag{9.33}$$

then the value of S_o is deemed to be the correct one and no further estimate undertaken.

(6) Proceed with iterations until convergence is obtained to the accuracy required and then perform a few final sweeps with S = 1 to smooth the field solution [38].

A feature was included in the computer program to avoid attempting to take the square root of a negative number when calculating S_o from (9.30). This occurs when $\lambda_2 > 1$ indicating that S is too large and the solution is oscillating. The difficulty was overcome by reducing S as in (9.32) to a minimum value of one and then recalculating after subsequent iterations.

All the features described are incorporated in the following computer program for finding the symmetric mode in a strain-induced slot waveguide.

```
100  REM FROG TO CALCULATE RI AND FIND FIELDS
110  U=3.14159
120  PRINT 'X STEP LENGTH MICRONS'
130  INPUT X
140  PRINT 'Y STEP LENGTH MICRONS'
150  INPUT Y
160  X5=X
170  Y5=Y
180  PRINT 'INPUT FILM DEPTH(STEPS)'
190  INPUT H
200  PRINT 'BOX HALF WIDTH STEPS  B'
210  INPUT B
220  PRINT 'BOX DEPTH A STEPS'
230  INPUT A
240  PRINT 'STLOT HALFWIDTH S STEPS'
250  INPUT S
260  PRINT 'N2='
270  INPUT N2
280  PRINT 'N3=
290  INPUT N3
300  PRINT 'INPUT AU THICKNESS MICRONS'
310  INPUT T
320  F=600*T
330  V=.23
340  E=120000
350  D=2*F*(1+V)/(U*E)
360  P=X
370  R=Y
380  Y0=S*R
390  DIM N(150,150)
400  FOR J=1 TO B
410  Y=(J-1)*R
420  FOR I=1 TO H-1
430  X=I*P
440  GOSUB 1510
450  N(I,J)=N2*(1+N2^2*(.07*E1+.113*E2))
460  NEXT I
470  FOR I=H+1 TO A-1
480  X=I*P
490  GOSUB 1510
500  N(I,J)=N3*(1+N2^2*(.07*E1+.113*E2))
510  NEXT I
520  I=H
530  GOSUB 1510
540  N(H,J)=(N2+N3)*(1+(N2+N3)^2*(.07*E1+.113*E2)/4)/2
550  NEXT J
560  PRINT 'NO OF ITERATIONS'
570  INPUT Q
580  K=2*U/1.15
590B2=1
600F=0
610P5=0
620  C=0
630  X=Y5
640  Y=Y5
650  G=0
660B1=1
670  DIM E(150,150)
680DIME1(150,150)
690  FOR I=1 TO A-1
700  FOR J=0 TO B+1
710  E(I,J)=1
720  NEXT J
730  NEXT I
```

```
740  N=N3
750 F8=-12
760B2=1
770B7=B2
780FORI=0TOA
790FORJ=0TOB
800E1(I,J)=E(I,J)
810NEXTJ
820NEXTI
830D2=D1
840D1=0
850FOR I=1 TO A-1
 860  FOR J=1 TO B
 870  E(0,J)=0
 880  E(A,J)=0
 890  S=E(I+1,J)+E(I-1,J)+(X/Y)^2*(E(I,J+1)+E(I,J-1))
 900  E(I,J)=S/(2*(1+(X/Y)^2)-K^2*X^2*(N(I,J)^2-N^2))
910E(I,J)=B2*E(I,J)-(B2-1)*E1(I,J)
 920  E(I,B+1)=0
 930  E(I,0)=E(I.2)
940 D1=D1+ABS(E(I.J)*E(I.J)-E1(I.J)*E1(I.J))
 950  NEXT J
 960  NEXT I
 970  P=P+1
980 D1=SQR(D1)
990F5=P5+1
1000P8=P8+1
 1010  REM ROUOTIENT
 1020  FOR I=1 TO A-1
 1030  FOR J=2 TO B
 1040  GOSUB 1560
 1050  C=C+Q
 1060  NEXT J
 1070  J=1
 1080  GOSUB 1560
 1090  C=C+Q/2
 1100  NEXT I
 1110  FOR I=1 TO A-1
 1120  FOR J=2 TO B
 1130  F=E(I,J)^2
 1140  G=F+G
 1150  NEXT J
 1160  G=G+E(I,1)^2/2
 1170  NEXT I
1180N=SQR(C/G)/(K*X)
1190C=0
1200G=0
1210 IF P5<50 THEN 1230
1220GO SUB 1590
1230IF P8<3 THEN 1250
1240 GO SUB 1640
1250 IF P>(O-3) THEN 1270
1260 GO TO 1290
1270B2=1
1280 PRINT"N=":N
1290 IF P=1 THEN 1320
1300IF P>O THEN1350
1310 GO TO 760
1320 B2=1.375
1330B7=B2
1340 GO TO 760
 1350  PRINT "WAVEL=1.15"
 1360  PRINT "X=":X
 1370  PRINT "H=":H
 1380  PRINT "A=":A
 1390  PRINT "B=":B
```

```
1420 PRINT 'DO YOU WANT FIELD--TYPE Y OR N'
1430 INPUT Z$
1440 IF Z$='N'THEN 1500
1450 I=6
 1460  FOR J=1 TO B
 1470  PRINT 'E(':I:J:')=':E(I,J)
 1480  NEXT J
 1500  END        1510 N = (X^2+(Y+Y0)^2)^2
1520  M=(X^2+(Y-Y0)^2)^2
1530  E1=D*((1-V)*X^2*((Y+Y0)/N-(Y-Y0)/M)-V*((Y+Y0)^3/N-(Y-Y0)^3/M))
1540  E2=D*((1-V)*((Y+Y0)^3/N-(Y-Y0)^3/M)-V*X^2*((Y+Y0)/N-(Y-Y0)/M))
1550  RETURN
1560  Q=E(I+1,J)+E(I-1,J)-2*E(I,J)+(X/Y)^2*(E(I,J+1)+E(I,J-1)-2*E(I,J))+
(N(I,J)*K*X)^2*E(I,J)
1570  Q=Q*E(I,J)
1580  RETURN
1590P5=0
1600PRINT'P=':P
1610PRINT'FACTOR=':B2
1620PRINT'N=':N
1630RETURN
1640L1=D1/D2
1650 B1=B2
1660 P8=0
1670B9=B7
1680IF B6=5 THEN1830
1690 IF(((L1+B1-1)^2)/(L1*B1*B1))>1 THEN 1750
1700 B2=2/(1+SQR(1-((L1+B1-1)^2/(L1*B1*B1))))
1710B7=B2
1720 B2=B2-0.4*(2-B2)
1730B5=(B7-B9)
1740GO TO 1780
1750PRINT '4007 OK FOR P=':P
1760B2=B2-0.4*(2-B2)
1765 IF B2<1 THEN B2=1
1770 RETURN
1780 IF ABS(B5/(2-B7))<0.05 THEN 1800
1790RETURN
1800B6=5
1810PRINT'4055 SATISFIED WHEN P=':P
1820 PRINT'FACTOR=':B2
1830 RETURN
```

9.7 Loss in Waveguides

From Maxwell's equation :

$$\nabla \times \underset{\sim}{H} = \underset{\sim}{J} + \frac{\partial \underset{\sim}{D}}{\partial L} = (\sigma + j\omega\varepsilon)\underset{\sim}{E} \tag{9.34}$$

$$\nabla \times \underset{\sim}{H} = j\omega\varepsilon_c \underset{\sim}{E}$$

where
$$\varepsilon_c = (n-jk)^2 \varepsilon_0 \tag{9.35}$$

From the imaginary parts of (9.34) and (9.35) :

$$\frac{\sigma}{\omega} = 2nk\varepsilon_0$$

or
$$k = \frac{\sigma}{2\omega n\varepsilon_0} .$$

The loss per unit volume is :

$$\underset{\sim}{E}.\underset{\sim}{J} = \frac{1}{2}\sigma E^2 = \omega nk\varepsilon_0 E^2 \tag{9.36}$$

where E is the maximum electric field amplitude and the intensity from the time-averaged Poynting vector is :

$$\left.\begin{aligned} &\frac{1}{2}\int E\,H\,dA \\ \text{where} \quad &\frac{E}{H} = \frac{1}{n}\sqrt{\frac{\mu_0}{\varepsilon_0}} \end{aligned}\right) \tag{9.37}$$

Writing $I = I_o \exp(-\alpha Z)$

$$\frac{dI}{I} = -\alpha Z \tag{9.38}$$

From (9.36) the power loss in distance dZ is

$$(\omega\varepsilon_0 \int nkE^2 dA)\,dZ \tag{9.39}$$

and using (9.37) and (9.39), (9.38) may be written as :

$$\alpha dZ = \frac{(\omega\varepsilon_0 \int nkE^2 dA)}{\sqrt{\frac{\mu_0}{\varepsilon_0}} \int nE^2 dA}\, dZ \tag{9.40}$$

But $\omega\sqrt{\mu_0 \varepsilon_0} = \omega/c = k_o$ (9.41)

Hence
$$\alpha = \frac{2k_o \int nkE^2 dA}{\int nE^2 dA} \tag{9.42}$$

9.8 Coupled Wave Theory of Directional-Couplers

Consider two waveguides (labelled a and b) whose evanescent fields overlap and each of which would propagate with normalised amplitude A satisfying the equation :

$$\frac{dA}{dZ} = -j\beta A \tag{9.43}$$

without the other waveguide present. Interaction between the two modes of the waveguides couples the differential equations for their mode amplitudes A_a and A_b so that :

$$\left.\begin{aligned} \frac{dA_a}{dZ} &= -j\beta_a A_a - jCA_b \\ \frac{dA_b}{dZ} &= -j\beta_b A_b - jCA_a \end{aligned}\right) \tag{9.44}$$

where C is the coupling coefficient giving the extent of overlap of the modes.

Unger [82] shows that in the coupling region the two modes of the uncoupled waveguides form two new modes propagating independently with propagation constants :

$$\beta_{1,2} = (\beta_c \pm \alpha) \tag{9.45}$$

where

$$\beta_c = \frac{1}{2}(\beta_{a1} + \beta_{b1}) \tag{9.46}$$

$$\alpha^2 = (\Delta\beta^{1^2} + C^2) \tag{9.47}$$

and

$$\Delta\beta^1 = \frac{1}{2}(\beta_{a1} - \beta_{b1}) \tag{9.48}$$

It should be noted that $\Delta\beta = 2\Delta\beta^1$. β_{a1}, β_{b1} are the propagation constants of the waveguides a and b in the section of the waveguide considered. The extra subscript has been added because later the possibility of having a second section of waveguide is considered where the propagation constants for waves in guides a and b are β_{a_2} and β_{b_2} respectively. β_1 is called β_S and β_2 is called β_A elsewhere in this thesis.

Combining the two modes given by (9.45) the general solution to (9.44) is :

$$\left.\begin{aligned} A_a &= A_1\exp(-j\beta_1 Z) + A_2\exp(-j\beta_2 Z) \\ A_b &= \left(\frac{\beta_1-\beta_{a_1}}{C}\right)A_1\exp(-j\beta_1 Z) + \frac{\beta_2-\beta_{a_1}}{C} A_2\exp(-j\beta_2 Z) \end{aligned}\right) \qquad (9.49)$$

If at Z = 0 mode a is launched with unit power and mode b with no power then :

$$A_2 = (1-A_1) = \tfrac{1}{2}\{1- \frac{\Delta\beta^1}{\alpha}\}$$

and the amplitudes in each waveguide mode along the coupling region are determined using (9.49). In particular at $Z = \ell_1$

$$\left.\begin{aligned} A_a(\ell_1) &= (\cos\phi_1-j\,\frac{\Delta\beta^1}{\alpha}\,\sin\phi_1)\; e^{-j\beta_c\ell_1} \\ \text{and} \quad & \\ A_b(\ell_1) &= (-\,\frac{jC}{\alpha}\,\sin\phi_1)\; e^{-j\beta_c\ell_1} \end{aligned}\right) \qquad (9.50)$$

where $\phi_1 = \alpha\ell_1$.

For phase synchronism between both coupled modes $\Delta\beta^1 = 0$ and from (9.50) the power P_a in the excited guide is :

$$P_a = \cos^2 C\ell_1 \qquad (9.51)$$

while it transfers the power

$$P_b = \sin^2 C\ell_1 \qquad (9.52)$$

All the power incident in mode a transfers to mode b at distances :

$$Z = \frac{(P+\frac{1}{2})\pi}{C} \qquad P = 0,1,2... \tag{9.53}$$

The coupling length L_c is the shortest length for complete power transfer between phase synchronous modes and is from (9.53) :

$$L_c = \frac{\pi}{2C} \tag{9.54}$$

From (9.47) and (9.48) :

$$L_c = \frac{\pi}{(\beta_1-\beta_2)} \tag{9.55}$$

In devices studied $\Delta\beta^1$ is introduced by the applied bias. In order to model directional-coupler structures having a reversed $\Delta\beta$ electrode configuration consider a second region of the guide of length L_2 with a $\Delta\beta^1$ of the same magnitude but of reversed sign.

In this region 2 :

$$\left.\begin{aligned} A_{a_2} &= (A_1{}^1 e^{-j\alpha Z_2} + A_2{}^1 e^{j\alpha Z_2}) e^{-j\beta_c Z_2} \\ A_{b_2} &= [(\frac{\beta_1-\beta_{a_2}}{C}) A_1{}^1 e^{-j\alpha Z_2} + (\frac{\beta_2-\beta_{a_2}}{C}) A_2 e^{j\alpha Z_2}] e^{-j\beta_c Z_2} \end{aligned}\right\} \tag{9.56}$$

where now

$$\beta_{\frac{1}{2}} = \frac{1}{2}(\beta_{a_2}+\beta_{b_2}) \pm \alpha \tag{9.57}$$

i.e. $$\beta_1-\beta_{a_2} = \frac{1}{2}(\beta_{b_2}-\beta_{a_2}) + \alpha$$

and $$\beta_2-\beta_{a_2} = \frac{1}{2}(\beta_{b_2}-\beta_{a_2}) - \alpha$$

and Z_2 is measured from the front of the second section.

As the sign of $\Delta\beta^1$ is reversed

$$\left.\begin{aligned}\beta_{a_1} &= \beta_{b_2}\\ \beta_{b_1} &= \beta_{a_2}\end{aligned}\right\}\tag{9.58}$$

so

$$\left.\begin{aligned}\beta_1 - \beta_{a_2} &= \Delta\beta^1 + \alpha\\ \beta_2 - \beta_{a_2} &= \Delta\beta^1 - \alpha\end{aligned}\right\}\tag{9.59}$$

Thus from (9.49), (9.50) and (9.59) :

$$\left.\begin{aligned}A_{a_2}(o) &= A_1{}^1 + A_2{}^1 = \cos\phi_1 - \frac{j\Delta\beta^1}{\alpha}\sin\phi_1\\ A_{b_2}(o) &= \left(\frac{\Delta\beta^1+\alpha}{C}\right) A_1{}^1 + \left(\frac{\Delta\beta^1-\alpha}{C}\right) A_2{}^1\\ &= -\frac{jC}{\alpha}\sin\phi_1\end{aligned}\right)\tag{9.60}$$

Solving for $A_1{}^1$ and $A_2{}^1$ and putting $Z_2 = \ell_2$ and $\phi_2 = \alpha\ell_2$ yields:

$$\left.\begin{aligned}A_{a_2}(\ell_2) &= [\cos\phi_1\cos\phi_2 + \frac{1}{\alpha^2}(\Delta\beta^{1^2} - C^2)\sin\phi_1\sin\phi_2\\ &\quad + j\frac{\Delta\beta^1}{\alpha}\sin(\phi_2-\phi_1)]e^{-j\beta_c\ell_2}\\ A_{b_2}(\ell_2) &= -\frac{C}{\alpha}[\frac{2\Delta\beta^1}{\alpha}\sin\phi_1\sin\phi_2 + j\sin(\phi_1+\phi_2)]e^{-j\beta_c\ell_2}\end{aligned}\right)\tag{9.61}$$

$$\left.\begin{aligned}P_a(\ell_2) &= A_{a_2}(\ell_2)A^*_{a_2}(\ell_2)\\ &= [\cos\phi_1\cos\phi_2 + \frac{1}{\alpha^2}(\Delta\beta^{1^2} - C^2)\sin\phi_1\sin\phi_2]^2\\ &\qquad + \frac{\Delta\beta^{1^2}}{\alpha^2}\sin^2(\phi_2-\phi_1)\\ P_b(\ell_2) &= A_{b_2}(\ell_2)A^*_{b_2}(\ell_2)\\ &= \frac{4C^2\Delta\beta^{1^2}}{\alpha^2}\sin^2\phi_1\sin^2\phi_2 + \frac{C^2}{\alpha^2}\sin^2(\phi_1+\phi_2)\end{aligned}\right)\tag{9.62}$$

N.B. : $P_a + P_b = 1.$

In a similar manner expressions may be derived for the power in each guide at the output of a device with more sections or with the magnitude of $\Delta\beta^1$ different for each electrode pair.